CONTROL AND FILTERING METHODS FOR CAUSES AND REDUCTION OF JITTER FORMATION ON OPTICAL BEAM: VARIOUS APPLICATIONS IN OPTICAL SPACE COMMUNICATION

by

Özgenç Subaşı

Submitted to Graduate School of Natural and Applied Sciences
in Partial Fulfillment of the Requirements
for the Degree of Doctor of Philosophy in
Electrical and Electronics Engineering

Yeditepe University
2022

CONTROL AND FILTERING METHODS FOR CAUSES AND REDUCTION OF JITTER FORMATION ON OPTICAL BEAM: VARIOUS APPLICATIONS IN OPTICAL SPACE COMMUNICATION

APPROVED BY:

Assoc. Prof. Dr. Koray K. Şafak ....
(Thesis Supervisor)
(Yeditepe University)

Prof. Dr. Duygun Erol Barkana ....
(Yeditepe University)

Assoc. Prof. Dr. Uğur Yıldıran ....
(Yeditepe University)

Assoc. Prof. Dr. Akın Delibaşı ....
(Coventry University)

Prof. Dr. Mehmet Turan Söylemez ....
(Istanbul Technical University)

DATE OF APPROVAL: ..../..../2022

I hereby declare that this thesis is my own work and that all information in this thesis has been obtained and presented in accordance with academic rules and ethical conduct. I have fully cited and referenced all material and results as required by these rules and conduct, and this thesis study does not contain any plagiarism. If any material used in the thesis requires copyright, the necessary permissions have been obtained. No material from this thesis has been used for the award of another degree.

I accept all kinds of legal liability that may arise in case contrary to these situations.

Name, Last name Özgenç SUBAŞI

Signature …………………………………….

ACKNOWLEDGEMENTS

I would like to thank to my thesis advisor Associate Prof. Dr. Koray K. Şafak who did not spare his support during the execution of this thesis. I am also very thankful to my former advisor Prof. Dr. Cem Ünsalan and also Associate Prof. Dr. Akın Delibaşı who greatly contributed to the work I have done on robust control and laser beam stabilization. I also appreciate my dear colleagues Harun Turan and Dr. Nurdan Baci from Electro-optics and Laser Systems Group at TÜBİTAK BİLGEM for their valuable contribution. I thank to Dr. Bilal Erol and Dr. Berk Altıner as well. Last but not least, I thank to my dear sister Özge Subaşı for her supportiveness in the process of writing my thesis.

ABSTRACT

CONTROL AND FILTERING METHODS FOR CAUSES AND REDUCTION OF JITTER FORMATION ON OPTICAL BEAM. VARIOUS APPLICATIONS IN OPTICAL SPACE COMMUNICATION

In this thesis, the control of a fast steering mirror, which is the core element of an adaptive optics system, is investigated to suppress the beam jitter.The main source of the jitter is taken as the atmospheric turbulence. The effect of the atmospheric turbulence on the beam jitter is experimentally determined with respect to the two different refractive index structure parameters. The mathematical model of the fast steering mirror based on the atmoshperic turbulence data is obtained using the system identification. In order to overcome implementation problems, the low order proportional integral-derivative (PID) type controllers, which minimize the $\mathcal{H}_\infty$ norm of the closed loop system, are designed in the centralized and the decentralized settings. In addition to this, the fixed order weighted $\mathcal{H}_\infty$ controller is based on the frequency characteristics of the atmospheric turbulence that is determined experimentally. Then, in order to show the effectiveness of the proposed low order PID type controller, the designed controllers are compared on the experimental setup. Finally, the simulation and the experimental results are presented. Comparison of advantageous and disadvantageous of centralized and decentralized controller architectures are discussed. In addition, the hysteresis nonlinearity arising from the piezo structure in FSM mirrors is discussed. It has been seen in the applications on the system that the controller performance can be increased if the nonlinearity that affects the closed loop controller performance is corrected.

ÖZET

OPTİK HÜZME ÜZERİNDE JITTER(SEĞİRME) OLUŞUMUNUN NEDENLERI VE AZALTILMASI İÇİN KONTROL VE FILTRELEME YÖNTEMLERI. OPTIK UZAY ILETIŞIMINDE ÇEŞITLI UYGULAMALAR

Bu tez çalışmasında, uyarlamalı optik sistemin temel elemanlarından olan hızlı yönlendirilebilen aynanın hüzme titreşimini bastırması araştırılmıştır. Titremenin ana kaynağı atmosferik türbülans olarak alınmıştır. Atmosferik türbülansın ışın titreşimi üzerindeki etkisi, iki farklı kırılma indisi yapı parametresine göre deneysel olarak belirlenir. Atmosferik türbülans verilerine dayalı hızlı direksiyon aynasının matematiksel modeli, sistem tanımlaması kullanılarak elde edilir. Uygulama problemlerinin üstesinden gelmek için, kapalı çevrim sistemin $\mathcal{H}_\infty$ normunu en aza indiren Oran İntegral Türev (PID) tipi kontrolörler, merkezi ve merkezi olmayan yapıda tasarlanmıştır. Buna ek olarak, sabit dereceli $\mathcal{H}_\infty$ kontrolörü, deneysel olarak belirlenen atmosferik türbülansın frekans karakteristiğine uygun ağırlıklandırma fonksiyonları seçilerek tasarlanmıştır. Daha sonra önerilen düşük dereceli PID tipi kontrolörün etkinliğini göstermek için tasarlanan kontrolörler deney düzeneğinde karşılaştırılmıştır. Son olarak simülasyon sonuçları ve deneysel sonuçlar sunulmuştur. Merkezi ve merkezi olmayan kontrolör mimarilerinin avantaj ve dezavantajlarının karşılaştırılması tartışılmıştır. Ayrıca FSM aynalarındaki piezo yapısından kaynaklanan histerezis nonlineeritesi tartışılmıştır. Kapalı çevrim kontrolör performansını etkileyen doğrusal olmama durumu düzeltilerek kontrolör performansının artırılabileceği deney üzerindeki uygulamalarda gösterilmiştir.

TABLE OF CONTENTS

LIST OF FIGURES

LIST OF TABLES

LIST OF SYMBOLS/ABBREVIATIONS

APT	Acquisition pointing tracking
CCD	Charged coupled device
COTS	Commercial off the shelf
FSM	Fast steering mirror
FSO	Free space optical
HDD	Hard disk drive
HEL	High energy laser
PSD	Position sensing detectors
PSA	Piezo stack actuator
LMS	Least mean square
MEMS	Micro electro mechanical structure
MIMO	Multi input multi output
MIT	Massachusetts institute of technology
MPI	Modified prandtl ishlinsky
NODE	Nanosattelite optical downlink experiment
PID	Proportional integral derivative
PI	Proportional integral
P-I	Prandtl ishlinsky
RF	Radio frequency
RLS	Recursive least squares

1. INTRODUCTION

In many optical applications, such as high-energy laser systems, free-space optical communication, scanning optical lithography, laser welding and cutting processes, the laser beam steering plays a crucial role in the performance of application. Focusing the laser beam on a prescribed target requires special control approaches due to disturbance effects (atmospheric turbulence, platform vibrations, etc.) that may occur in such applications. These disturbance effects cause the wavefront aberrations and yield beam jitter that is directly related with fluctuations of the laser beam propagation and therefore degradation of performance is inevitable.

FSM is widely used in optical systems to compensate jitter formation in laser beams. Bandwidth of FSM is very important to supress the beam jitter occurs due to the disturbances for high accuracy. Furthermore, it is very important for rapid response and high error attenuation, especially for broad-frequency error attenuation. FSM control system includes the feedback error signal that is obtained from a PSD, quadrant detector or CCD cameras. Closed-loop performance for an FSM depends on sampling frequency. Hence, high sampling frequency results in high closed-loop bandwidth. However, it is difficult to obtain high bandwidth FSM for precision tracking. FSM is used to correct first order aberrations while a deformable mirror is used to correct for higher order aberrations. Deformable mirrors are elastic mirrors whose surface can be reshaped, in order to correct optical aberrations and achieve wavefront control. Deformable mirrors are used in conjuction with wavefront sensors (mostly Shack-Hartman sensor) and real-time control systems in adaptive optics.

In the literature, the presented control approaches for the FSM aim to suppress the beam jitter caused by the atmospheric turbulence and the other disturbance effects. Since the atmospheric turbulence has time varying structure, the literature is abounded with many studies which adopt the adaptive control schemes.

1.1. PURPOSE OF THE STUDY

Main motivation in this thesis is to design and implement robust control algorithms for jitter rejection in laser beam stabilization task. For this purpose performances of actuator mechanisms and various sensors have been evaluated and performances has been compared.

Atmospheric Turbulence is one of the phenomea in laser beam propagation which causes reducing of laser power and distorting beam wavefront. The control algorithm design that can correct this phenomenon has guided the progress of this thesis. Generally APT systems is used to control laser beam pointing direction. FSMs are one of the basic elements used in APT mechanisms. It is aimed to develop control algorithms with FSM, which is used for fine tracking of laser beam.

Piezo type FSMs are preffered for many applications for higher resolution and bandwith. However, hysteresis nonlinearity is a major disadvatage about usage for this type FSMs. With compensating hysteresis nonlinearity in piezo FSM’s which degrades the control performance, it is aimed to increase the control and tracking performance of FSM's.

Especially the controller design for stabilization and tracking that could be used in space optical communication is targeted. In order to carry out these experiments, an experimental setup was prepared and the theoretical and practical results of studies were given based on the results obtained in experimental environment.

1.2. CONTRIBUTION OF THIS THESIS

In this study, practical and technological contributions of laser beam steering and control problem has been proposed.

For this problem, high processing power and memory requirements are needed for the application of adaptive and robust control methods currently used.The design of simple structured control algorithms that provide better performance with lower processing power compared to the methods in the literature and their application to the real system are discussed within the scope of this thesis.

In addition, it is widely known that the hysteresis in the internal structure of Piezo FSM, which is used for beam tracking, degrades the control performance when used for beam stabilization and tracking. The application disadvantage of non-linearity of piezo Fast Steering mirrors has been investigated and an infrastructure has been developed that will contribute to the practical use of piezo FSM. The contribution of hysteresis compensation made in a selected usage profile in open loop and closed loop control performance has been shown comparatively.

1.3. SCOPE OF THIS THESIS

As a first step in this study, system identification methods were applied to estimate the system parameters in the experimental setup set up in the optical laboratory for experimental studies on this problem. Since a model-based control design will be made, mirror dynamics were obtained experimentally with system identification. At this point, a marker base has been determined at frequencies including frequency characteristics of the fast steering mirror bandwith experimentally obtained atmospheric turbulence effect for the whole of the signs to be used to achieve mirror dynamics. As a result of the data obtained, a PID design and a fixed-order $\mathcal{H}_\infty$ output feedback controller were designed to minimize the $\mathcal{H}_\infty$ norm of the transfer function from the disturbance input to the performance output. Simulation of laser beam fluctuation on target at 1km distance with a certain ${C_n}^2$value has been used as disturbance signal. The same calculated disturbance signal was used in the testing of all designed controllers.The performance of the controllers designed by simulation studies is examined.

In addition, controllability due to hysteresis in piezo FSMs and controllability with linear controllers becomes somewhat difficult. In literature there are various tecniques for modelling and compensating hysteresis nonlinearity arising from piezo structure of the Fast Steering Mirrors. In this thesis, methods for anti-hysteresis compensated open-loop and closed-loop control are proposed to compensate for hysteresis non-linearity for piezo-fast steering mirrors.

In Chapter 2, space optical communication experiments and other experiments such as high power laser beam stabilization applications also evaluated for completely definition for the beam stabilization problem. A general literature review on control methods for laser beam acquisition and pointing systems and their usage areas and applications in optical satellite communication is given. Chapter 3 provides information about basic robust control methods. In Chapter 4, information about the experimental setup in the lab environment and system identification method is given.In Chapter 5, information about the developed and applied control methods to the system for simulated atmospheric disturbance attenuation is given.In Chapter 6, the nonlinear hysteresis behavior of the piezo fast steering mirrors has been examined and it has been shown how the performance of the system can be increased when hysteresis compensation is applied for open-loop and closed-loop control control.

2. LASER BEAM POINTING AND TRACKING SYSTEMS AND APPLICATIONS IN SPACE OPTICAL COMMUNICATION

Laser beam steering technology is used in wide range of optical applications such as high-energy laser systems, free-space opical communication, scanning optical lithography, laser welding and cutting of materials processing and various applications for biomedical system. The control problem is to precisely position the center of a laser beam with minimal impact from external disturbances to a desired location on a target plane away from the laser source. In applications, the most common source of jitter is the turbulence effect that the laser beam encounters as it passes through the atmosphere. Furthermore, the vibration of the optical platform and the movement of the optical components cause jitter, resulting pointing inaccuracy.

Free-space optical communication is a technology that uses light emitted in free space for wireless data transmission[1].

Free space laser communication is also challenging and more critical technology comparing with RF communications. High data rates, data transfer capability to long distances and secure communication capability make it preferable for military and secure communication. In order to achieve optical communication, the beams of light coming out of the devices must follow each other at as narrow an angle as possible. APT systems are used to perform this feature.

APT systems consisting of Coarse Tracking System and Fine Tracking System are common. Coarse Tracking System provides a wide-field-of-regard and the Fine Tracking System a provides fast alignment of the laser beam to the receiver part. Coarse tracing side is responsible for reducing pointing errors and estimation of velocity and position of the beam for continuty of tracking performance. Fine tracking is responsible for accurate tracking of laser beam with low divergence error.

Space optical communication is also one of the most important areas of optical communication and makes it possible to transfer high-speed data to long distances in space because of the high connection speed and the small losses that weaken the laser beam in the atmosphere. Atmospheric scintillation is an important parameter that affects communication performance in optical communication applications around the world. However, since there is no atmosphere in space, the effect of Atmospheric scintillation in inter-satellite communication is small, but will be important because laser beam passes through the atmosphere in communication between the ground and the satellite communication.

In addition, since the operation of different mechanisms (cryocooler, etc.) on the satellite causes vibration of the laser beam, that will reduce the communication performance. With APT mechanisms, this vibration can be decreased and the communication performance can be corrected.

2.1. ATMOSPHERIC TURBULENCE EFFECTS

Atmospheric turbulence is one of the most important sources of wave front distortion, optical jitter. Due to its atmospheric structure, it contains air bubbles of varying dimensions with different humidity and temperature values. Due to the flow of air in the atmosphere, these bubbles are constantly in motion. As the light travels through the atmosphere, it passes through the air bubbles and is diffracted. The clippings in the stars in the sky, especially in summer, are caused by atmospheric turbulence. In order to work effectively with adaptive optical systems essential to overcome such problems, it is necessary to obtain a suitable model of atmospheric turbulence or to know the frequency band. Here, ${C_n}^2$represents a quantitative measure of the intensity of optical turbulence. if the ${C_n}^2$ value of the medium through which the laser beam of a certain power passes through the atmosphere is known, the mean clipping variance of the laser beam sent to a certain distance can be mathematically calculated.

Hence if we know distribution, we can suppress the jitter with less complicated controller structrures. Combined effect of jitter and turbulence in the performance of laser tracking of small targets mentioned in [2]. Intensity fluctuation of the sattellite to ground laser beam has been modelled which takes into account atmospheric turbulence in [3].

Changes in temperature, pressure, wind speed, humidity and other phenomena affect the refractive index of the atmosphere. This effect creates a turbulence behavior that can be expressed by the Navier-Stokes equation. Because the Navier-Stokes equation is a nonlinear equation and highly sensitive to the initial condition, statistical methods have been used to express the turbulence dynamics [4]. Kolmogorov's statistical approach to atmospheric turbulence is very useful for modeling such fluctuations. In 1941 the famous mathematician Andrey Nikolaevich Kolmogorov laid the foundation for the atmospheric turbulence models used today. His 1941 study on energy dissipation in a turbulent environment pioneered this field. Turbulence occurs in large outer-scale structures and spreads to smaller scale structures. When this energy transmission reaches a small enough structure, it disappears in heat with viscosity forces[5]. In the following years, Tatarski developed this theory of electromagnetic wave propagation in the turbulence layer by using this energy transfer in turbulence flow and methodology [6]. Inspired by the work of Kolmogorov and Tatarski in the following years, Fried presented measurable parameters that could be used to characterize the severity of atmospheric turbulence [7].

Kolmogorov's 3D power spectrum,

$$\Phi_n(\kappa) = 0.033{C_n}^2\kappa^{-11/3} \tag{2.1}$$

Where, κ is the spatial angle frequency, and ${C_n}^2$is the structural constant that characterizes the strength of the fracture. The ${C_n}^2$unit $m^{-2/3}$ is a constant used to measure the strength of the atmosphere.This structure constant changes regionally with height and time [8]. In other words, daytime measurements are at high values, constant throughout the night and minimum values at sunset and birth. There are many studies on the measurement of ${C_n}^2$constant in the literature.In these studies, the relationship between ${C_n}^2$and altitude has been revealed based on the experiments and observations from regional measurements in general.

In addition to the model produced by Kolmogorov, the effect of these variables on higher frequencies is expressed by using them on internal L0 and external L0 scales obtained from experimental data in the literature.

In this context, the developed Von Karman spectrum,

$$\Phi_n(\kappa) = 0.033{C_n}^2(\kappa^2 + f_0^2)^{-11/6}e^{-\frac{\kappa^2}{f_m^2}} \tag{2.2}$$

where f_o = 2π / L0 and f_m= 2π / l0. From these scales that limit Kolmogorov flow, the L0 value of the external scale is obtained. Although it varies from measurements to measurements, it varies between 20-30 m and the l0 value of the internal scale varies between , 2-12 mm [9], [10]. The ${C_n}^2$ structural constant, which characterizes the strength of the fracture, has values approximately $10^{-13}m^{-2/3}$ where turbulence is strong and $10^{-18}m^{-2/3}$ at high altitudes where the turbulence is weak. In this context, data has been obtained at two different ${C_n}^2$ values, weak and strong to test designed controller performance. Thus, how far the laser deviates from the X and Y plane has been determined mathematically and tabulated.

The laser beam propagation values used in this study is obtained using LAtmoSim software which is a Gaussian beam boosting code developed by TUBITAK (the Scientific and Technological Research Council of Turkey). LAtmoSim® uses the method of creating phase screens with Kolmogorov spectral power distribution with split-step Fast Fourier Transform (FFT) algorithm to demonstrate laser propagation in atmospheric turbulence.

2.2. VIBRATION MODELLING IN SATELLITES

When an optical satellite communication terminal is mounted on the satellite, vibrations caused by the movement of other payloads on the satellite have a negative effect on the performance of the communication.These effects should be taken into account when designing a terminal [11].

The SILEX system is the first optical communication terminal used in satellites [12]. Using the power spectrum of the SILEX platform vibration used by ESA in the design of SILEX terminals, controller design have been proposed to reduce vibrations in the terminal [13]. Figure 2.1. shows the spectrum model of the satellite platform vibration, which is used by the European Space Agency (ESA) in design of SILEX terminal.

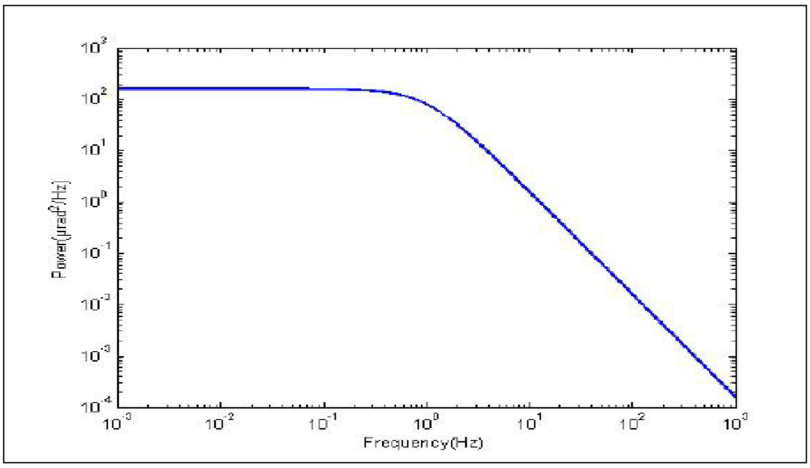

Figure 2.1. Power spectral density of vibration model data

With this model, power spectrum of the satellite platform vibration can be expressed as:

$$S(f) = \frac{160}{1+f^2}\left(\frac{urad^2}{Hz}\right) \tag{2.3}$$

In addition to the atmospheric scintillation power spectral density, power spectral density of the satellite vibration model was also taken into account in order to derive the mathematical model of the APT system to be used in the optical communication between earth and satellite.

In [14] they have been designed filter as the vibration transfer model to simulate the vibration between satellite and the payload. The filter's transfer function is formula (2.4).

$$G_f(s) = \frac{3000}{s+6.28} \tag{2.4}$$

2.3. COARSE TRACKING AND ESTABLISIHING LINE OF SIGHT IN SATTELLITE OPTICAL LASER COMMINICATION SYSTEMS

In laser communication applications, coarse tracking mechanisms are used to ensure that the moving terminals have a rough view of each other. The coarse block fulfills the task of keeping the laser beam within line of sight in certain accuracy. After the terminals are roughly aligned to each other's line of sight, the alignment error can be reduced to lower values with precise tracking mechanisms, ensuring maximum power transfer of laser beam to the opposite terminal, ensuring that communication is carried out without breaking and at maximum speed.

NODE has been designed and manufactured using COTS devices in MIT, is a good experiment and simulation study of space optical communication.

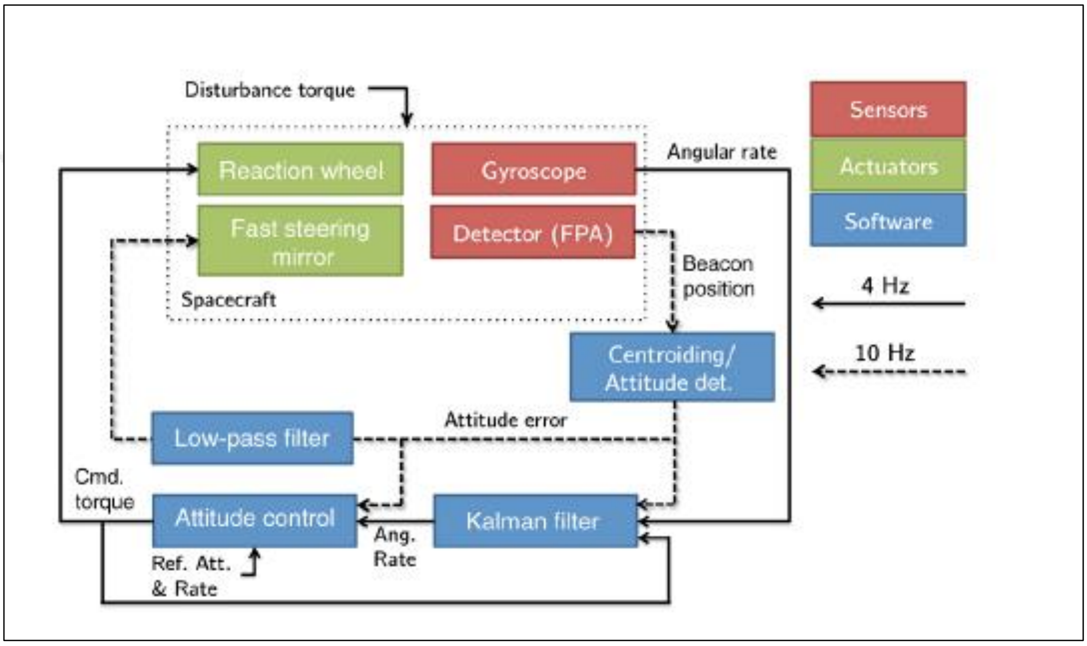

Figure 2.2. Fine tracking and coarse tracking part of the nanosatellite laser communication system NODE [15]

Including coarse tracking and fine tracking control simulation block diagram, NODE system is shown in Figure 2.2. Coarse tracking mechanism created using reaction wheel and gyro. The line of sight angle obtained only when the Coarse pointing control cycle is 2.32 mrad. The closed loop coarse pointing control cycle operates at 4hz. A faster cycle of 10 Hz is used as a precision tracking mechanism and reduces the alignment angle to 0.3 mrad.

Another paper describing Inter-Satellite Laser Communication System is in [16], which consists two level of stages for estabishing maximum power of laser beam. Coarse pointing for rough tracking of gimbal mechanism that includes a simple velocity and position control loop. Fine tracking control block include three stages, First block is fast stering mirror for transreceiver pointing, second stage is Point Ahead Mirror for transmitter-receiver misalignment adjustment. Third part of lower level control block is linear stage for shaping laser beam defocus.

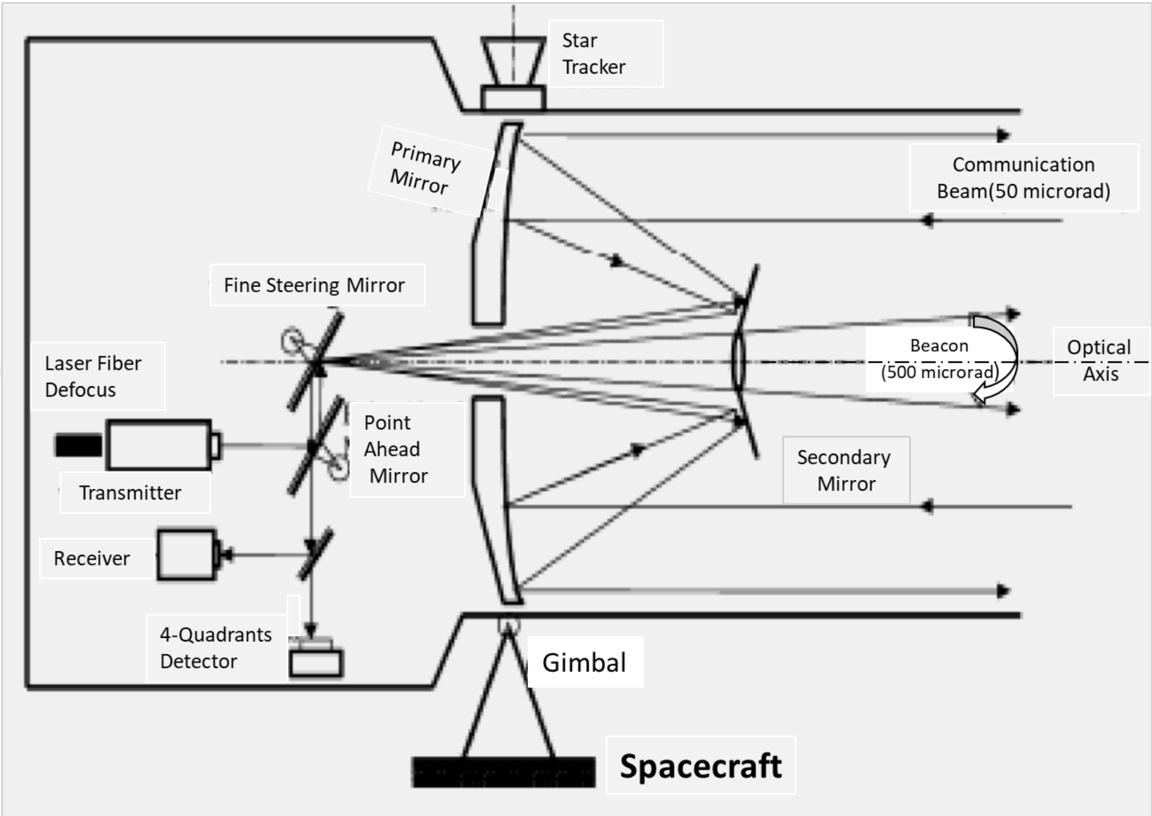

Figure 2.3.Conceptual diagram of acquisition and tracking system of intersatellite laser communication system(revised) [16]

For predicting future state of the system and smoothing fluctuations in line of sight pointing systems, Kalman Filters are widely used [17]. Due to slow variations of line of sight within the telescope classical kalman filtering provides efficient technique for on board estimation and processing [18].

In many laser pointing and tracking applications, the Kalman filter is generally used in the coarse tracking section. In [19] Kalman filter is used for pointing the high power laser target for filtering the target position coordinates from the GPS data and for determining the target speed in case the target is lost by the coarse tracking camera. Kalman filter is used as a safety barrier when laser beam is lost for air to air laser Communication applications in APT control system approach [20].

Kalman Filter aided cooperative optical beam tracking mechanism between two moving vehicle terminals has been proposed in [21]. The optical jitter control system based on FPGA and cameralink cameras on a multi beam laser coherent combining system has been introduced [22].

Also other control strategies for coarse pointing of laser beam in acquisition tracking and pointing applications has beeen proposed. For space optical communication, coarse tracking applications for rejecting disturbance and minimizing tracking error and disturbance Active Disturbance rejection controller proposed [23]. Fuzzy supervised PID controller for coarse tracking experiment method has been applied with TMS320F2812 DSP card [24]. Robust disturbance compensator algorithm to improve Japanese satellite HALCA’s attitude control for astronomical observation missions have been presented in [25]. Cooperative type synchronized fine pointing and coarse pointing controller type for improvement of disturbance rejection performance of APT systems used for free space optical communication is proposed in [26].

2.4. FINE TRACKING CONTROL INCLUDING JITTER REJECTION METHODS

FSMs are widely used as fine tracking components in APT systems to compensate for jitter caused by atmospheric turbulence and mechanical vibration. Bandwidth of FSM is very important to suppress the beam jitter occurence due to the disturbances for high accuracy. Furthermore, it is very important for rapid response and high error attenuation, especially for broad-frequency error attenuation. FSM control system includes the feedback error signal that is obtained from a PSD, quadrant detector or CCD cameras. Closed-loop performance for an FSM depends on sampling frequency. Hence, high sampling frequency results in high closed-loop bandwidth. However, it is difficult to obtain high bandwidth FSM for precision tracking. A fast steering nirror is used to correct first order aberrations while a deformable mirror is used to correct for higher order aberrations. Deformable mirrors are mirrors whose surface can be reshaped, in order to correct optical aberrations and achieve wavefront control . Deformable mirrors are used in conjuction with wavefront sensors (mostly Shack-Hartman sensor) and real-time control systems in adaptive optics.

Since jitter characteristics are time varying, studies in the literature have used controller structures whose parameters can be adjusted dependent on noise characteristics instead of fixed gain controllers. Recent research has developed novel adaptive control methods that can track and reject non-stationary, high bandwidth jitter in laser beams.These methods use adaptive filters that monitor disturbance characteristics, and adapt feedforward and/or feedback controller parameters that drive actuators to suppress jitter. In the literature, some control studies have been conducted to address this problem.The most common method in the feedback-type control is the linear-time-invariant controller, which includes techniques such as classical PID controller. In the presence of time-varying or uncertain disturbances, jitter control systems using fixed-gain feedback control loops cannot operate effectively. Because of the broad frequency content and time-varying nature of typical jitter and model uncertainty associated with both the jitter and the plants, adaptive control and robust control methods are required to minimize the effect of jitter in realistic applications.

Laser beam jitter control applications using RLS adaptive filter [27, 28] and LMS adaptive filter [29] has been proposed which requires to measure reference signal with an additional sensor. Adaptive feedback control method using Q-parameterization is reported in [30] where the LMS algorithm is used for the Q-parameter adaptation. Also nonlinear adaptive controller which models the plant nonlinearities with a new liquid Crystal beam steering device has been proposed in [31]. Adaptive filter structures that contains higher order FIR filters have better performances to reject disturbances but they are poor in sudden transients, higher order adaptive filters could produce larger transient errors. Instead of fixed order, variable order have been used in [32] to cope with sudden changes and optimum noise rejection performance together. Without adaptive filtering Q- parameterization has also been applied to similar problem which uses two different types of filters for Q-parameter , each suppressing frequencies in different frequency bands [33].

FSM-based adaptive jitter reduction systems which can be used to reduce jitter in satellite communication is proposed in [34]. Also method for jitter reduction proposed in [30] optimizes the stable controller coefficients found by Q-parameterization method with LMS adaptive filter. A similar method has been proposed by [35] to reduce satellite vibrations by using RLS adaptive filter so that filter coefficients can be adjusted faster.By making use of image processing algorithms, the control algorithm design using CCD-based cameras in the control loop can also be made for fine tracking system design with FSM [36]. In the case of weak-damped MEMS tilt mirrors, the problem of disturbance suppression with the μ-synthesis method and adaptive control is addressed in [37].

A similar adaptive control structure in the aforementioned studies and the performance improvement has been established using two different disturbance sources [38]. FSM1 is mounted on an electronically controlled shaker and another disturbance source in this setup is FSM2 is used to add disturbance to laser beam which is driven with designed disturbance sequence.

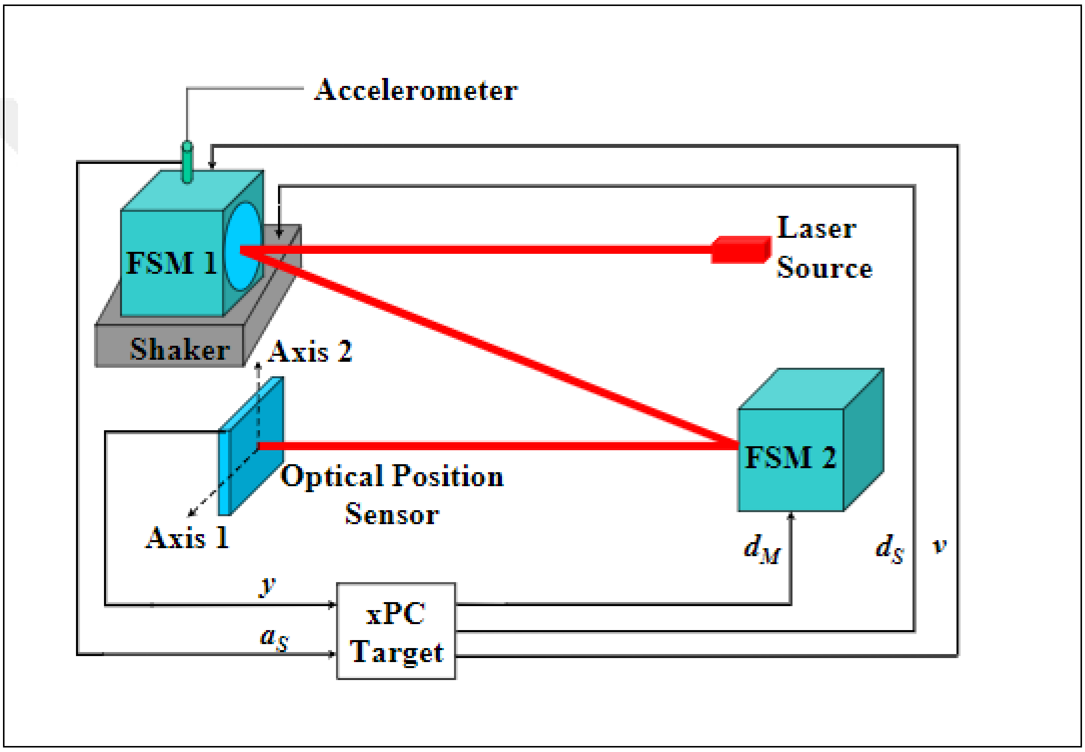

Figure 2.4. Block diagram of experimental setup [38]

In addition to the fast-steering mirrors, permeable liquid crystal beam orientation modules are also used to correct the optical jitter. An adaptive control approach has been developed by considering the nonlinear dynamics of the liquid crystal beam orientation module in the study [39].

Teledyne Scientific Company has developed the transmissive liquid crystal tip-tilt corrector leverages dual frequency liquid crystal optical phased array technology requirements for a compact, transmissive, highspeed tip-tilt correction device alternative to FSM. Liquid crystal beam steering device has no moving parts that differ from FSM's and they provide low power consumption [40].

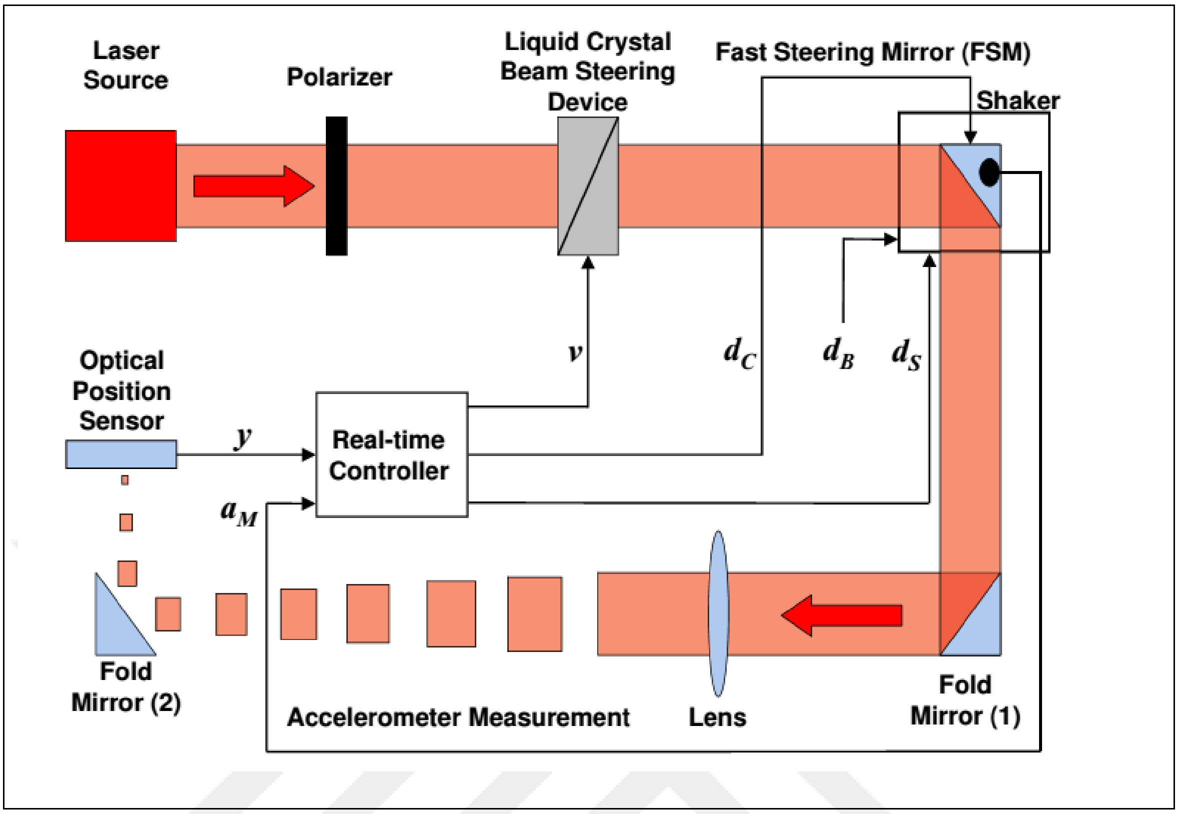

Figure 2.5. Diagram of the experiment [39].

Block diagram and electrooptical components that are used in the diagram can be seen in Figure 2.5. Here $d_b$and d_s are signals used to vibrate the vibration motor on which the FSM is mounted. d_c is disturbance signals given to FSM to distort laser beam. Rms values of the noise generated at the beam output are given comparatively with the adaptive controller algorithm designed to reduce the effect of noise injected into the system by creating noises at different bandwidths.

In addition, there are also studies conducted in the field of optimal control. LQR type controllers have also found use in laser beam pointing and control systems where restricted control signal is required [42, 43]. A study [44] comparing PID and more basic controller structures such as lead compensator and LQR was also performed.

2.5. PIEZO FAST STEERING MIRRORS

Piezo-electric actuators produce a linear motion resulting from the elongation and contraction of crystal and ceramic materials under high voltage. The amount of movement that the piezo actuator can deliver is linearly proportional to the amount of applied voltage. Linear motion results from the elongation and contraction of crystal and ceramic materials under high voltage. The amount of movement does not depend on the dimensions of the piezoelectric material. Therefore, the amount of movement is increased by stacking the piezoelements on top of each other. For example, an actuator with 2 piezo elements will have twice the displacement of the voltage applied to a single piezo element. This is how Piezo Stack Actuators are created [45].

FSM represents a mirror mounted on actuators that can produce fast and precise movements. Piezo Stack Actuators are usually linear motion elements. To produce angular motion around any axis, two actuators are used, each moving in opposite directions with respect to each other.

Feedback can be provided from capacitive sensors placed within the FSM or by images taken with imaging elements such as PSD, camera or quadrant detector from the point where the laser beam controlled by the FSM falls.

In Figure 2.6(a) the reflection of the laser beam from the mirror mounted on the FSM and falling onto the PSD is shown in the axial plane. In Figure 2.6(b) also provides a representation of the dynamic equivalent model of piezo stack actuator that enable movement on the y-axis. In Figure 2.6(c) is also shows distribution of actuators in FSM.

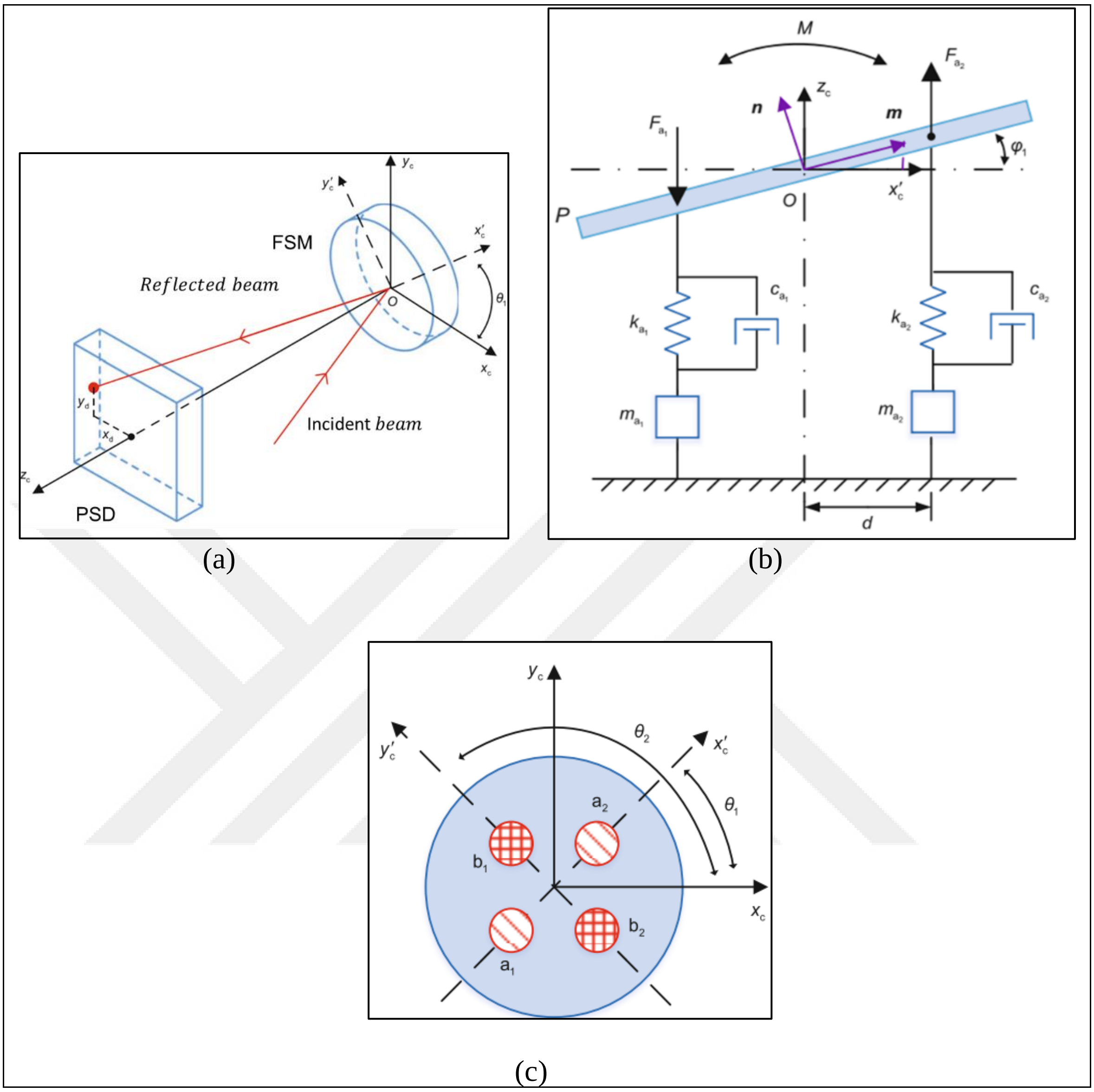

Figure 2.6. Operating principle of FSM (a) Geometric configuration of FSM and PSD in cartesian coordinates, (b) Mirror surface deflected by a pair of push and pull actuators in x_c' , (c) distrubution of the actuators in FSM [46].

Linear equations can be used for approximate modelling of FSM. The equation between the mirror's torque M and the angular position φ_1 is given as follows [46, 47].

$$M = [J + (m_{a_1} + m_{a_2})d^2]\ddot{\varphi}_1 + (c_{a_1} + c_{a_2})d^2\dot{\varphi}_1 + (k_{a_1} + k_{a_2})d^2\varphi_1 \tag{2.5}$$

where J is the moment of inertia, d is the distance between the center of the mirror and actuator, m_{a_1} and m_{a_2} are masses, c_{a_1} and c_{a_2} are damping coefficients, and k_{a_1} and k_{a_2} are elastic coefficients of the two actuators. It can be written that the applied torque and the applied control signal are proportional to the coefficient p_1. And same torque values is equal and in same direction as $F_{a_1} = -F_{a_2}$

$$F_1 = 2F_{a_1} = p_1 u_1 = m_1 \ddot{\varphi}_1 + c_1 \dot{\varphi}_1 + k_1 \varphi_1 \tag{2.6}$$

Equation of control signal and angle of motion in an axis

$$u_1 = \frac{1}{p_1}(m_1 \ddot{\varphi}_1 + c_1 \dot{\varphi}_1 + k_1 \varphi_1) \tag{2.7}$$

For the other axis can be given as,

$$u_2 = \frac{1}{p_2}(m_2 \ddot{\varphi}_2 + c_2 \dot{\varphi}_2 + k_2 \varphi_2) \tag{2.8}$$

Piezoelectricity is one of the fundamental processes for electromechanical energy conversion. Electric field is used for mechanical compression/extension in piezoelectric material.This fundamental property of piezoelectricity has led to the use of such materials for the manufacture of various piezoelectric transducers, including actuators and sensors. with piezoelectric ceramic materials such as lead-zirconate-titanate Pb(Zr, Ti)O3 crystal called PZT [48] shows the polarization process for a piezoelectric actuator. As seen in Figure 2.7-a, the electric dipoles of the ceramic materials are randomly oriented.The position of the electric dipoles does not change unless there is an external electric field.When an electric field is applied, the electric dipoles align themselves in a direction close to the applied electric field, and the crystals expand the material in the direction of the applied electric field, as shown in Figure 2.7-b. However, when the electric field is removed, the electric dipoles will not fully return to their original positions. this is also shown in -Figure 2.7-c.

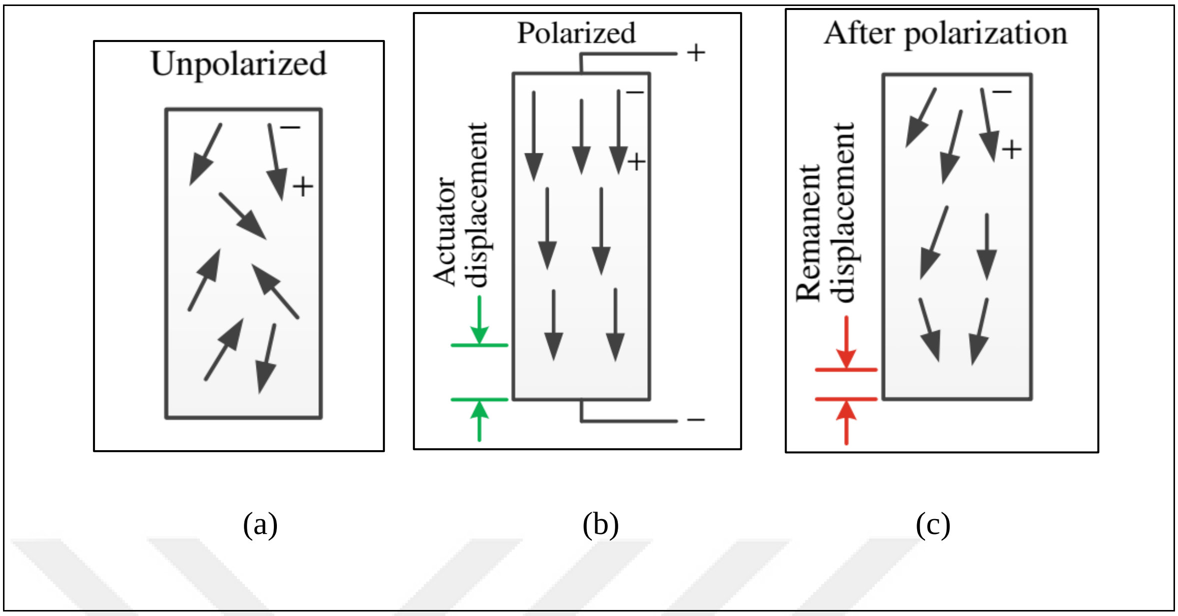

Figure 2.7. Polarization and depolarization process for piezoelectric actuator [48]

The nonlineer properties of FSM piezoelectric material used in FSM's can have a performance-reducing effect, especially in reference tracking. It has a little effect on the control systems used to suppress external disturbances, but can affect performance in the control systems used for precise reference tracking. In the thesis study, the controller mechanisms used for both situations were examined in the following sections.

3. ROBUST CONTROL METHODS

3.1. BASIC REQUIREMENTS FOR FOBUST CONTROL

Control systems are used in many areas of critical importance in our lives, from today's technological production processes and autonomous systems requiring precise positioning to space technology. Control systems are based on the principle of feedback. It is based on the principle of applying a corrective signal formed by the difference between the reference value and the system response to the entrance of the system.

For the design of the control system, the mathematical model of the system to be controlled must be known. In addition, the nonlinear behavior of the systems should be taken into account within the system model. Changes in the parameters of the system model over time, noises in measuring sensors and external disturbances play an important role in the design of control systems. There are two basic disciplines for the design of control systems by reducing or eliminating such effects, such as adaptive control and robust control.

The main purpose of the 10 m astronomical telescope whose block diagram is shown in Figure 3.1. is to collect and focus light from stars with the help of a large concave mirror. The mirror is used to adjust the position of 3 piston mirrors on 3 axes for each segment divided into 36 segments. There are capacitive type sensors to measure the displacements defined by the y vector between both segments. The multivariate feedback control loop is shown below so that the displacements of each of the segments are at the pre-calculated point with the vector r.

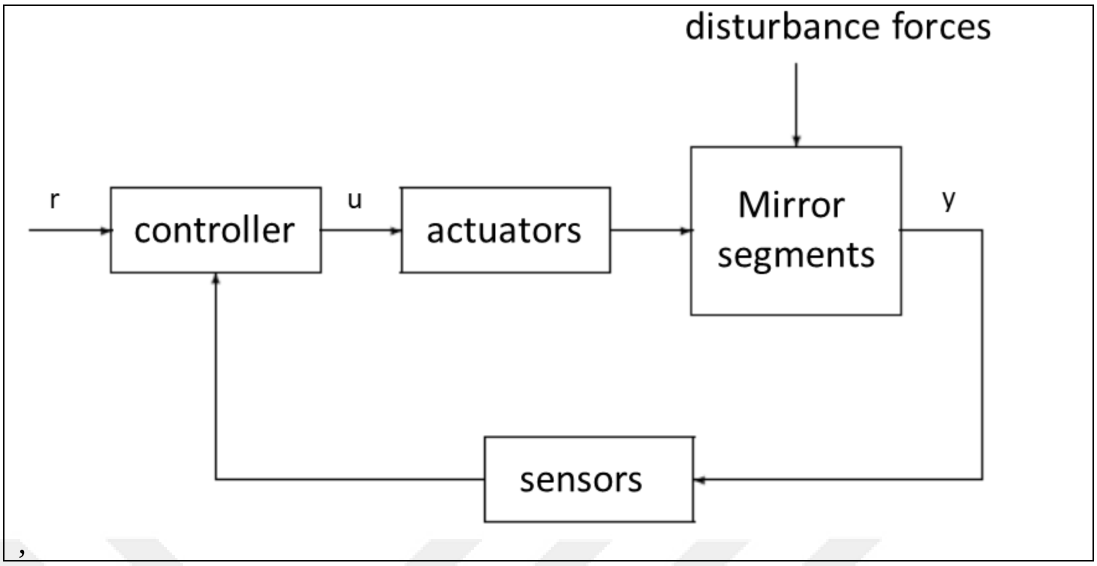

Figure 3.1. Block diagram of Keck telescope control system. [49]

In the telescope control system, there are disturbances such as the wind blowing at different intensities, the change in temperature, and the change of the gravitational force as the position of the mirror changes. In addition, the dynamic behavior of segments of the mirror, actuators and sensors can be modeled with limited accuracy.

Robust control methods are used to minimize the effects of the disturbances in the controlled systems and the uncertainties in the modeling on the controller performance.

3.2. MATHEMATICAL BASICS

3.2.1. Vector Norms

For a given vector x with length n a function $\|\cdot\|: \mathbb{R}^n \rightarrow \mathbb{R}$ is called a vector norm

The most commonly used vector norms belong to the family of p-norms, or ℓ_p-norms, which are defined by

$$\| \mathbf{x} \|_p = \left(\sum_{i=1}^{n} |x_i|^p \right)^{1/p} . \tag{3.1}$$

For p=1 ℓ_1 norm is

$$\| \mathbf{x} \|_1 = |x_1| + |x_2| + \cdots + |x_n| \tag{3.2}$$

For p=2 ℓ_2 norm is defined as

$$\| \mathbf{x} \|_2 = \sqrt{x_1^2 + x_2^2 + \cdots + x_n^2} = \sqrt{\mathbf{x}^T \mathbf{x}} \tag{3.3}$$

For p=∞ ℓ_∞ norm is defined as

$$\| \mathbf{x} \|_\infty = \max_{1 \le i \le n} |x_i| \tag{3.4}$$

3.2.2. Singular Value Decomposition

The singular value decomposition method is used to extract the dominant features from the matrices and to reduce the size [50]. In this way, the matrix is conceptually represented by a smaller data space. The singular value decomposition method is used for classification and size reduction. In control systems, it is used for frequency domain analysis in multi-input, multi-output systems. The singular value decomposition is given by the following equations,

Let transfer function $G \in \mathbb{C}^{l \times m}$

$$G = U \Sigma V^* \tag{3.5}$$

$$\begin{aligned} U &= [u_1, \dots, u_l] \in \mathbb{C}^{l \times l} \\ V &= [v_1, \dots, v_m] \in \mathbb{C}^{m \times m} \end{aligned} \tag{3.6}$$

Are unitary martices

$$\Sigma = \begin{bmatrix} \Sigma_1 & 0 \\ 0 & 0 \end{bmatrix} \qquad \Sigma_1 = \begin{bmatrix} \sigma_1 & 0 & \dots & 0 \\ 0 & \sigma_2 & \dots & 0 \\ \vdots & \vdots & \ddots & \vdots \\ 0 & 0 & \dots & \sigma_p \end{bmatrix} \tag{3.7}$$

The diagonal of the Σ_1 matrix is called the singular values of the G matrix. Symbolic representation is as in (2.4).

$$\sigma_1 > \sigma_2 > \ldots > \sigma_p \tag{3.8}$$

$\bar{\sigma}$ is denoted as the largest singular value of G and $\underline{\sigma}$ is the the smallest one.

3.2.3. $\mathcal{H}_\infty$ Norm

H infinity norm gives maximum peak value in BODE plot of strictly proper transfer function G(s) in SISO systems. For MIMO Systems, the highest gain value that inputs can receive at any frequency value determines the $\mathcal{H}_\infty$ norm.

$$\| G(s) \|_\infty = \sup_{\omega} \bar{\sigma}(G(j\omega)) \tag{3.9}$$

As shown in Figure 3.2., the highest of singular value for MIMO systems determines the system's $\mathcal{H}_\infty$ norm.

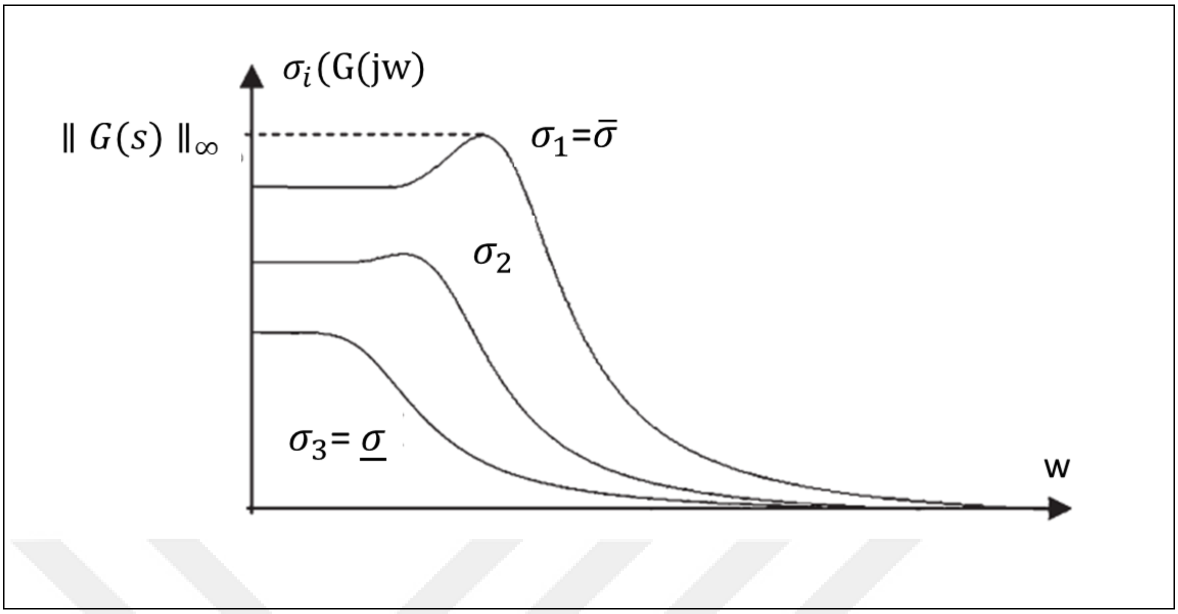

Figure 3.2. Singular values and $\mathcal{H}_\infty$ norm of a MIMO system [51].

3.2.4. $\mathcal{H}_2$ Norm

The $\mathcal{H}_2$ norm gives the average gain of the system given by G(s) in the frequency domain.Let G(s) be a stable transfer function matrix of MIMO $p \times m$ system, $\mathcal{H}_2$ norm is given as,

$$\| G(s) \|_2 = \left(\frac{1}{2\pi} \int_{-\infty}^{+\infty} \text{Trace } (G(j\omega)G^*(j\omega)) d\omega \right)^{1/2} \tag{3.10}$$

3.2.5. Linear Fractional Transformation

In $\mathcal{H}_2$ and $\mathcal{H}_\infty$ controller structures, minimizing gain from output to input is important. For this reason generalized controller structure is mainly used. In generalized controller structure input vectors w,u and output vectors is z,v. The representation of the closed-loop control system in the generalized controller structure is shown Figure 3.3.

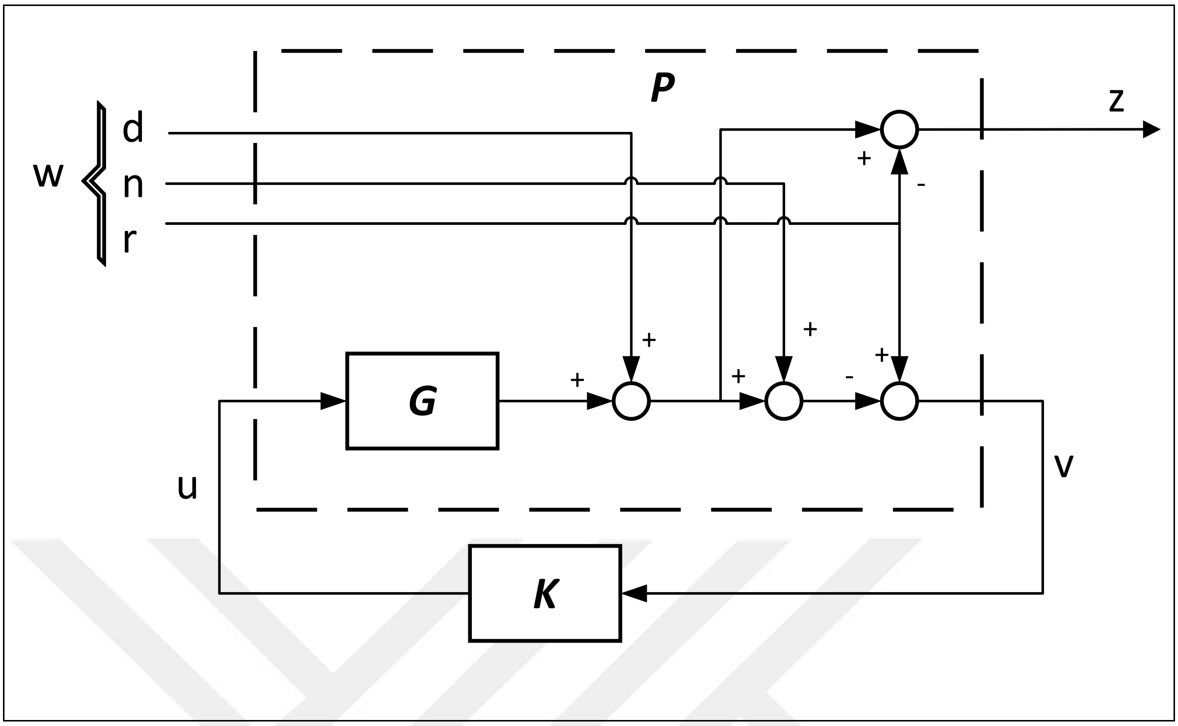

Figure 3.3. Closed loop control system in generalized structure

Shown systems and signals are

- P - generalized system, K – controller, G - system
- w - exogeneous inputs such as disturbance, reference, noise (d, r, n)
- z - exogeneous outputs such as error, control signal (e, u)
- u - control signal
- v - measurements,

Control signal can be taken as output in generalized structure, based on this block diagram, generalized control system structure can be seen in Figure 3.4.

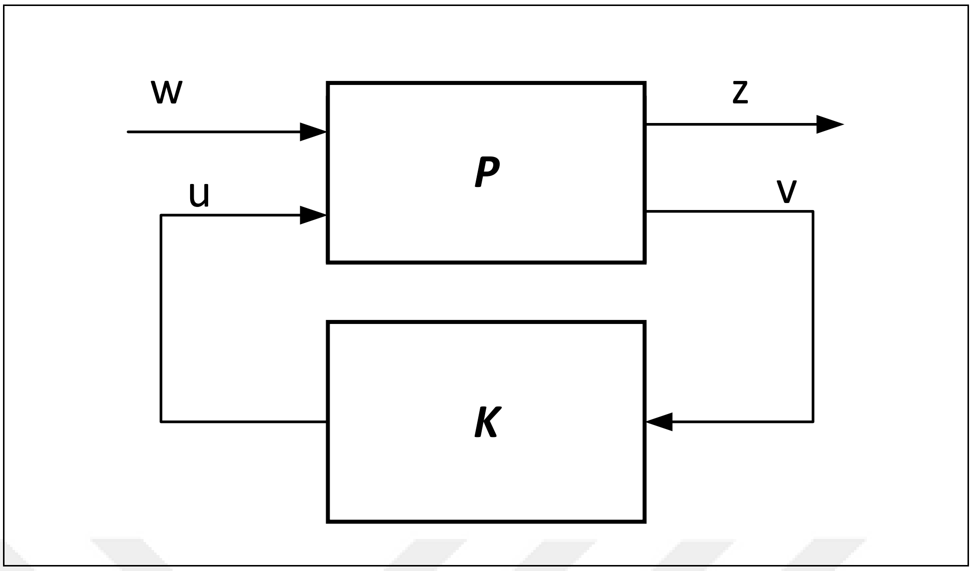

Figure 3.4. Generalized control system structure

State space equations of generalized plant:

$$\begin{bmatrix} z \\ v \end{bmatrix} = \begin{bmatrix} P_{11} P_{12} \\ P_{21} P_{22} \end{bmatrix} \begin{bmatrix} w \\ u \end{bmatrix} \text{ where } P = \begin{bmatrix} A & B_1 & B_2 \\ C_1 & D_{11} & D_{12} \\ C_2 & D_{21} & D_{22} \end{bmatrix} \tag{3.11}$$

Controller equations:

$$\text{z}\, u = Ky \text{ where } \quad K = \begin{bmatrix} A_K & B_K \\ C_K & D_K \end{bmatrix} \tag{3.12}$$

Objective: minimize gain from w to z, with appropriate weights/scaling, make gain smaller than one.

As shown in Figure 3.3. controller closes the loop from y to u. Generalized control structure is shown in

$$\begin{gathered} z = P_{11}w + P_{12}u \\ y = P_{21}w + P_{22}u \\ u = Ky \end{gathered} \tag{3.13}$$

solving for u

$$u = KP_{21}w + KP_{22}u \tag{3.14}$$

and solving for z gives:

$$z = [P_{11} + P_{12}(I - KP_{22})^{-1}KP_{21}]w \qquad (3.15)$$

Closed loop transfer gain from w to z is given with

$$T_{w \to z}(P, K) = [P_{11} + P_{12}(I - KP_{22})^{-1}KP_{21}] \qquad (3.16)$$

3.3. CENTRALIZED AND DECENTRALIZED CONTROLLER STRUCTURES FOR MIMO SYSTEMS

Centralized and decentralized structured controllers are used in MIMO systems. Controllers can be structured as decentralized where each axis can be controlled independently or as centralized where systems that are difficult to control due to inter-axis interaction. . Both of the structures can be used in MIMO controllers. For the two input two-output system, the representations of both types of controllers can be seen in Figure 3.5. and Figure 3.6.

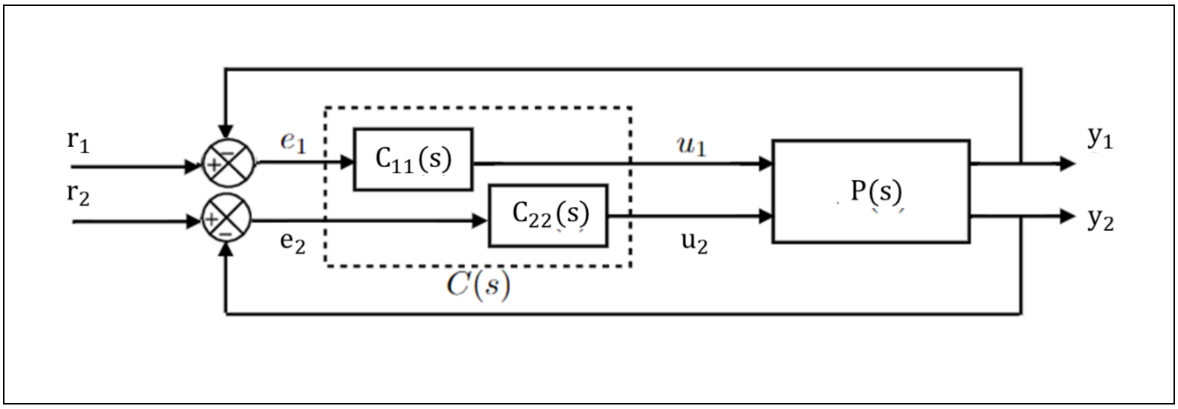

Figure 3.5. Decentralized control structure

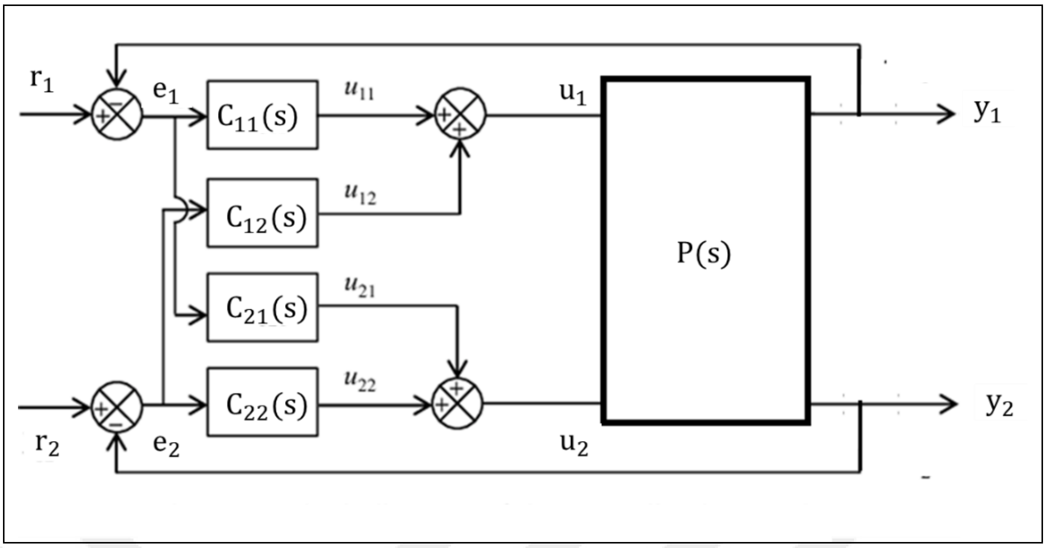

Figure 3.6. Centralized controller structure

3.4. FREQUENCY DOMAIN PERFORMANCE AND LOOP SHAPING METHODOLOGY

Loop shaping can be made sense as shaping the BODE diagram of the closed cycle control system. To explain this, firstly we need to define the block diagram of closed loop control system. Also equations that defines Sensitivity and Cosensitivity criteria of the closed cycle control system have to be given. In addition, in loopshaping procedure, the loop gain requires to be adjusted to guarantee phase margin and gain margin to guarantee the stability of the system. When designing the controller, frequency domain behaviors are analyzed via BODE Plot and stability margins via Nyquist diagram.

3.4.1. General Closed Loop System Equations

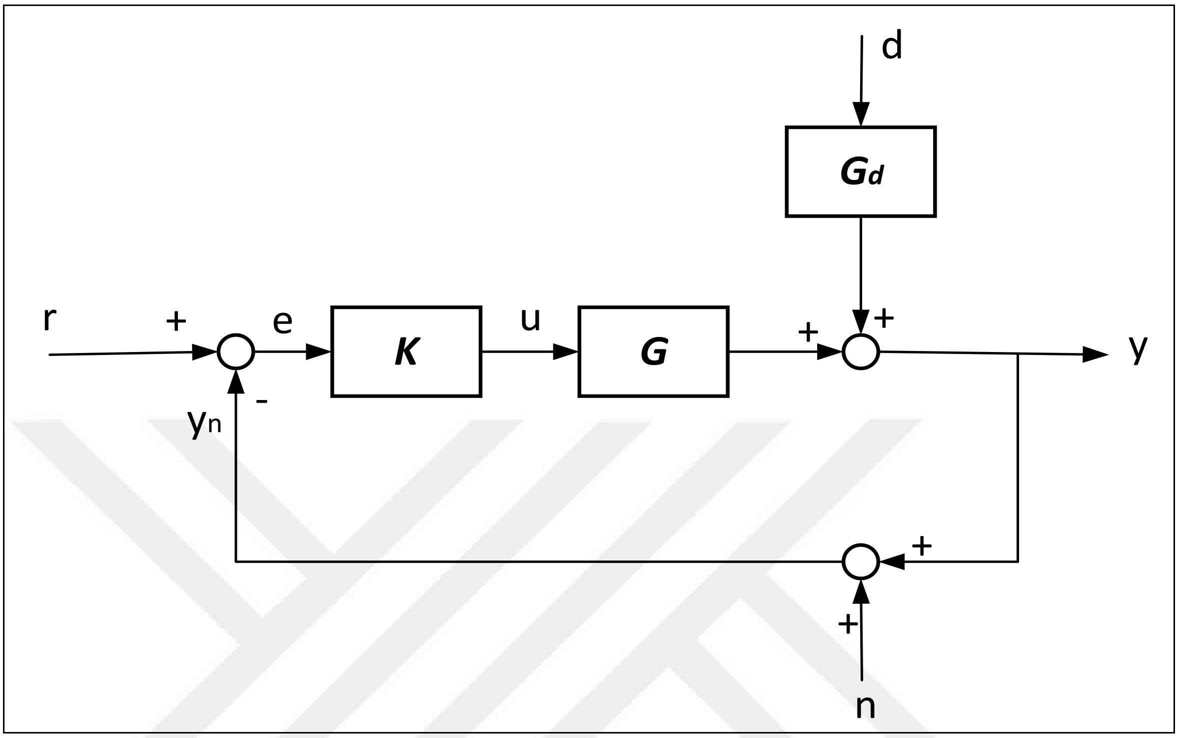

Figure 3.7. Single input single-output control system configuration

Consider the simple one degree-of-freedom configuration in Figure 3.7. In the control system, external disturbances and sensor noises affect the controller performance. Closed-loop control system equation with all effects taken into account,

$$y = \underbrace{(I + G(s)K(s))^{-1}G(s)K(s)}_{T}\, r + \underbrace{(I + G(s)K(s))^{-1}}_{S}\, G_d(s)d - \underbrace{(I + G(s)K(s))^{-1}G(s)K(s)}_{T}\, n \tag{3.1}$$

And terminology,

$L = GK$ Loop Gain

$S = (I + GK)^{-1} = (I + L)^{-1}$ Sensitivity function

$T = (I + GK)^{-1}GK = (I + L)^{-1}L$ is defined as Cosensitivity transfer function.

Lastly, $S + T = I$

To achieve excellent reference tracking performance, you are prompted for the error to be zero e = y−r = 0. Control input could be parameterized by reference input, disturbance and sensitivity function,

$$u = KSr - KSG_d d - KSn \tag{3.2}$$

System output equals $y = \frac{GK}{1+GK} r$ when (n=d=0), for perfect reference tracking Loop gain GK value must be as high as possible.

In order to rejection of external disturbances, Sensitivity and Cosensitivity functions have to be S≈0 and therefore T ≈ 1. If we examine this situation for the situation where r=n=0, we need to examine the equality of $y = \frac{G_d}{1+GK} d$. In order to minimize the output effect of the disturbances, the GK value must again be very large.

For noise rejection performance with r=d=0 system output equals to $y = -\frac{GK}{1+GK} n$. On the other hand, it should be expected to be GK≈0, that is, when the T ≈ 0 therefore S ≈ I, the sensor noise n can be minimized [52]. Table 3.1. summarizes it up.

Table 3.1. The status of loop gain vs loop transfer functions according to the performance requirements of the closed cycle system

Performance Requirement	**Sensitivity Transfer Function, S**	**Cosensitivity Transfer Function, T**	**Loop Gain, L**
Good disturbance rejection	$S \approx 0$	$T \approx I$	$L \approx \infty$
Good command following	$S \approx 0$	$T \approx I$	$L \approx \infty$
Mitigation of measurement noise on output	$S \approx I$	$T \approx 0$	$L \approx 0$

In addition, the loop gain and boundary regions are shown representatively in Figure 3.8.

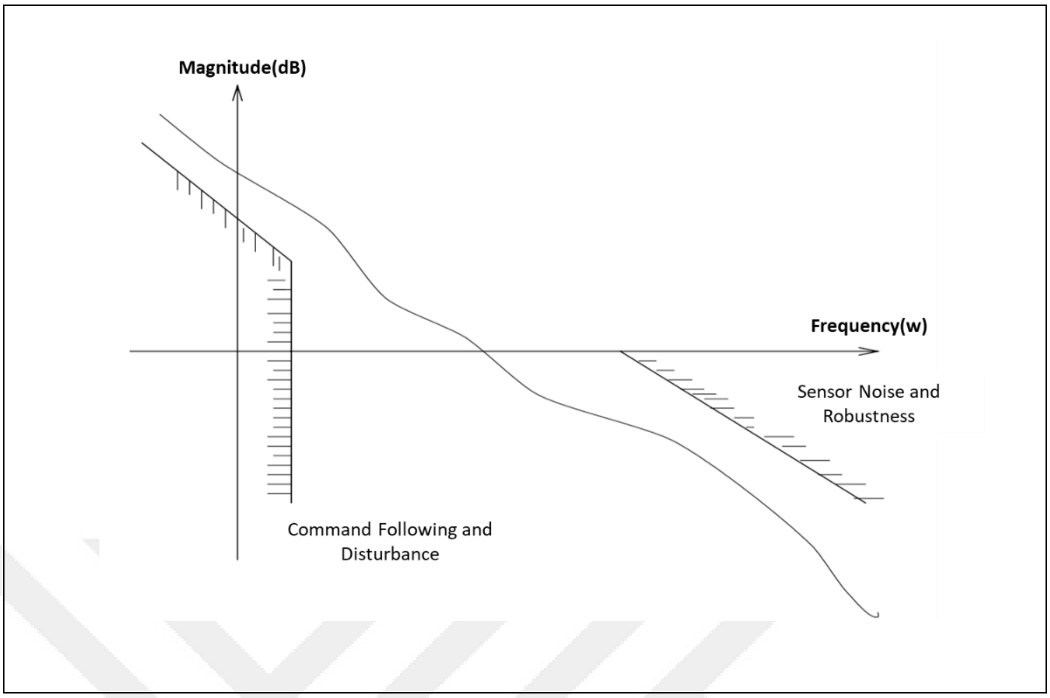

Figure 3.8. BODE Diagram of loop gain G(s)*K(s)

3.4.2. SISO System Frequency Domain Performance

BODE plot gives frequency domain response phase and gain metrics of the system transfer function. Magnitude plot gives gain of the system depending on the frequency, and phase plot gives phase response with varying frequency. Also phase and gain margins can be read using BODE plot.

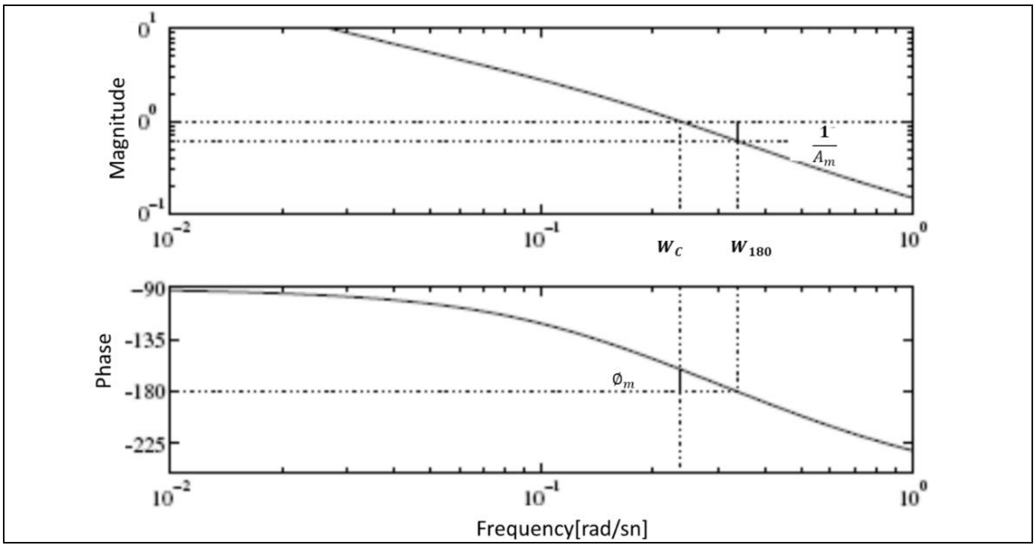

Figure 3.9. Bode plot of L(jω),

The gain margin gives information about the closeness of the loop gain to the point(-1+0i) on the real axis. Phase margin gives information about the distance from the point where loop gain intersects with the unit circle to the point (-1+0i).

An important point on the Nyquist curve is the closest distance of the loop gain to the critical gain point[53]. If we write mathematically

$$d_{\text{crit}} = \min_{\omega}(\text{dist}(L(j\omega), s_{\text{crit}})) = \min_{\omega}|L(j\omega) - s_{\text{crit}}| = \min_{\omega}|1 + L(j\omega)| \qquad (3.3)$$

Therefore

$$d_{\text{crit}} = \min_{\omega}\left|\frac{1}{S(jw)}\right| \qquad (3.4)$$

Since one of the natural goals of the $\mathcal{H}_\infty$controller is to minimize the norm of the Sensitivity function, according to these equations, the decrease in the sensitivity function resulting increase in d_{crit} shows that the system is more robust for perturbation in system parameters.

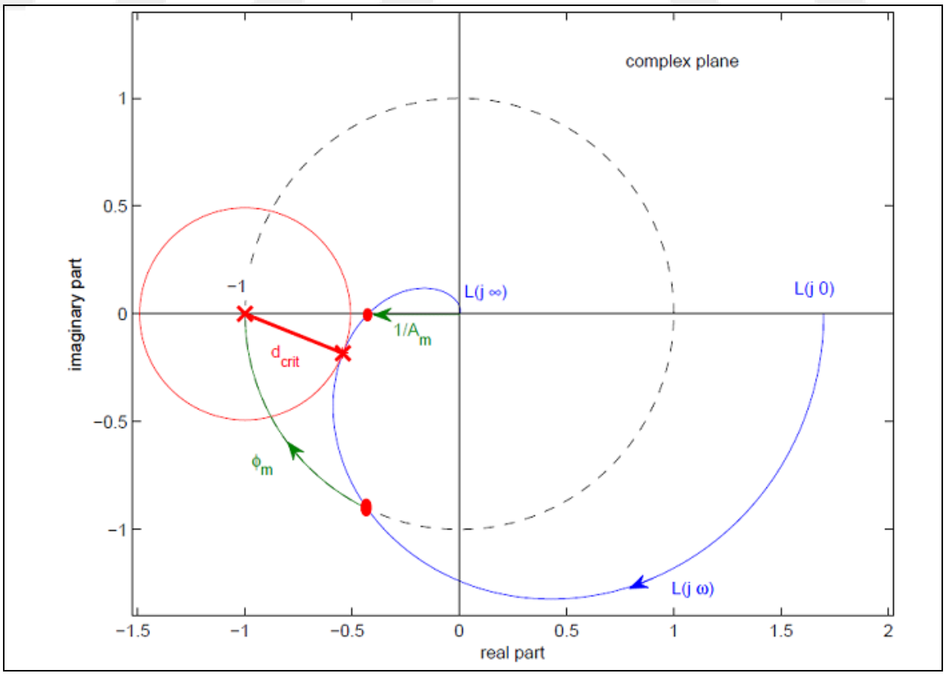

Figure 3.10. Nyquist plot of L(jω), definition of gain(A_m) margin,phase margin($\emptyset_m$) and critical distance (d_{crit}) [53].

3.4.3. MIMO System Loop Shaping

Although the same closed loop equations are valid for MIMO systems, it is necessary to provide similar conditions over singular values for loop shaping. It can be expressed as, $S + T = I$ as the sum of Sensitivity and Cosensitivity functions.

In order to minimize the effect of external disturbances, which are generally dominant in the low frequency region, on the system output, S ≈ 0 therefore T ≈ I should be. Similarly, the highest singular value of the Cosensitivity function should be $\bar{\sigma}(T(j\omega)) \approx 0$ in this region, since sensor noises are dominant in the high frequency region [54].

To minimize the reference tracking error, the value of the cosensitivity function in the low frequency region should be about to the unit matrix. This can be restated as

$$\begin{aligned} \bar{\sigma}(T(j\omega) &\approx I \\ \underline{\sigma}(T(j\omega) &\approx I \end{aligned} \tag{3.5}$$

Keeping the control signal low in the frequency region where distortions and noises are dominant is important for the stability of the system. Equation of the control signal for a closed-loop MIMO system is

$$u = (I + KP)^{-1}Kr - (I + KP)^{-1}K(d + n) \tag{3.6}$$

To keep the control signal low in the frequency region where noise and disturbances are dominant, value of

$$\bar{\sigma}((I + K(j\omega)P(j\omega))^{-1}K(j\omega)) \tag{3.7}$$

have to be near zero. Proposed arguments can be seen graphically in Figure 3.11.

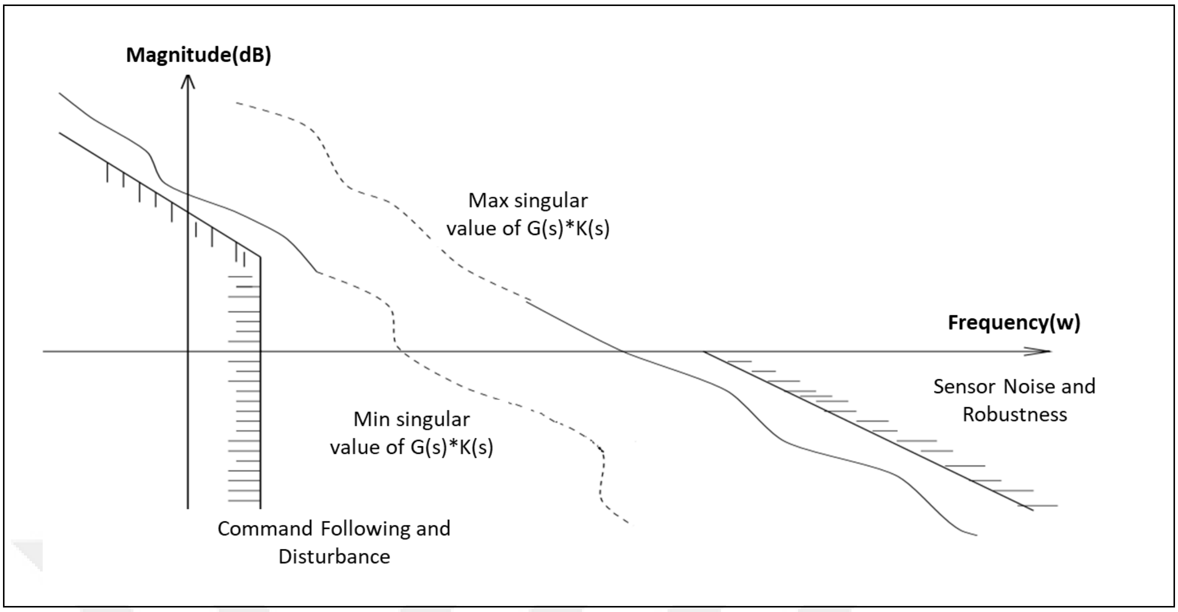

Figure 3.11. Typical Singular value diagram of loop gain G(s)*K(s)

3.5. Finding all stabilizing controllers for closed loop system

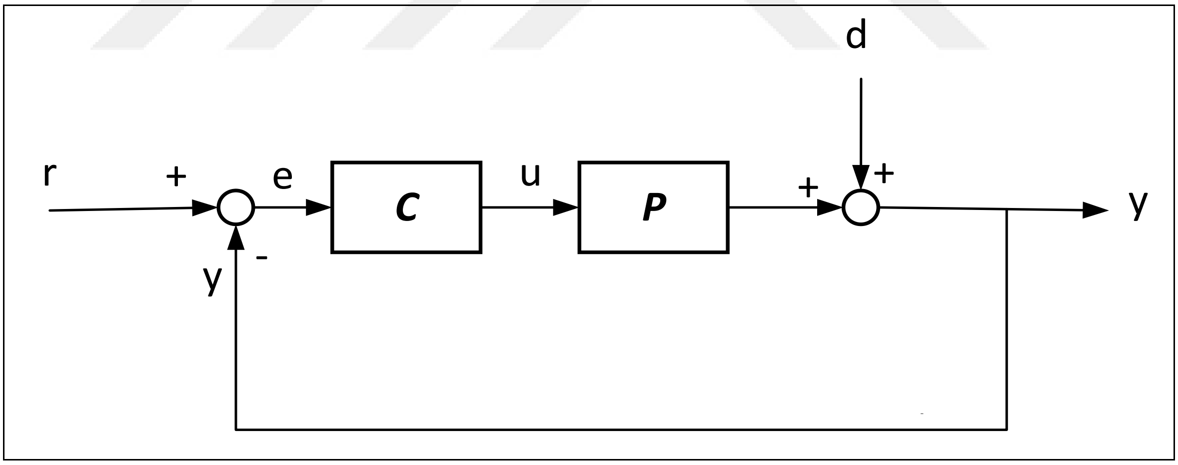

Figure 3.12. Basic block diagram of closed loop control system

All stabilizing controllers for a system can be calculated using Youla Parameterization [54]. For rational transfer function P(s) , left coprime factorization is $\mathrm{P(s)} = \mathrm{N(s)}.\mathrm{M}^{-1}(\mathrm{s})$.

Where N(s) and M(s) are polynomials. Assume there are two other polynomial $\mathrm{X(s)}$ and $\mathrm{Y(s)}$ that satisfy Bezout Identity

$$\mathrm{X(s)}.N(s) + Y(s).\mathrm{M(s)} = I \tag{3.8}$$

Every stabilizing controller $C(s)$ for given G(s) system can be given as

$$C(s) = \frac{\mathrm{X(s)} + Q(s).\mathrm{M(s)}}{Y(s) - Q(s).N(s)} \tag{3.9}$$

Where $Q(s)$ must be a stable polynomial. The next step is to choose these coprime factors and design the free parameter $Q(s)$. If G(s) is stable, we can select N(s)=G(s), M=I, X=0, Y=I. If the transfer function G(s) is unstable, all stable controllers can be found by performing coprime factorization. Coprime factorization method that should be used to calculate all stable controllers for the MIMO case described below.

Coprime Factorization method for SISO and MIMO cases is explained in [55]. If we mention the state space method for coprime factorization, first of all, the matrices forming the G(s) transfer function can be written as, suppose *A, B, C, D* are real matrices with dimensions *(n × n), (n × 1), (1 × n), (1 × 1).*

$$G(s) = \left[\begin{array}{c|c} A & B \\ \hline C & D \end{array}\right] \tag{3.10}$$

Here, our aim will be the state space realization of 4 different transfer functions *M, N, X* and *Y.*

$$G = \frac{N}{M},\ NX + MY = I \tag{3.11}$$

By choosing a real matrix F, (*1 × n*), such that $A + BF$ is stable By taking v= $Fx - u$

$$\begin{aligned} \dot{x} &= (A + BF)x + Bv \\ u &= Fx + v \\ y &= (C + DF)x + Dv \end{aligned} \tag{3.12}$$

M(s) is defined from v to u

$$M(s) = \left[\begin{array}{c|c} A + BF & B \\ \hline B & 1 \end{array}\right] \tag{3.13}$$

and $N(s)$ is from v to y

$$N(s) = \left[\begin{array}{c|c} A+BF & B \\ \hline C+DF & D \end{array}\right] \tag{3.14}$$

Therefore, $u = Mv$, $and\, y = Nv$, The procedure is to choose a real matrix H, $(n \times 1)$, so that $A + HC$ is stable, and then set

$$X(s) = \left[\begin{array}{c|c} A+HC & H \\ \hline F & 0 \end{array}\right] \tag{3.15}$$

$$Y(s) = \left[\begin{array}{c|c} A+HC & -B-HD \\ \hline F & 1 \end{array}\right] \tag{3.16}$$

In summary, the procedure for coprime factorization of proper state space transfer function G(s) is: By setting F and H matrices which stabilizes A+FC and A+HC matrices for transfer functions and using the formulas compute the for functions A,B F,H

3.6. $\mathcal{H}_\infty$ CONTROL METHODS

3.6.1. Sensitivity and Cosensitivity Functions Performance Constarint

As mentioned, if the Loop transfer function is taken as L=P.C and the Sensitivity function is defined from the reference input r to the tracking error e

$$S = \frac{1}{1+L} \tag{3.17}$$

Here, as a performance criterion, if we put the condition that the amplitude of the sine signal given to its input is less than 1, at the output the amplitude of the signal must be less than ϵ, the performance condition is

$$\| S \|_\infty < \epsilon \tag{3.18}$$

Here, if $W_1(s) = 1/\epsilon$ is taken as the weighting function, then as the performance specification is

$$\| W_1 . S \|_{\infty} < 1 \tag{3.19}$$

In $\mathcal{H}_\infty$ loop shaping control, the bode diagram of the sensitivity function is requested to have a certain shape depending on the desired behavior from the system in terms of amplitude gain. If we take ϵ as a frequency dependent transfer function rather than a scalar value, our results will be more realistic. The limit values we want to obtain at each frequency can be given with $W_1(jw)$, provided that S is stable. If we formulate what has been said

$$|S(j\omega)| < |W_1(j\omega)|^{-1}, \forall\omega \tag{3.20}$$

On the other hand, it is similar to the equation written before.

$$\| W_1(jw).S(jw) \|_{\infty} < 1 \tag{3.21}$$

As we said before Complimentary Sensitivity function T, from noise input n, to sistem output y, can be defined as

$$T := 1 - S = \frac{PC}{1 + PC} \tag{3.22}$$

Robust control problem is based on the principle of designing the stable sensitivity and complimentary sensitivity functions in the closed loop control system by shaping the Bode diagrams, by attenuating the outputs against the noise and disturbance effects coming into the system input.

3.6.2. $\mathcal{H}_\infty$ Optimal and Suboptimal Controller

For sub-optimal $\mathcal{H}_\infty$ controller design, the $\mathcal{H}_\infty$ norm of the closed-loop system should be below a certain value determined by γ>0 .And closed loop system should be stable.

$\mathcal{H}_\infty$ norm of closed loop system norm calculated with LFT should satisfy,

$$\| T_{z \to w} \|_{\infty} < \gamma \tag{3.23}$$

Solution method for this sub optimal controller problem is proposed in [56]. By reducing γ iteratively optimal solution can be obtained.

Hinfsyn command in MATLAB is used for calculation of this type controller.

su_ciently accurate _The above result provides a test for each value of _ to

3.6.3. Mixed Sensitvity $\mathcal{H}_\infty$ Controller

In order to shape frequency responses of closed loop system for disturbance rejection, noise reduction, tracking, robustness, and controller effort by shaping S, T, KS transfer functions mixed sensitivity $\mathcal{H}_\infty$ controller is used [54].

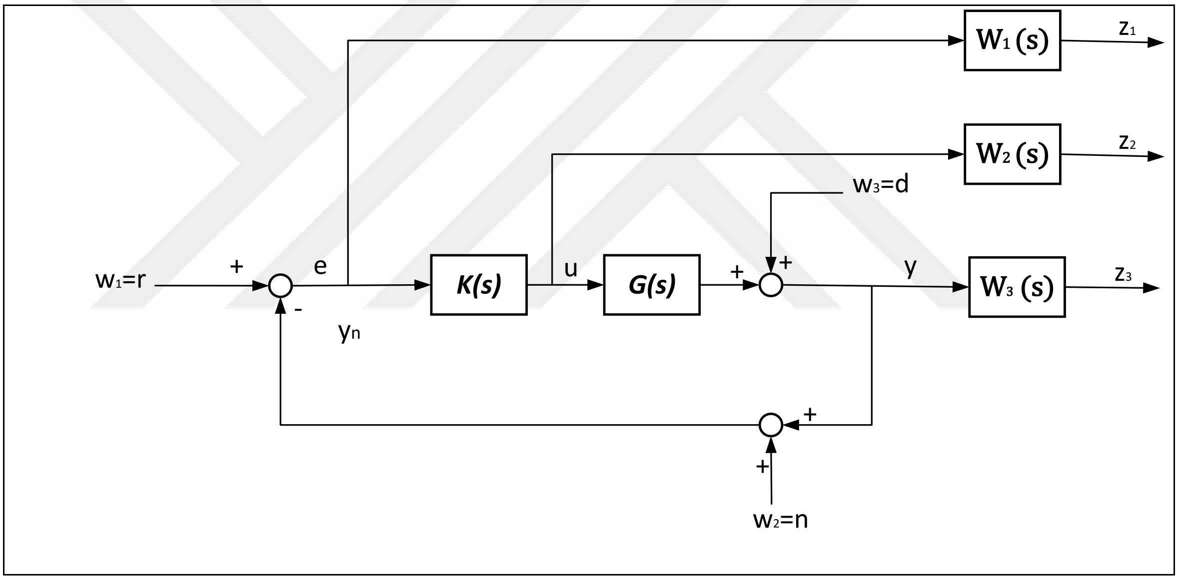

Figure 3.13. Mixed Sensitivity transfer functions $W_1(s), W_2(s), W_3(s)$ in control loop

The transfer function from inputs w to outputs z can be expressed as

$$M(s) = \begin{bmatrix} W_1 S \\ W_2 KS \\ W_3 T \end{bmatrix} \tag{3.24}$$

Where S is the sensitivity, T is cosensitivity and KS is the transfer function from u to y.The weighting functions defined in the frequency domain determine the $\mathcal{H}_\infty$ controller design requirements.

$$\begin{gathered} \| S \|_{\infty} \leq |W_1^{-1}| \\ \| KS \|_{\infty} \leq |W_2^{-1}| \\ \| T \|_{\infty} \leq |W_3^{-1}| \end{gathered} \tag{3.25}$$

And the $\mathcal{H}_{\infty}$ control algorithm calculates the controller that satisfies the following equation.

$$\| M(s) \|_{\infty} = \left\| \begin{matrix} W_1 S \\ W_2 KS \\ W_3 T \end{matrix} \right\|_{\infty} \leq 1 \tag{3.26}$$

If control effort is not want to be restricted just Sensitivity and Cosensitivity functions included in *M(s)*

$$M(s) = \begin{bmatrix} W_1 S \\ W_3 T \end{bmatrix} \tag{3.27}$$

3.6.4. $\mathcal{H}_{\infty}$ Tuning of Fixed-Structure Controllers

Although the $\mathcal{H}_{\infty}$ control method is one of the wide-ranging control methods, it has some limitations. The degree of controllers designed primarily with classical $\mathcal{H}_{\infty}$ controller methods is high. The degree of the controller is determined by adding the degree of weighting functions selected to the degree of the system [53] . Therefore, controllers designed for high-degree systems are also higher degree, which might be a problem for practical applications such as limited computational power and implementation issues [57] .

Algorithms that minimize the $\mathcal{H}_{\infty}$ norm of fixed-structure controllers are often used in practical applications in order to increase the applicability of classical control methods.

In [58] nonsmooth $\mathcal{H}_{\infty}$ optimization technique for fixed structure controllers has been proposed. In order to increase the usability of classical control methods, the algorithm that minimizes the $\mathcal{H}_{\infty}$ norm of fixed-order controllers is frequently used. Controller structrure is defined with

$$K(s) = C_K(sI - A_K)^{-1} B_K + D_K, A_K \in \mathbb{R}^{k \times k} \tag{3.28}$$

where k is the order of structured controller.Standard form of linear time invariant plant described by state-space equations can be given as

$$P(s): \begin{bmatrix} \dot{x} \\ z \\ y \end{bmatrix} = \begin{bmatrix} A & B_1 & B_2 \\ C_1 & D_{11} & D_{12} \\ C_2 & D_{21} & D_{22} \end{bmatrix} \begin{bmatrix} x \\ w \\ u \end{bmatrix} \tag{3.29}$$

$x \in \mathbb{R}^n$ is the state vector, $u \in \mathbb{R}^{m_2}$ is the control inputs, $w \in \mathbb{R}^{m_1}$ is the exogenous inputs, $y \in \mathbb{R}^{p_2}$ vector of measurement inputs, $z \in \mathbb{R}^{p_1}$ performance vector. Algorithm calculates $K(s)$ such that minimizing $\|T_{w\to z}(K)\|_\infty$ subject to $K(s)$ stabilizes the system.

MATLAB Command Hinfstruct extends classical Hinfsyn comand to fixed structure control system synthesis.

Aforomentioned algorithm is suitable for the design of fixed-order MIMO controllers in a centralized and decentralized structure.

4. SYSTEM MODELLING AND EXPERIMENTAL SETUP

4.1. EXPERIMENTAL SETUP

In the laboratory environment, the test environment shown in Figure 4.1 was established for system identification and controller design. The test environment consists of HE-NE Laser source, two FSMs, one PSD, Industrial PC and a real-time PCIe-6320 card. Laser beam is obtained in the visible area (wavelength 632 nm) in the visible area with laser welding. The first of the two FSMs is used to create disturbance effects similar to optical jitter and the second FSM is used to suppress the disturbance effects detected via PSD. PSD, the latest element of the optical pathway, is used to detect the disturbance effects of laser beam. Finally, PCIe-6320 is used to collect/process real-time data.

Figure 4.1. Experimental setup

The optical path refers to the path from the laser beam to PSD via the Disturbance FSM and Control FSM, respectively. After the laser beam exits the source, optical jitter-like disturbances are added to the laser beam using the Disturbance FSM located in the optical path. Disturbance added laser beam is projected from the control FSM, another element of the optical path, and falls onto the PSD. Distortions in the optical path with PSD are obtained as linear displacement in the x and y coordinate plane. In the last step, the controller running in real time on the PCIe-6320 drives the Control FSM with the control signal in the reverse form of distortions in the optical path, and the deviations on the PSD are corrected.

4.2. HE-NE LASER SOURCE

Stabilized HeNe laser, which is shown in Figure 4.2. as the laser source and is given its properties with Table 4.1., was used in the experimental device. The HeNe laser source consists of two parts: the power supply module and the laser head.

Figure 4.2. Stabilized HE-NE laser source

Table 4.1. Specifications of HeNE Laser Source

Wavelength	632.991nm
Stabilized Power	>1.2mW
Beam Diameter	0.7mm
Beam Divergence	1.25mrad

The HeNe laser is a low-power gas laser used in many industrial and scientific applications such as metrology, imaging and optical alignment. The wavelength of the laser used is 632.8 nm in the visible red zone. The most important feature of this laser is that it has stabilized frequency and optical power output.

In this study, a stabilized laser source was selected to avoid external noise from the laser source. In order to stabilize the laser source, the laser source was opened 1 hour before the studies and the laser beam was expected to stabilize.

In this experimental setup, P4S30 product of MRC company, shown in Figure 4.3, was used as FSM. 2-inch mirror is mounted on the FSM with a mirror holder. The technical specifications of the P4S30 are given in Table 4.2.

Figure 4.3. P4S30 FSM

Table 4.2. Technical Specifications of P4S30 FSM

Specification	**P4S30**
Tilting range	4 mrad (± 2mrad) mechanical, 8 mrad optical
Coarse adjustment (manually)	± 4.5°
Piezo stacks	4 Piezo stacks integrated
High resonant frequencies	> 1,200 Hz (with 1" mirror)
High stabilizatör bandwidths	> 400 Hz (with 1" mirror)

A total of 4 Piezo Stacks, two for each axis, were used in the P4S30 product. The high voltage amplifier given in Figure 4.4. is used to drive these piezo stacks in the FSM.

Figure 4.4. High voltage amplifier module

4.3. POSITION SENSITIVE DETECTORS(PSD)

There are two types of sensors: 4-quadrant sensor and PS to detect type/tilt distortions occurring in laser beam. The 4-quadrant sensor consists of 4 standard light-sensitive diodes separated by small gaps. The basic principle of operation is to determine the location of the laser beam on the sensor by looking at the density of each of the laser beams that fall on these 4 photodiode. Another sensor is PSD.

Compared to the 4-quadrant sensor, the PSD provides a continuous measuring field on the sensor. It can also detect even a very small focused laser beam. For this reason, the VIS PSD product of the MRC company, shown in Figure 4.5., was used in the experimental setup. The technical specifications of the product are given in Table 4.3.

(a) (b)

Figure 4.5. VIS PSD (a) Front view of PSD , (b) Back view of PSD

Table 4.3 Opto-electronic properties of PSD

Bandwidth	up to 100 kHz
Sensor area	9.0 x 9.0 mm2
Typical spatial resolution	< 1.5 µm (depending on the beam diameter and profile)
Spectral sensitivity	VIS version: 320 – 1100 nm
Sensitivity / position vs. voltage	approx. 1.2 mV / µm

4.4. DATA ACQUISITION CARD

National Instruments' PCI-Express 6363 card, shown in Figure 4.6.hf , was used to collect data on the system and run control loops. This board is widely used mainly in applications such as data acquisition, control and test automation. The PCI-e 6363 card has 32 analog inputs, 4 analog outputs and 48 digital I/O features with 16-bit resolution and 250kS/s sampling rate. In addition, this card provides the ideal environment for control loops by using the low latency PCI Express bus.

Figure 4.6. NI PCIe 6363 data acquisition card

4.5. EXPERIMENTAL SYSTEM BLOCK DIAGRAM

Figure 4.7. shows the path of the laser light after leaving the He-Ne(Helium-Neon) laser source until it reaches the PSD. After the laser beam leaves the source, it first comes to the disturbance FSM. Disturbance was added to the laser beam using Disturbance FSM in order to model the real disturbance. Distorted laser beam arrives at the Position Sensitive Sensor after reflecting from the Control FSM.

The experimental setup, whose block diagram is given in Figure 4.7. is set up on an optical table. With this mechanism, it is aimed to find the transfer function of the system using the system identification method and to design a controller that minimizes the effects of disturbances.

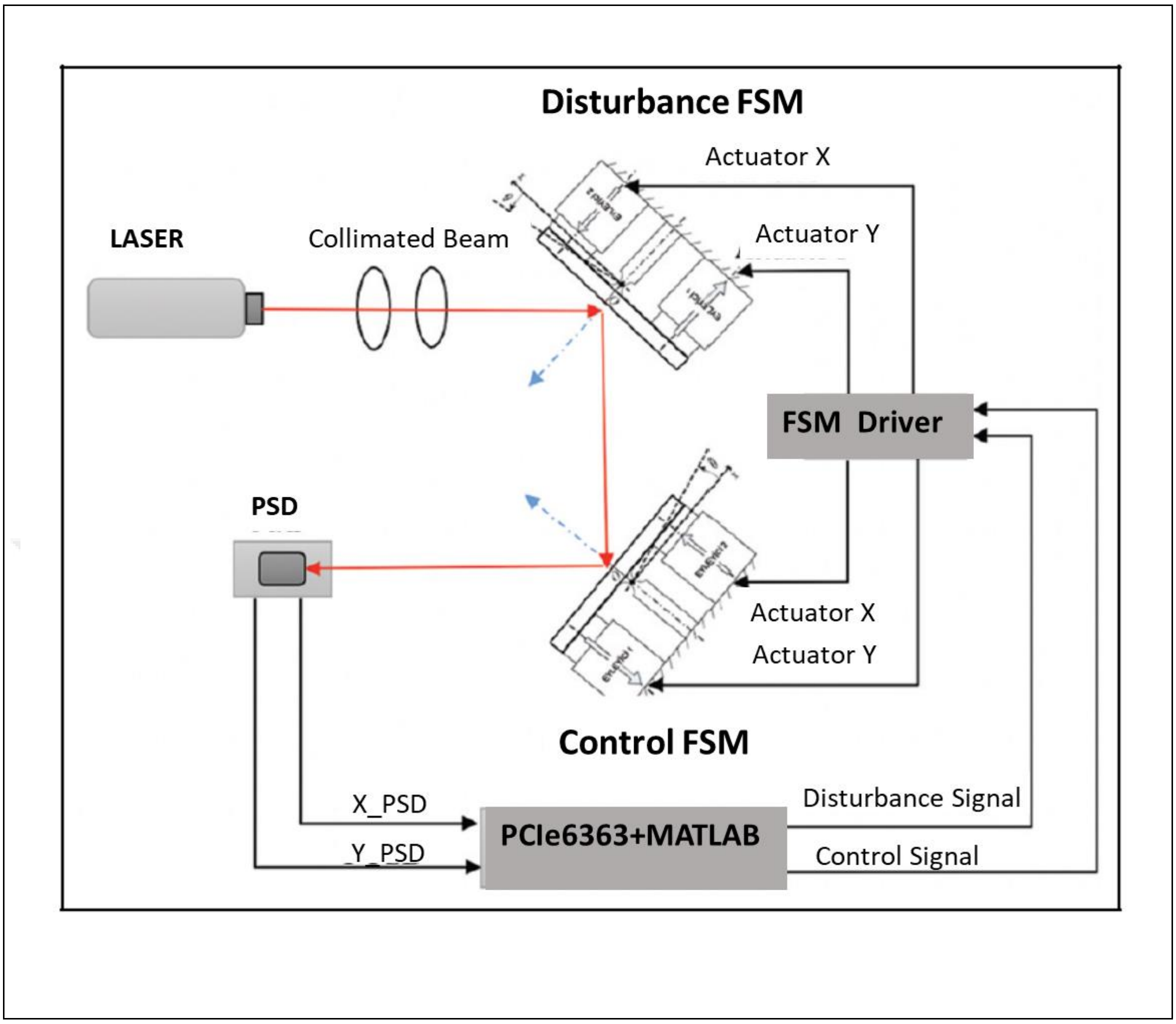

Figure 4.7. Block diagram of experimental setup

National Instruments' PCIe-6363 product was used to control the Disturbance and Control FSMs with analog signals and to read analog position information via PSD.

4.6. MODELLING WITH SYSTEM IDENTIFICATION

In our experimental setup, we are using two FSMs, one is used to create atmospheric turbulence effect, and the other is used to compensate this aberration. First of all the tip tilt deformation in the laser beam is determined by the position sensitive detector. Then, the control unit drives FSM in order to take the shape in the reverse form of distorted wavefront and consequently the reflected wavefront from the mirror would be corrected. In order to analyse a real time system, deriving an accurate model is essential. Since modelling a system via physical laws needs a comprehensive knowledge and effort, mostly system identification methods are employed by researchers because of its practical usage. In system identification methods, only thing to do is to excite the system with suitable input signals and observe the outputs. Using the relationship between, these data the system model can be acquired. The main idea of these techniques is based on minimizing the difference between the derived model and the real system, so that this model represents the system well.

The first and the most important step in the process of deriving the system model is to determine excitation signals. These signals are crucial, in order to attain characteristic behaviour of a system they should be constructed in the system operation frequency band. In the light of this, a rich signal which is constructed by the randomized 50 sinusoidal signals is used to encapsulate all bandwidth provided by the FSM manufacturer and extract the appropriate parameters of the selected model structure. The equation of summation of sinusoidal signals is given as follows

$$\mathrm{w(k)} = \sum_{i=1}^{50} \vartheta_i \cos(2\pi\omega_i \mathrm{t}) \tag{4.1}$$

This is called rich sinus signal. Where ϑ_{i} and ω_{i} are denoted as amplitude, frequency. Their values are gernerated randomly. It used random sinus signals to cover all bandwidth given by the FSM manufacturer for the inference of the appropriate parameters of the selected model structure. ω_i is gaussian random variable with a mean value of 50 Hz and a variance 20 Hz. ϑ_i is also gaussian random variable with a mean value of 0 Volt and variance 2 Volts.

In this thesis it is aimed to minimize tip-tilt deformation modes of the atmospheric turbulence. The frequency bandwidth of a system for minimizing only these atmospheric turbulence modes is different from the case in which other high order modes are taken into account. In order to deal with tip-tilt mode correction, the optical system should have a bandwidth greater than the following frequency,

$$f_{tilt} = 0.386\, D^{-1/6} \lambda^{-1}\, sec(\beta)^{1/2} \{\int dh C_N^2\,(h) V(h)^2\}^{1/2} \tag{4.2}$$

which is called Tyler frequency. Where C_N^2 represents the strength of atmospheric turbulence and other parameters D, V, λ, β, h represent lens diameter, wind speed, wavelength, zenite angle and altitude, respectively. in Figure 4.8 , the frequency values for different scenarios are demonstrated.

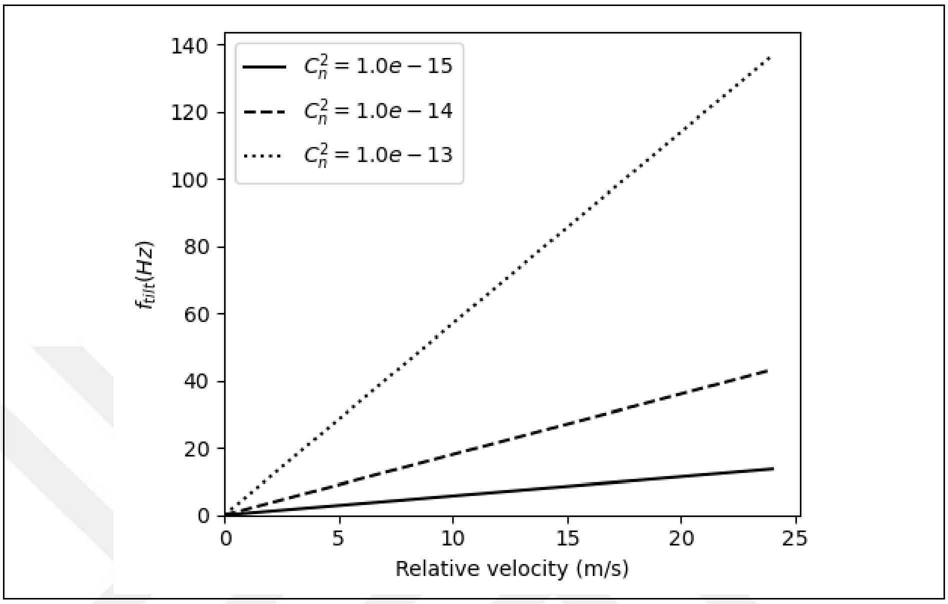

Figure 4.8. The characteristic frequency values of the system for tip/tilt correction, valid under different atmospheric conditions. λ = 808 nm, L = 500 m, D = 0.3 m.

Based on this, another rich sinus signal with the sum of 50 sinusoids with a frequency random variable of 250 Hz and a standard deviation of 25 Hz, whose bandwidth is 2.5-3 times that of the atmospheric scintillation signal, is used since the laser light will be exposed to atmospheric scintillation. The signals sent to the inputs are shown in Figure 4.9. The x-axis and y-axis output signals from the PSD sensor are shown in Figure 4.10.

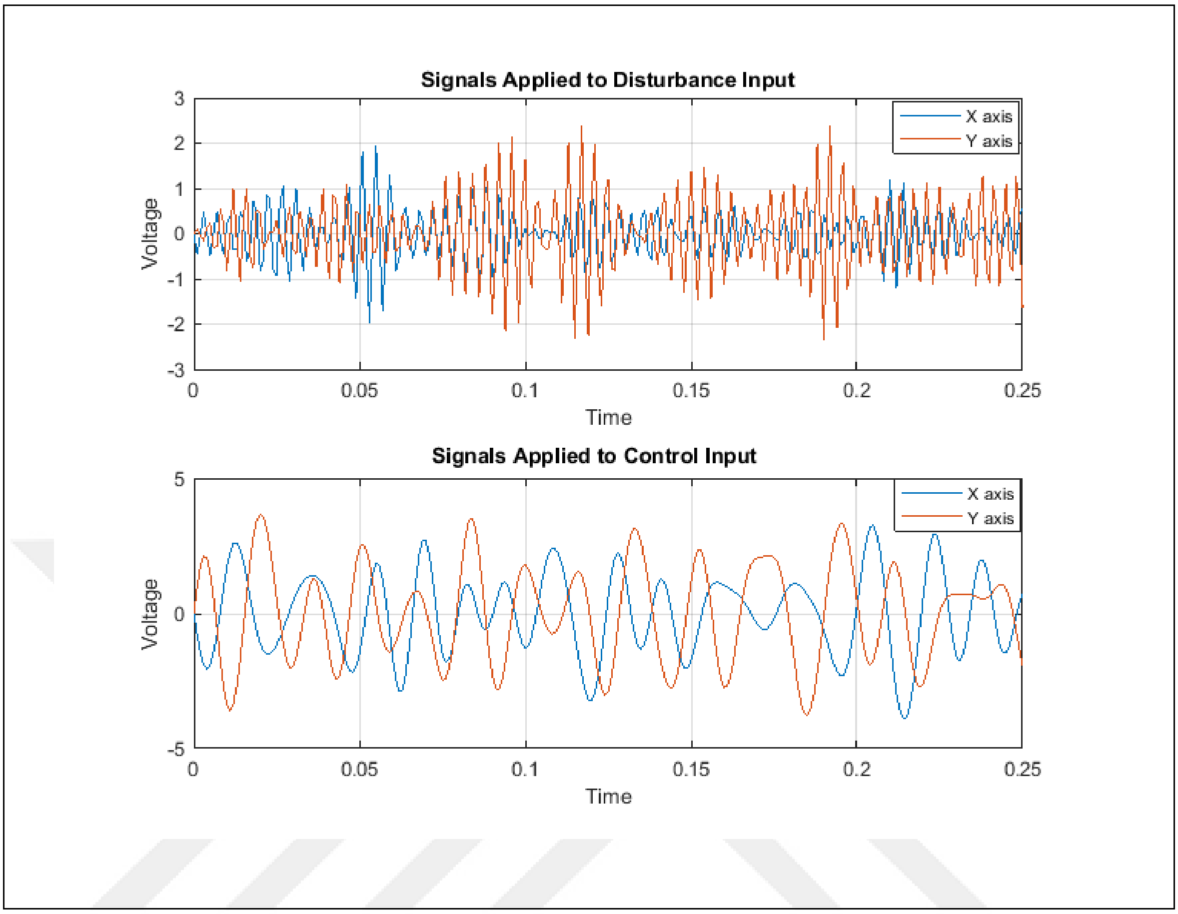

Figure 4.9. Disturbance and control signals applied to experimental setup

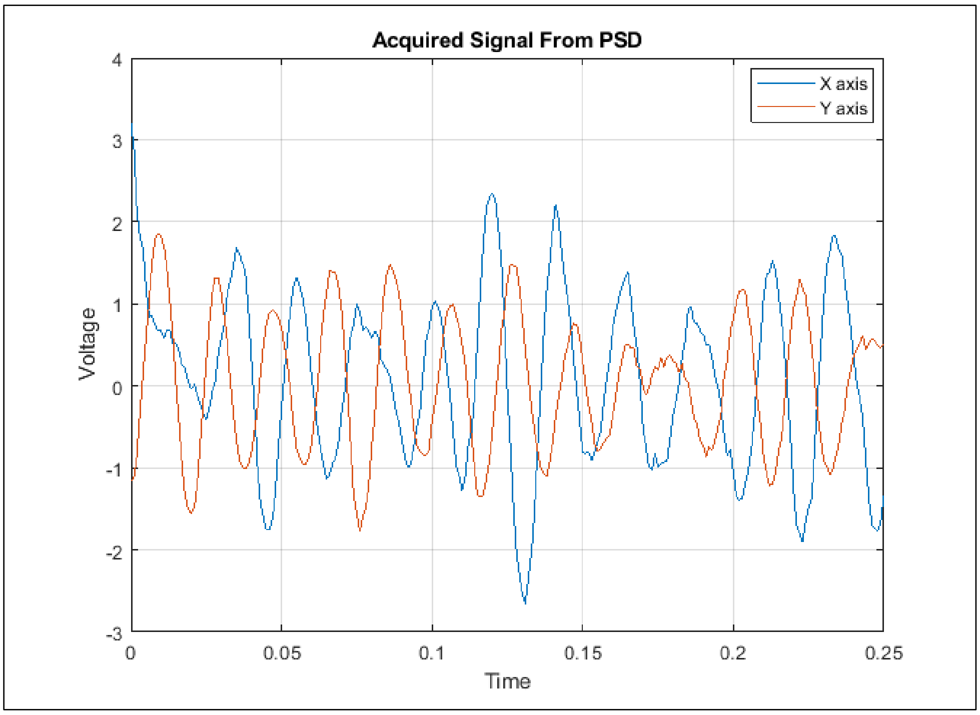

Figure 4.10. Acquired signals from PSD

Table 4.4. Comparison of transfer functions and real system output for 2 different types of rich sinus signals applied to the system

Model Type / Accuracy%	Phase-1		Phase-2	
	X axis(%)	Y axis(%)	X axis(%)	Y axis(%)
3^{rd} Order System	94	95	91	92
4^{th} Order System	94	96.5	91	94.5
5^{th} Order System	92	94	91	89
6^{th} Order System	93	96.5	88.3	95.4
Frequency Domain Identified System	86.5	93	81.5	91

Another important stage in deriving a model between then input and the output signals is the selection of model structure. The choice of the model structure depends on the dynamics and the noise characteristics of the system. The system identification techniques are divided into the parametric and the non-parametric ones. After selecting the model structure in parametric methods, the parameters of the selected model are estimated. In non-parametric methods, the model structure is not selected in the first stage, the model is estimated through inputs and outputs. In this study, parametric model is preferred for time domain system identification.

Also frequency domain identificaton has been applied to compare the results and seeing the identified model and frequency respose of system comparatively. In addition, the frequency response was obtained by examining the response of the system in the entire frequency band, and frequency domain identification was made using the MATLAB System Identification Toolbox®, rich sinus signal given in equation (4.1) is used for 4 inputs. In terms of covering the frequency band completely, the frequency $\omega_i$random variable is selected with standard deviation of 190 Hz with an average value of 200 Hz. The amplitude random variable ϑ_i is 0 Volt average value and standard deviation of 2 Volts.

The data obtained from the predicted models and the data obtained from the real system were compared using the mean squared error function given in equation (4.3). Table 4.4 shows the result and performances of the different structures.

$$fit = \frac{\| x - xref \|^2}{Ns} \tag{4.3}$$

Where Ns is the number of samples and ‖ indicates the 2-norm of a vector. x is test data $xref$ is reference data.

The signals used in system identification were not used for verification. Thus, the best model fitted to real system could be decided. Two different test data were collected on the real system using rich mixed sine signals to compare the compatibility of the predicted models with the real system. The signals used in these tests are rich mixed sinus signals with random frequency variable mean 45 Hz and standard deviation 25 Hz and random frequency variable mean 55 Hz and standard deviation 15 Hz.

As a result of these observations, 4th order state space model provides a very similar response to the real time system, identified state space equation is

$$A = \begin{bmatrix} -484.0525 & -73.8082 & 835.4421 & 216.6447 \\ -99.9231 & -400.7242 & 276.5892 & 468.4347 \\ 755.4889 & 291.8578 & -4403.17 & -579.0370 \\ 322.0545 & 365.2778 & -604.9344 & 1849.60 \end{bmatrix}$$

$$B = [B_w \quad B_u] = \begin{bmatrix} -6.1629 & -4.0354 & 6.5146 & -7.2197 \\ -0.6446 & -1.9007 & -1.2667 & 1.2754 \\ 150.5311 & -12.0074 & -167.7240 & 43.3618 \\ -8.9272 & 53.3089 & -8.3555 & 75.7887 \end{bmatrix} \tag{4.4}$$

$$C_z = C_y = \begin{bmatrix} 13.4451 & -0.4461 & -3.0048 & 0.5602 \\ -1.7193 & 13.4935 & -1.5173 & -2.0011 \end{bmatrix}$$

$$D_z = D_y = \begin{bmatrix} 0 & 0 & 0 & 0 \\ 0 & 0 & 0 & 0 \end{bmatrix}$$

The disturbance model is also included in the identified system model. B_w column denotes disturbance inputs B_u column denotes the system inputs.

Time response comparison response to rich sinus signal to 4^{th} order model and real system is given in Figure 4.11.

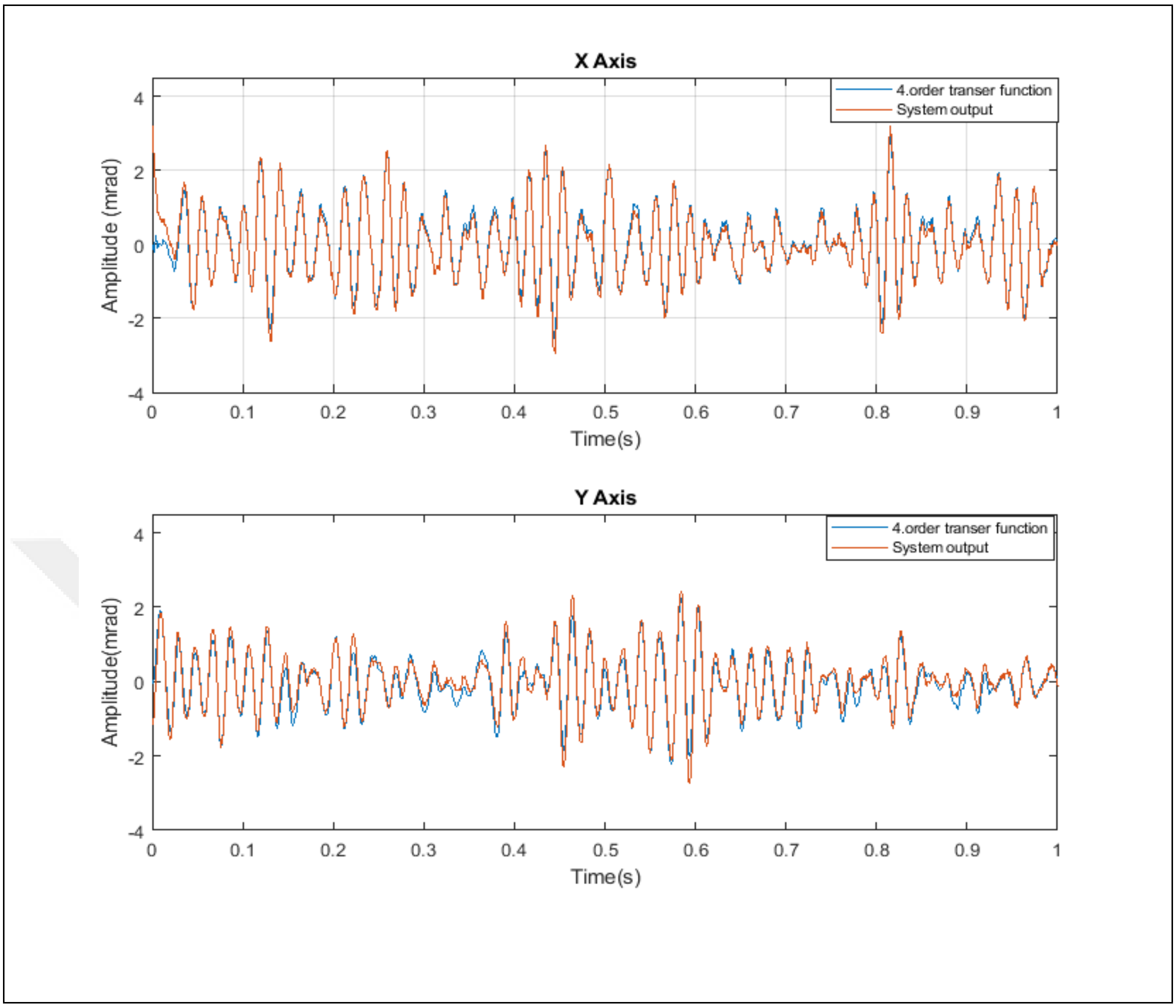

Figure 4.11. Time response comparison of predicted 4th order model and real time system

Singular value comparison plot of 4th order model, system response and frequency domain identified model could be seen in Figure 4.12.

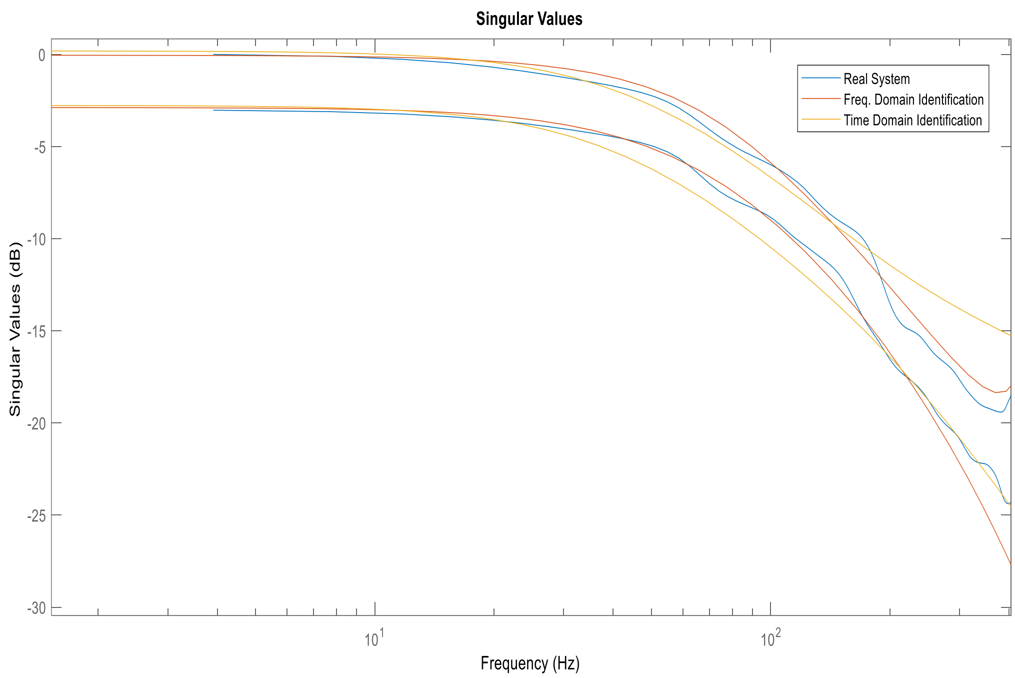

Figure 4.12. Frequency response of best fitted 4th order system and frequency domain identified system

4.7. DISCUSSION OF THE RESULTS

Time domain and frequency domain modeling have been applied to model the experimental system. By using the subspace state-space estimation method, the identification was made by choosing the system transfer function degrees 3,4,5,6. In addition, with the help of the data received to cover the entire operating frequency range of the system, frequency domain system identification was performed and the all identified transfer functions were compared. Although it is seen that all model degrees used in time domain modeling gives high accuracy, it seems that 4th order model gives identification results with a little more accuracy.

In modelling study of FSM [46], 4 state variable results 4th order system, which performs gray-box subspace system identificaton method. In the frequency domain responses given in Figure 4.12, it is seen that the frequency response of the system closely follows the response of the transfer functions identified with different methodolgies. Also hysteresis nonlinearities is another tricky problem in linear identification of FSM systems.

5. FINE TRACKING CONTROLLER DESIGN FOR JITTER REJECTION

5.1. INTRODUCTION

Focusing the laser beam on a prescribed target requires special control approaches due to disturbance effects (atmospheric turbulence, platform vibrations, etc.) that may occur in such applications. These disturbance effects cause the wavefront aberrations and yield beam jitter that is directly related with fluctuations of the laser beam propagation, therefore degradation of performance is inevitable.

Since it is important to keep the received power ratio high against disturbance effects such as platform vibration and atmospheric scintillation for laser beam tracking, fine tracking is of great importance.

Within the scope of this thesis, atmospheric scintillation data modeled by Latmosim® as disturbance signal was used. Flickering of laser light away 1500m under moderate turbulence conditions ($C_N^2 = 10^{-15}$) was calculated and deviations in x and y coordinates on the target was calculated and used as a disturbance signal. Same calculated disturbance signal was applied for evaluation of all designed controllers.

Structured $\boldsymbol{\mathcal{H}}_\infty$ controller has been designed for suppression of disturbance. In order to compare effectiveness of the controller, MIMO loop shaping and the adaptive feedback control based on Youla-parameterization has been designed and applied to same system.

Simulation and experimentation phases was applied in design. In both phases, sample rate is taken as 500 Hz, zero-order hold discreteization method and fixed step solver was used in simulations performed with MATLAB Simulink®.

5.2. PROBLEM FORMULATION

Consider a continuous time LTI MIMO system

$$\begin{aligned}\dot{x} &= Ax + B_u u + B_w w \\ z &= C_z x + D_{zu} u + D_{zw} w \\ y &= C_y x + D_{yu} u + D_{yw} w\end{aligned} \tag{5.1}$$

where $A \in \mathbb{R}^{n\times n}, B = [B_w \;\; B_u] \in \mathbb{R}^{n\times m}, C = \begin{bmatrix} C_z \\ C_y \end{bmatrix} \in \mathbb{R}^{p\times n}, D = \begin{bmatrix} D_{zw} & D_{zu} \\ D_{yw} & D_{yu} \end{bmatrix} \in \mathbb{R}^{p\times m}$ are the system matrices, $x \in \mathbb{R}^n; w, u, y$ and z are the state vector, exogenous input, control input, measured output and performance output respectively. Assume that (A, B_u) is controllable and $D_{yw} = 0$.

The PID controller K(s) has the form

$$\begin{aligned} K(s) &\triangleq K_p + K_i \frac{1}{s} + K_d \frac{s}{T_f s + 1} \\ &= \frac{\left(K_p T_f + K_d\right)s^2 + \left(K_p + K_i T_f\right)s + K_i}{T_f s^2 + s} \end{aligned} \tag{5.2}$$

where K_p, K_i and K_d are P (proportional), I (integration) and D (derivation) gains, respectively, and T_f is the first-order derivative filter time constant to avoid from derivative kick. In brief, it is aimed to find a PID type control law u $=K(s)$y for the system given in equation (5.2) such that the infinity norm of the transfer function between performance output and exogenous disturbance input ($P_{CL}(s)$) should be smaller than a positive scalar value γ, $\|P_{CL}(s)\|_\infty < \gamma$.

5.3. STRUCTURED $\mathcal{H}_\infty$ CONTROLLER DESIGN AND APPLICATION TO SYSTEM

In order to increase the applicability of standard control methods, fixed order $\mathcal{H}_\infty$ control has recently been the most frequently resorted form of $\mathcal{H}_\infty$ control design. However, the fixed order controller design problem is nonconvex, and there is no method that can solve the problem to global optimality. In order to overcome this issue, there exist many different methods. In this section, we use hinfstruct, which is a function under MATLAB Robust Control Toolbox®, in order to design PID type mixed sensitivity $\mathcal{H}_\infty$ controller. Best synthesized controller can be obtained by adding additional optimizations to the synthesis.

5 additional optimizations has been started together with randomstart, parameter for the synthesis. It has been tested that increasing the randomstart parameter more provides no additional benefits for design.

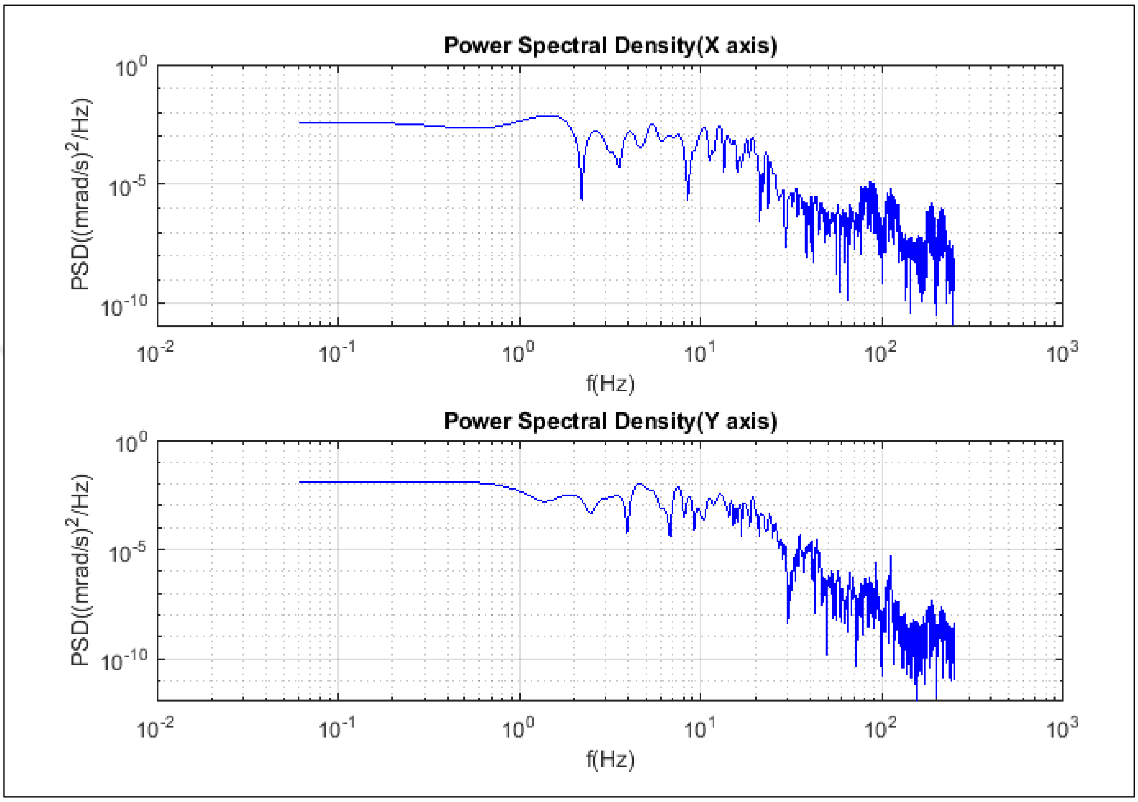

Figure 5.1. Power spectral density of atmospheric turbulence in tip-tilt mode.

In this work, the aim was to enhance the effectiveness of the structured $\mathcal{H}_\infty$ controller being aware of disturbance characteristics. As shown in Figure 5.1, scintillation signal has dominant frequency characteristics between 0 and 40 Hz. In the controller design stage, encapsulating this frequency band is desired. In this context, weight functions, that are called sensitivity and complimentary sensitivity, are chosen as lowpass and highpass filters as follows.

$$\mathcal{S}(s) = \frac{0.5s + 502.7}{s + 0.5027} \quad \mathcal{T}(s) = \frac{40s + 100.5}{s + 1.005 \times 10^5} \tag{5.3}$$

Sensitivity weight transfer function has been selected for disturbance minimization and cosensitivitity weight transfer function has been selected for minimization of PSD sensor noise characteristics

Parameters of PID type controllers are given in Table 5.1 . In the literature, it is common that tip-tilt axis is controlled individually. Therefore, a decentralized PID controller is also designed.

Table 5.1 PID controller parameters

Controller type	K_p	K_i	K_d
MIMO PID controller	$\begin{bmatrix} 76.7 & 395.2 \\ 56.9 & 252.4 \end{bmatrix}$	$\begin{bmatrix} 781.3 & 106.2 \\ 15.9 & 1188.9 \end{bmatrix}$	$\begin{bmatrix} -42.2 & -227.8 \\ -32.1 & -143.4 \end{bmatrix}$
Decentralized PID controller	$\begin{bmatrix} 3.89 & 0 \\ 0 & 3.99 \end{bmatrix}$	$\begin{bmatrix} 1.09 \times 10^3 & 0 \\ 0 & 1.08 \times 10^3 \end{bmatrix}$	$\begin{bmatrix} -6.38 & 0 \\ 0 & 0.027 \end{bmatrix}$

Model simulation results of the structured type $\mathcal{H}_\infty$controller are as follows. Refer to Figure 5.2. - 5.5.

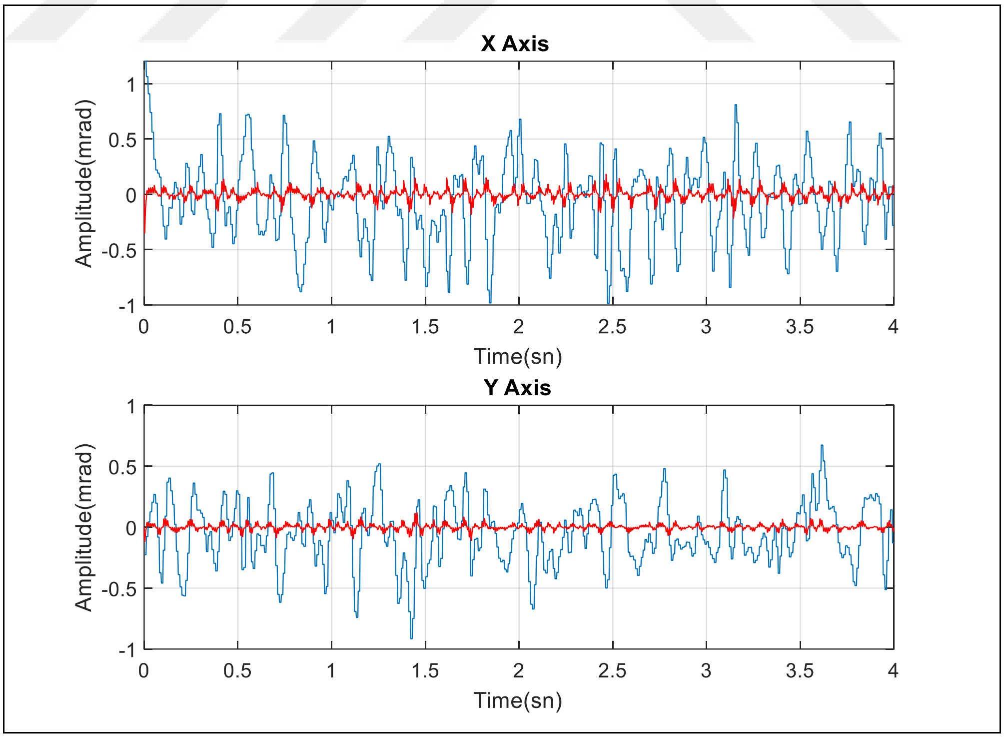

Figure 5.2. Simulation result of the open loop system (blue) and the closed loop system with the decentralized PID. Controller (red)

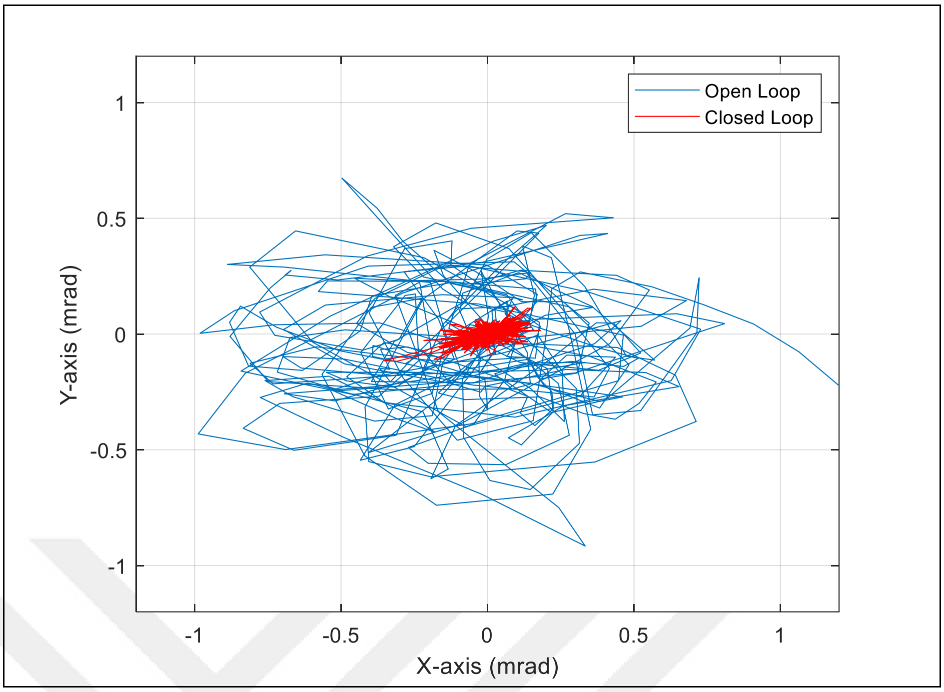

Figure 5.3. Simulation result of the distortion on the X-Y plane (blue) and stabilization with the decentralized PID controller (red)

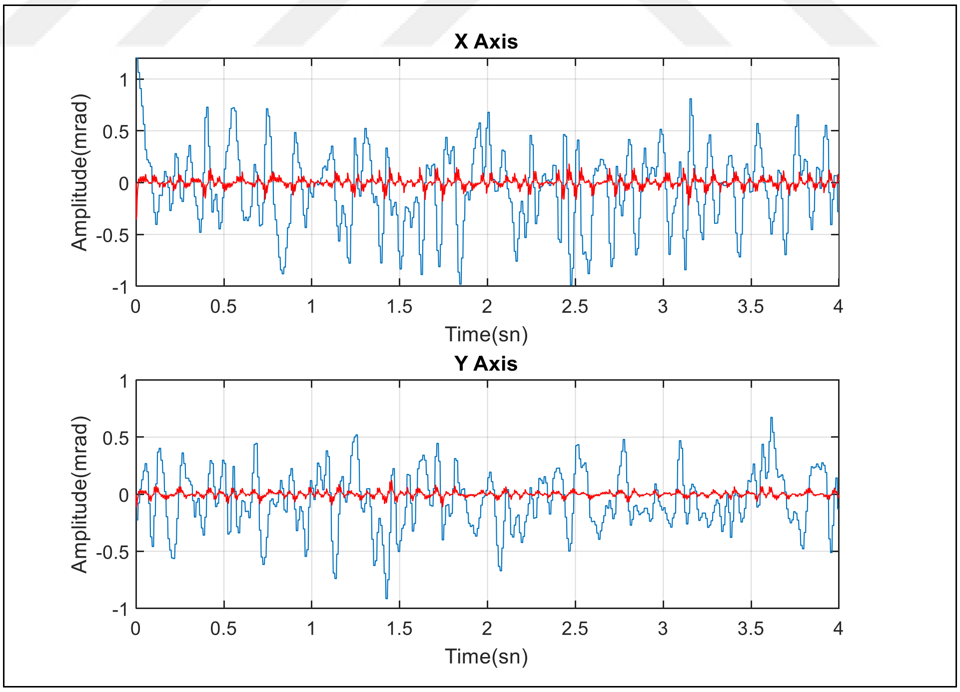

Figure 5.4. Simulation result of the open loop system (blue) and the closed loop system with the MIMO PID. controller (red)

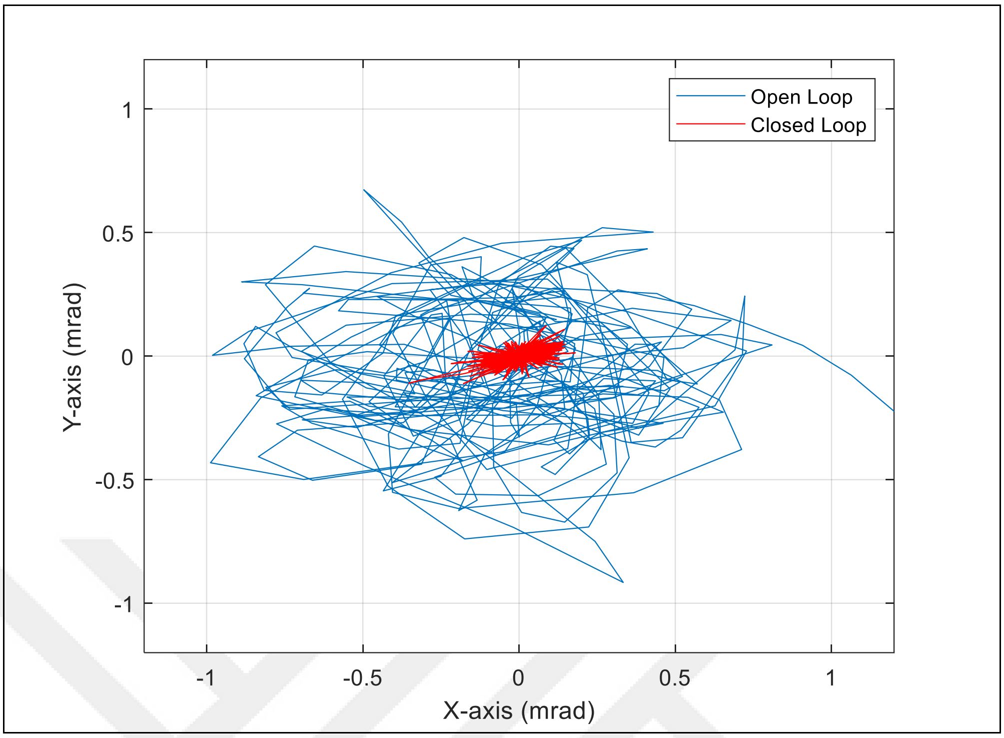

Figure 5.5. Simulation result of the distortion on the X-Y plane (blue) and stabilization with the MIMO PID controller (red)

Also for comparison of performance, MIMO loop shaping based controller has been designed and applied to identified system model in equation (4.4). The transfer function of MIMO loop shaping-based controller which is designed over frequency response of atmospheric turbulence, is as follows. Second order Bessel type lowpass filter with cutoff frequency f_c=477 Hz is selected. Resulting decentralized type controller is given in the following.

$$K(s) = \begin{bmatrix} \dfrac{900000}{s^2 + 5196s + 900000} & 0 \\ 0 & \dfrac{900000}{s^2 + 5196s + 900000} \end{bmatrix} \tag{5.4}$$

Loop gain has been designed as $L(j\omega) = k * G(j\omega)K(j\omega)$, where k value has been selected according to maximum disturbance rejection performance. For disturbance rejection in the low frequency range, frequency gain constant k has been increased until proper gain margin in Nyquist plot has been reached. Controller and system transfer functions are shown in Figure 5.6.

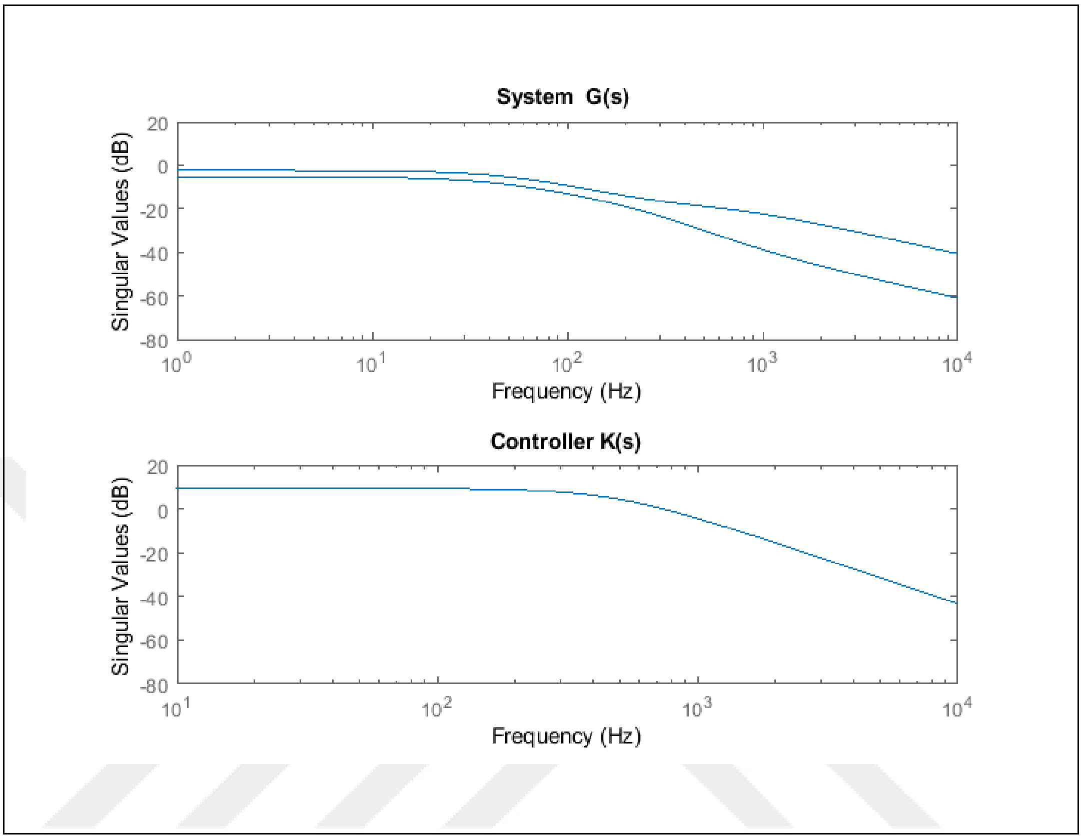

Figure 5.6. System and controller transfer functions

Resulting plot of loop gain function singular values is shown in Figure 5.7.

As mentioned in Section 3.4.3, it is important to keep loop gain high, $G(j\omega)K(j\omega) \gg 1$ for disturbance rejection in the low frequency region. Nevertheless, in high frequency region it is important to keep loop gain low, $G(j\omega)K(j\omega) \ll 1$ for good noise rejection.

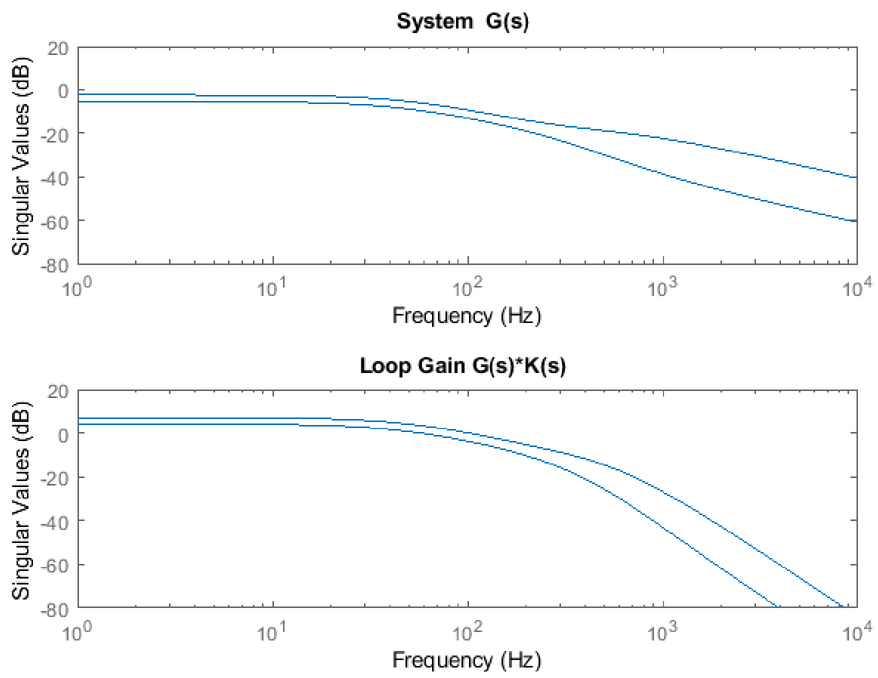

Figure 5.7. System and loop gain transfer functions

Resulting Sensitivity and Cosensitivity functions of the designed controller is shown in Figure 5.8. Also Nyquist plot for designed controller is shown in Figure 5.9.

From Nyquist plot one can see that increasing k value of the designed controller reduces the gain margin of the designed controller. Consequently, simulation results have been given as follows. Refer to Figure 5.10. - 5.11. in text.

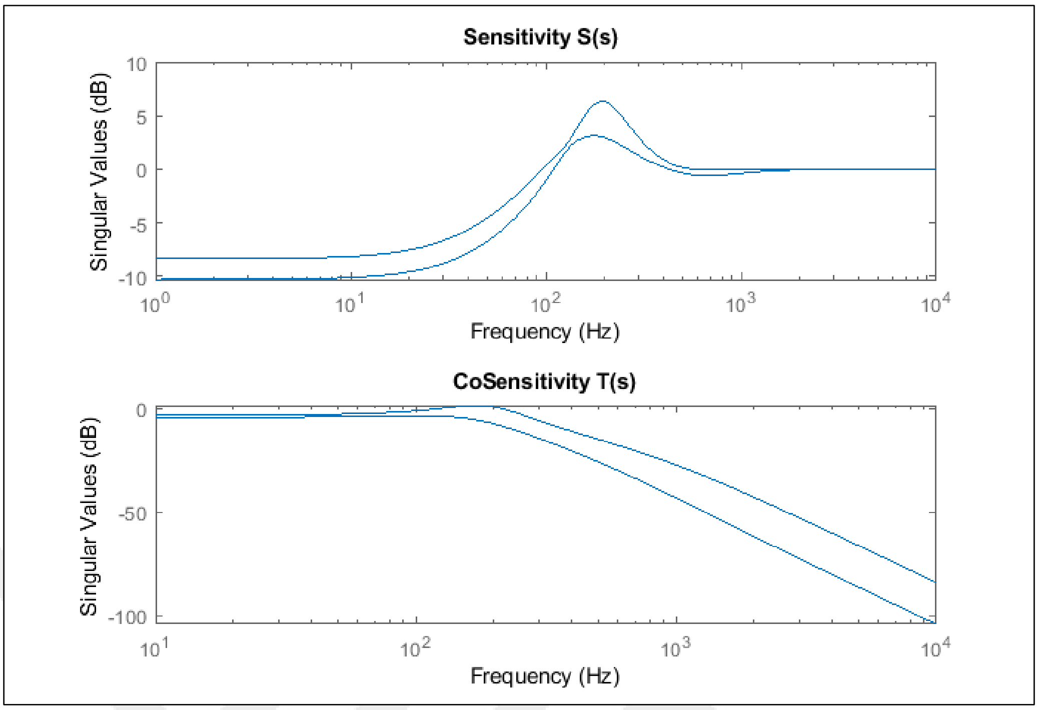

Figure 5.8. Sensitivity and Cosensitivity functions

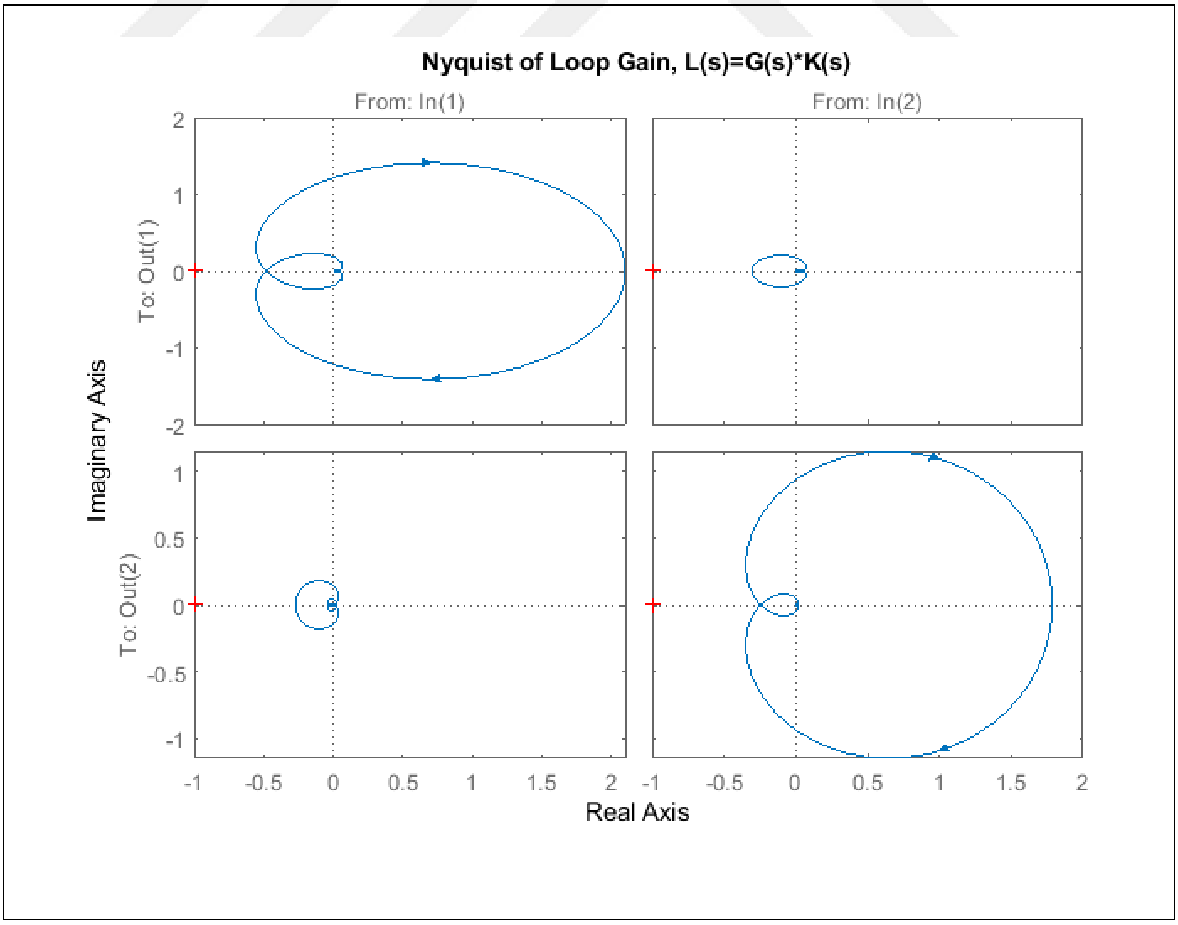

Figure 5.9. Nyquist Plot of the designed loop gain

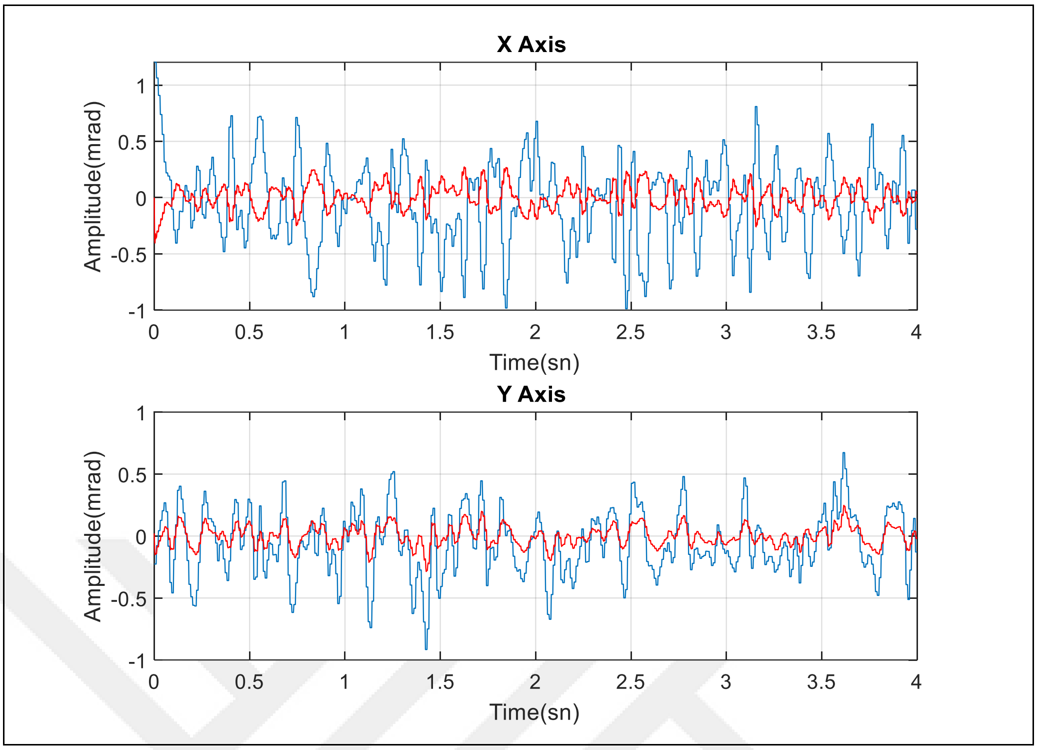

Figure 5.10. Simulation result of the open loop system (blue) and the closed loop system with the controller designed by loop shaping (red).

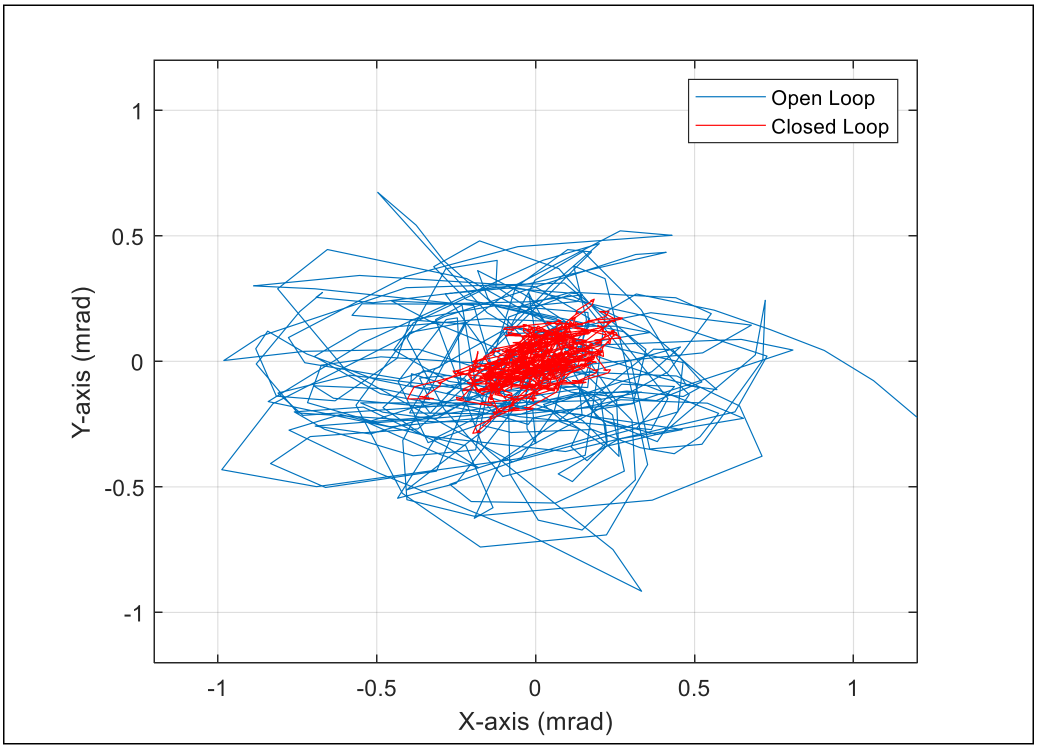

Figure 5.11. Simulation result of the distortion on the X-Y plane (blue) and stabilization with loop shaping based designed controller (red)

In order to compare effectiveness of this study, an adaptive feedback controller by the help of Q-Parameterization has been designed. Adaptive feedback jitter control method using Q-parametrization to minimize vibration-induced jitter is given in [30]. The result of this work is utilized in order to reject unwanted disturbance effects. This work is mainly based on setting Q parameter of the Youla parametrization to an adaptive finite impulse response and this parameter is updated by a recursive the least mean squares (LMS) algorithm. The main structure of this algorithm is given in Figure 5.12. Stable coprime factorization of G(z) is$\mathrm{G}(\mathrm{z}) = \mathrm{N}(\mathrm{z}).\mathrm{M}^{-1}(\mathrm{z})$, where N(z) and M(z) are its coprime factorizations. C(z) refers to transfer function of the controller as follows

$$C(z) = \frac{\mathrm{X}(\mathrm{z}) + Q(z).\mathrm{M}(\mathrm{z})}{Y(z) - Q(z).N(z)} \tag{5.5}$$

Where $Q(z)$ is a stable polynomial, every stabilizing controller $C(z)$ for given G(z) can be given as

$$\mathrm{X}(\mathrm{z}).\mathrm{N}(\mathrm{z}) + \mathrm{Y}(z)\mathrm{M}(\mathrm{z}) = \mathrm{I} \tag{5.6}$$

where X and Y are coprime factorizations of the nominal controller. There are various ways to derive coprime factors, among them one such pattern is as follows.

$$\mathrm{X} = \mathrm{K},\ \ \mathrm{Y} = \mathrm{I},\ \ \mathrm{M} = \mathrm{S} = (\mathrm{I} + \mathrm{G}.\mathrm{K})^{-1},\ \ \mathrm{N} = \mathrm{G}.\mathrm{S} = \mathrm{G}.\mathrm{M} \tag{5.7}$$

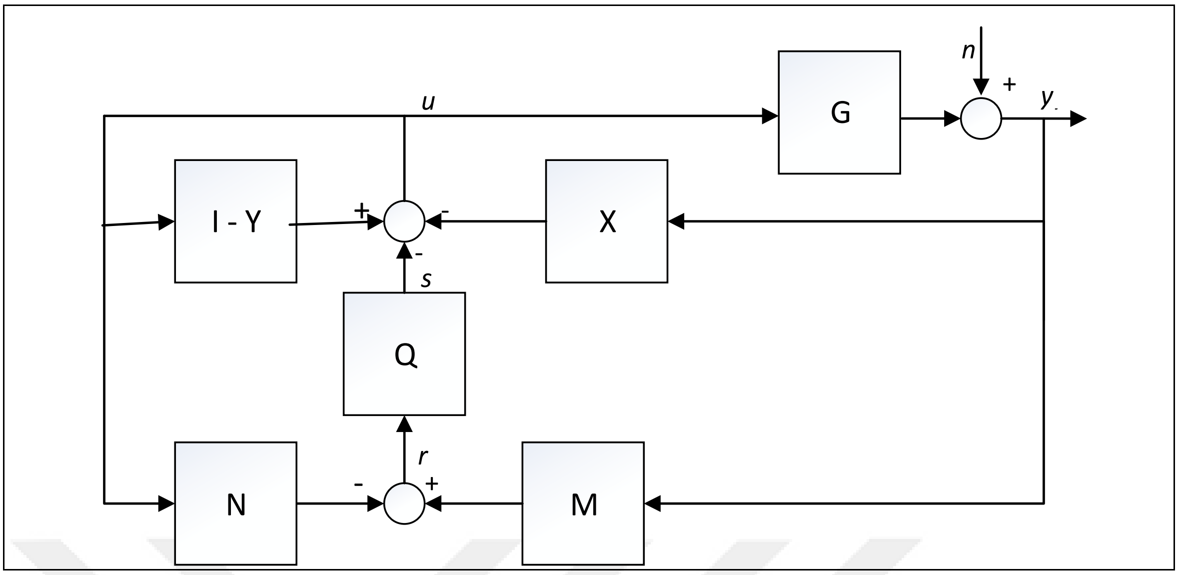

Figure 5.12. Youla-parameterization control structure

Since FIR Filters are stable due to their structure, it is an acceptable approach to select Q(z) polynomial as FIR adaptive filter. An FIR filter that we defined for Q parameter in the z domain is

$$Q(z) = w_0 + w_1.z^{-1} + w_2.z^{-2} + \cdots + w_{L-1}.z^{-L+1} \tag{5.8}$$

Cost function $\boldsymbol{J}$ have to be defined for adaptation of parameters, as instant value of the squared error value of the jitter signal.

$$J(n) = \frac{1}{2}\, y^2(n) \tag{5.9}$$

Each Q element is selected as FIR filter and LMS adaptation for FIR filters equation is derived from the block diagram given in Figure 5.12. for the jitter output y. The global minimum of the cost function with respect to the filter coefficients is achieved via adjusting the coefficients in the negative gradient direction of this function. The degrees of all FIR filters are selected as 25.

$$w\,(n+1) = \propto w\,(n) + \mu(-\nabla_w) \tag{5.10}$$

Each Q element is selected as FIR filter and LMS Adaptation for FIR Filters Equation is derived from the block diagram in Figure 5.12, the output y as a function of Q can be written:

$$y = (I + G.S.Q.)r \tag{5.11}$$

Gradient vector is calculated from

$$\nabla_w = \frac{\partial J}{\partial w} = y\frac{\partial y}{\partial w} \tag{5.12}$$

Partial derivative of jitter signal respect to filter coefficients can be written

$$\frac{\partial y}{\partial wi} = -[G(z)S(z)]rz^{-i} \tag{5.13}$$

Now let us define the filtered signal $x = -G(z)S(z)r$. Update equations for the FIR filter could be written as

$$w(n+1) = \propto w(n) + \ \mu\, y(n)\,[x(n), x(n-1),,, x(n-L+1)]^T \tag{5.14}$$

For MIMO system every vector in block diagram have two dimensions pan and tilt axis components, also x signal have

$$r = \begin{bmatrix} r_p \\ r_t \end{bmatrix}, \quad y = \begin{bmatrix} y_p \\ y_t \end{bmatrix}, \quad x = \begin{bmatrix} x_p \\ x_t \end{bmatrix} \tag{5.15}$$

Q polynomial for MIMO system have to be in matrix form for minimizing the jitter

$$Q = \begin{bmatrix} Q_{11}(z) & Q_{12}(z) \\ Q_{21}(z) & Q_{22}(z) \end{bmatrix} \tag{5.16}$$

For adaptation of $Q_{11}(z)$ and $Q_{12}(z)$ polynomial coefficients y_p and x_p is used. In equation (5.16. And for adaptation of $Q_{22}(z)$ and $Q_{21}(z)$ y_t and x_t . Consequently, the performance of this controller is given in Figure 5.13, 5.14.

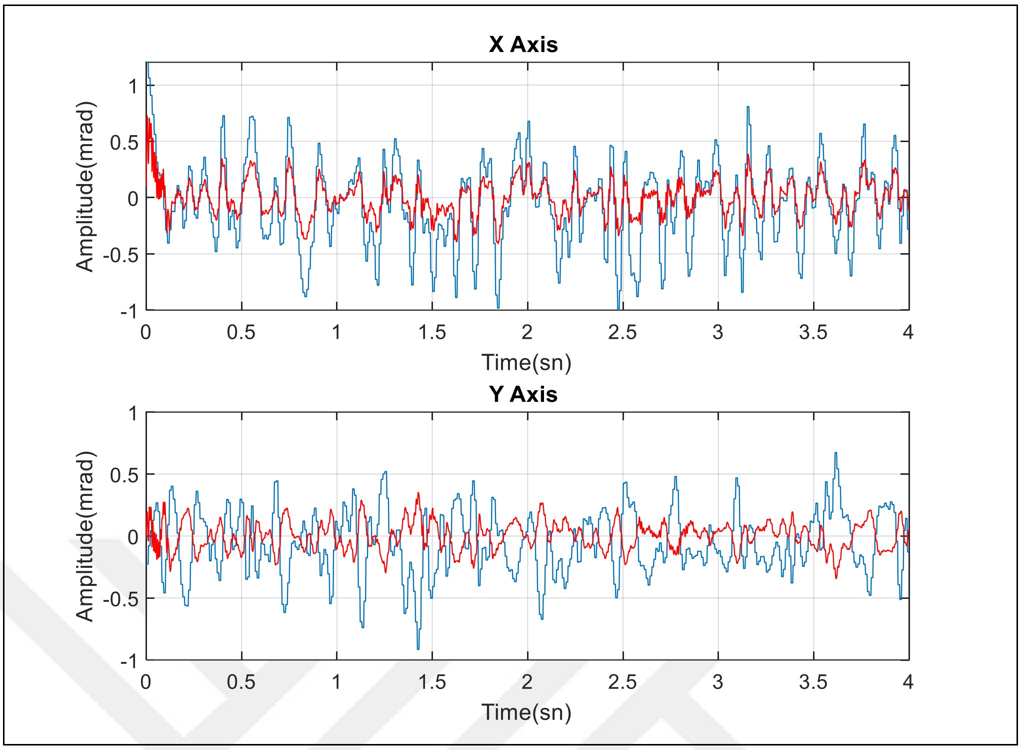

Figure 5.13. Simulation result of the open loop system (blue) and the closed loop system with the adaptive feedback controller (red)

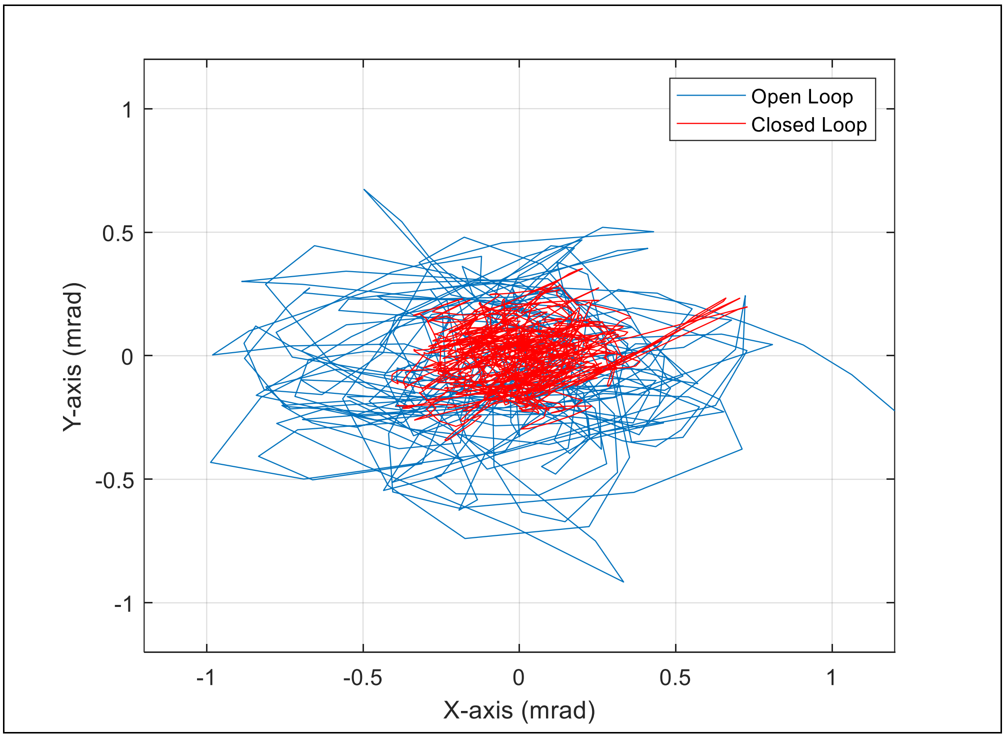

Figure 5.14. Simulation result of the distortion on the X-Y plane (blue) and stabilization with the adaptive feedback controller (red)

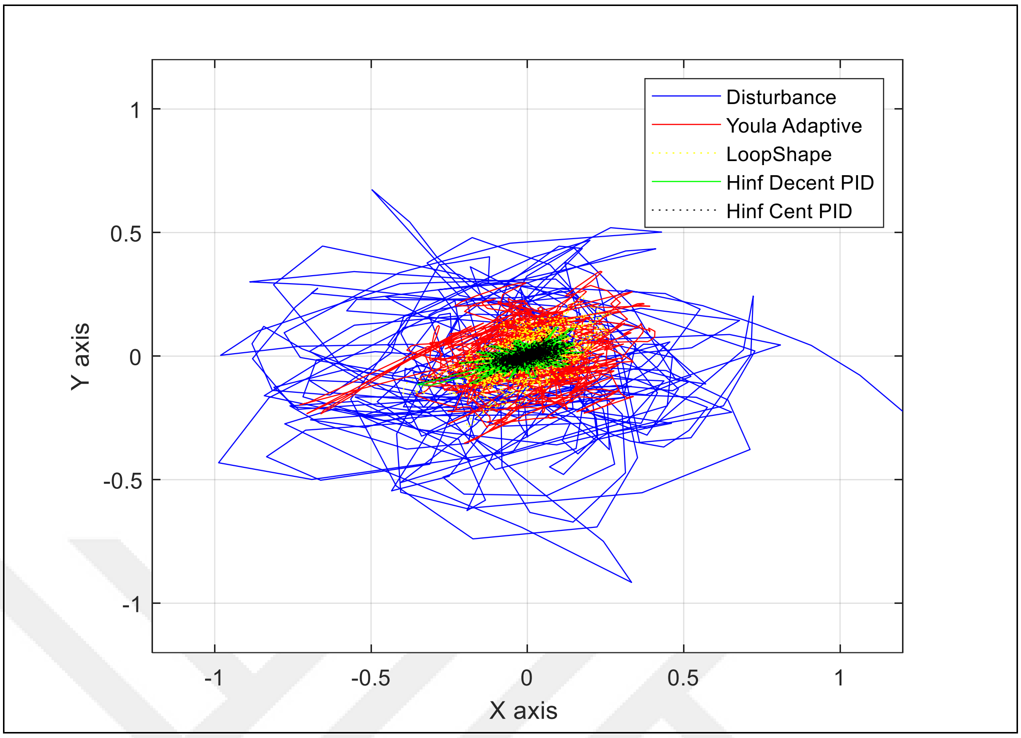

Figure 5.15. Simulation result of the distortion on the X-Y plane and stabilization with the controllers.

Simulation phase results are given in Figure 5.1 - 5.5 and Figure 5.10 - Figure 5.15, and experimental phase results are demonstrated in Figures 5.16 - 5.24 One can observe nearly the same improvements that are accomplished in both phases. Each PID controller provide nearly the same improvement, only a small difference exists between them; as it is usual in literature, one can control tip/tilt mirror separately at the expense of a small loss in enhancement.

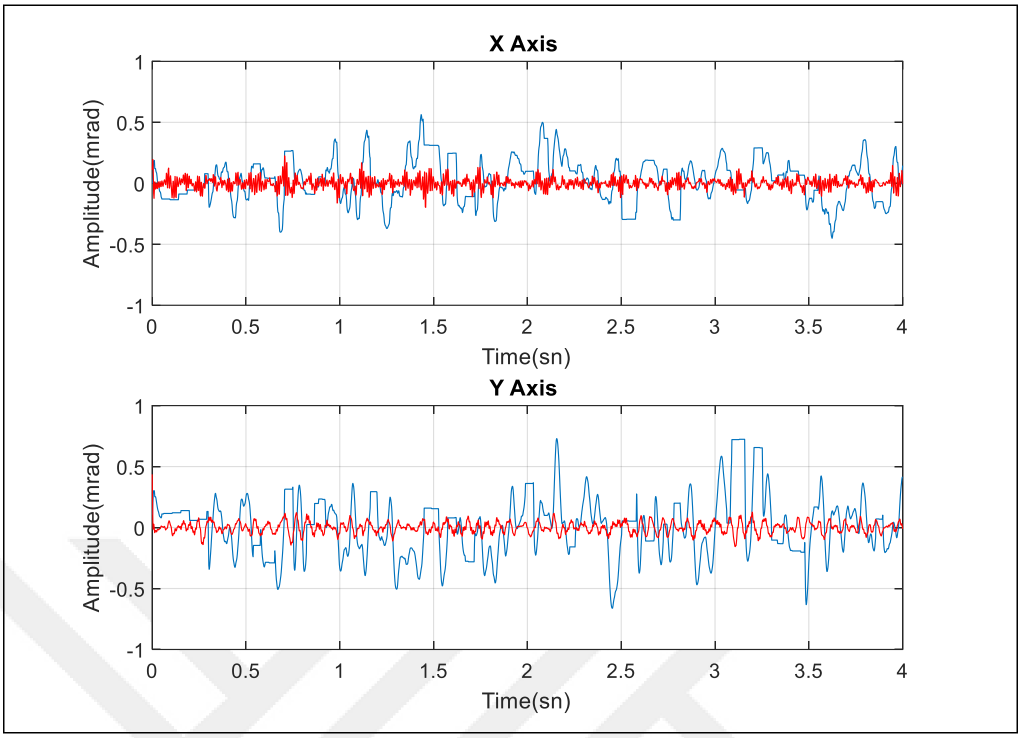

Figure 5.16. Experimental result of the open loop system (blue) and closed loop system with the decentralized PID controller (red)

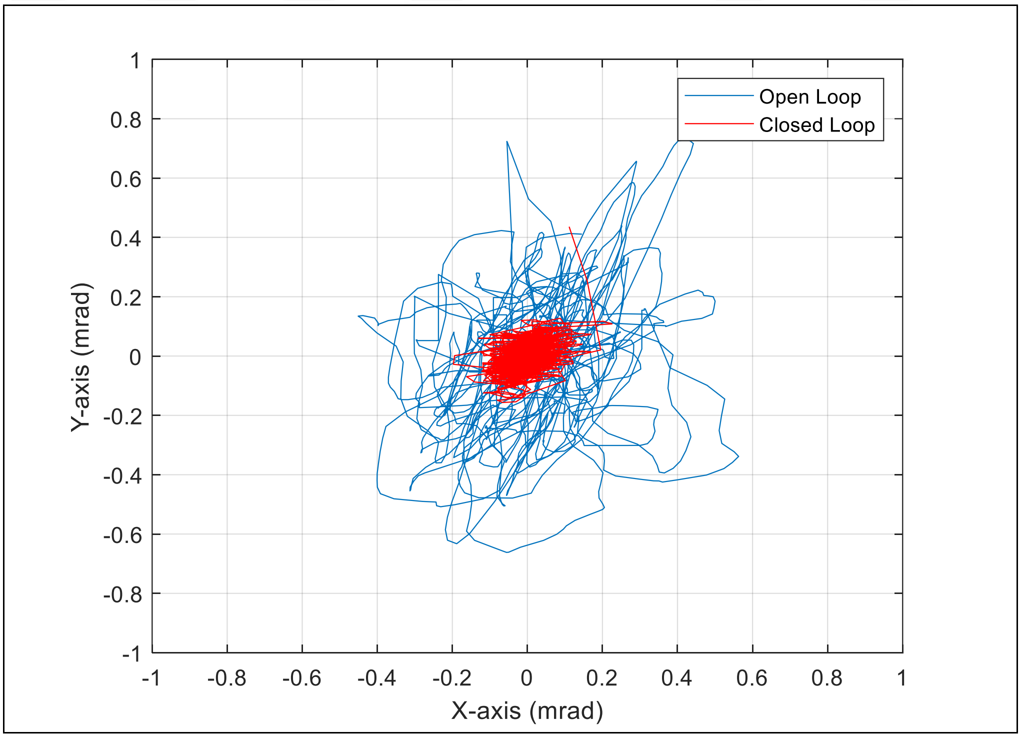

Figure 5.17. Experimental result of the distortion on the X-Y plane (blue) and stabilization with the decentralized controller (red)

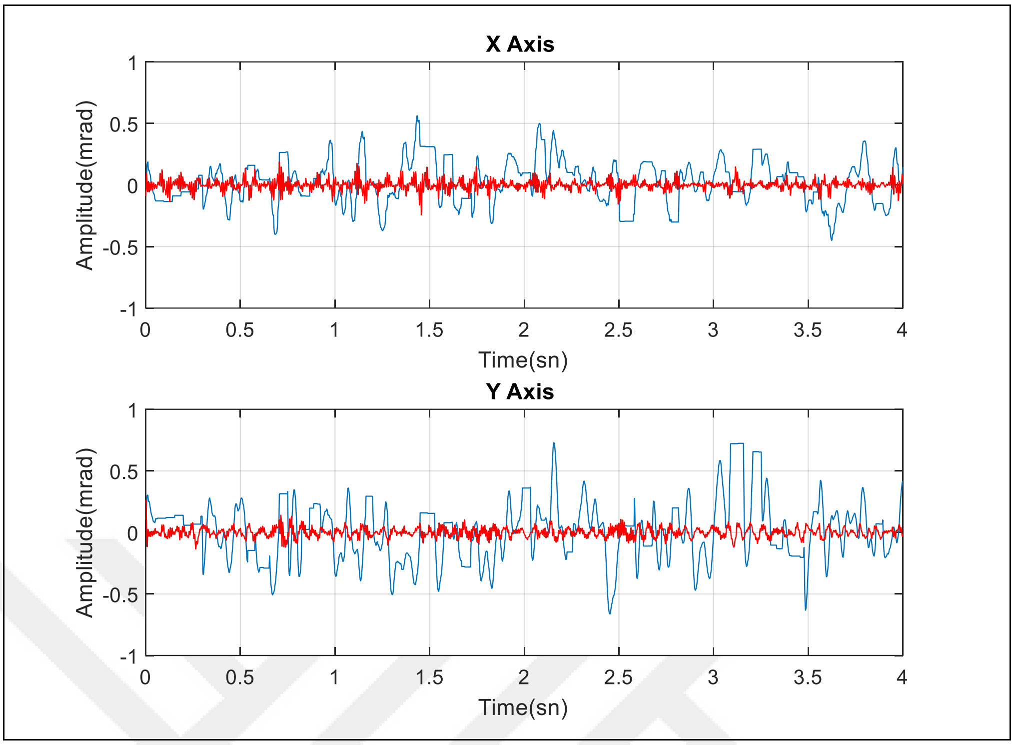

Figure 5.18. Experimental result of the open loop system (blue) and the closed loop system with the MIMO PID Controller (red).

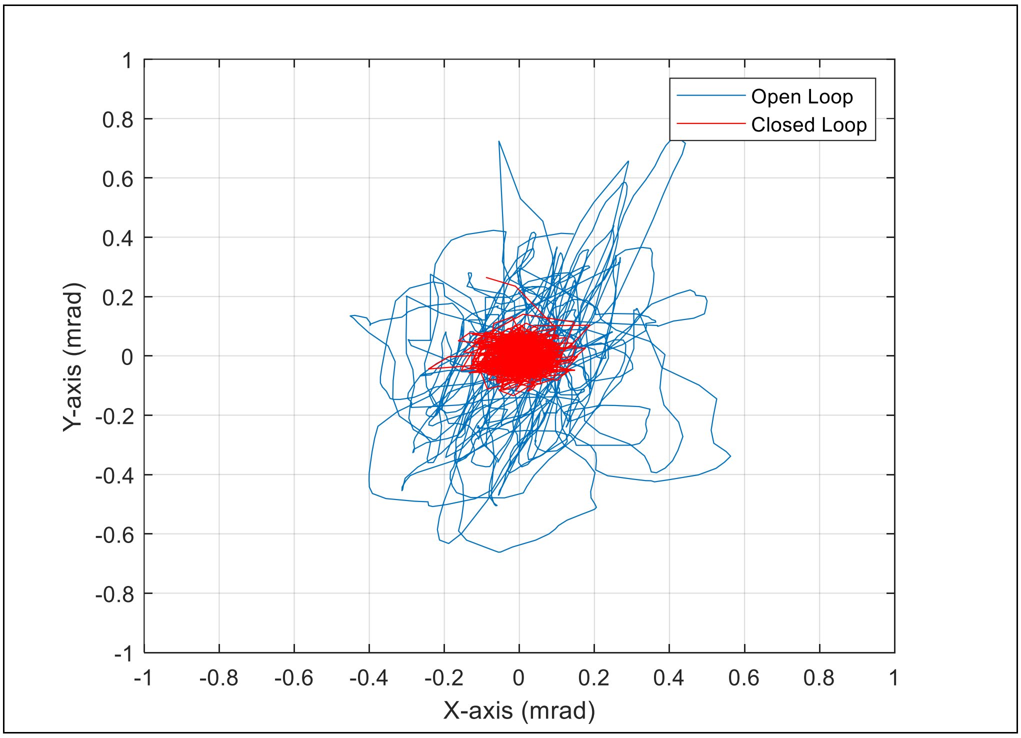

Figure 5.19. Experimental result of the distortion on the X-Y plane (blue) and stabilization with the MIMO PID controller (red)

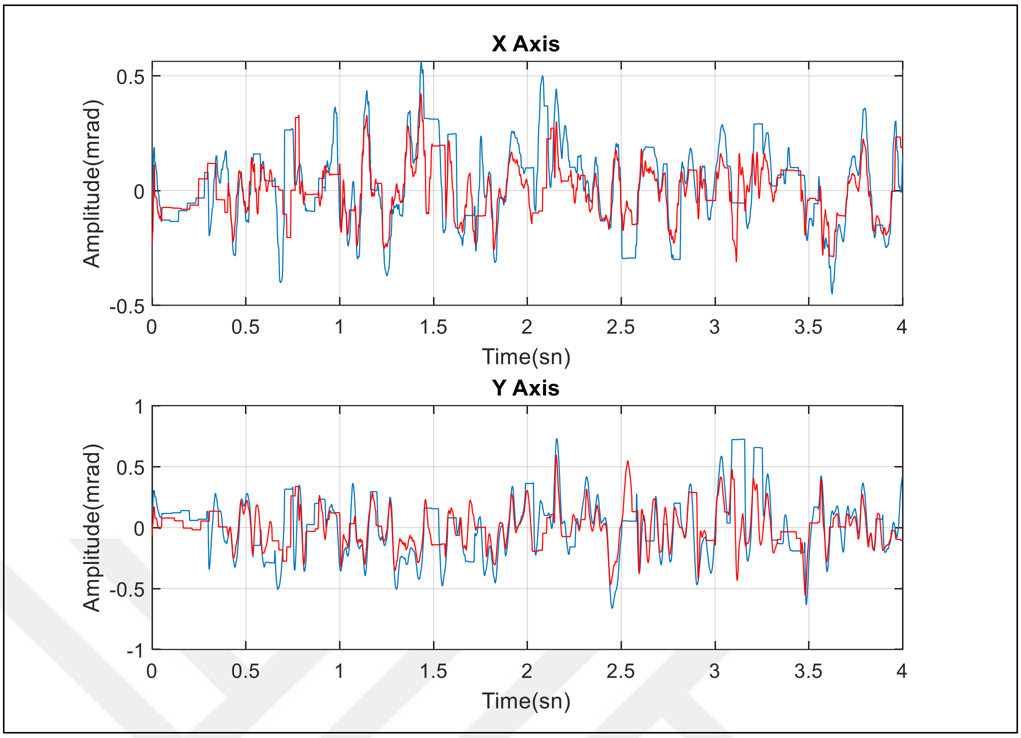

Figure 5.20. Experimental result of the open loop system (blue) and the closed loop system with the adaptive feedback controller (red).

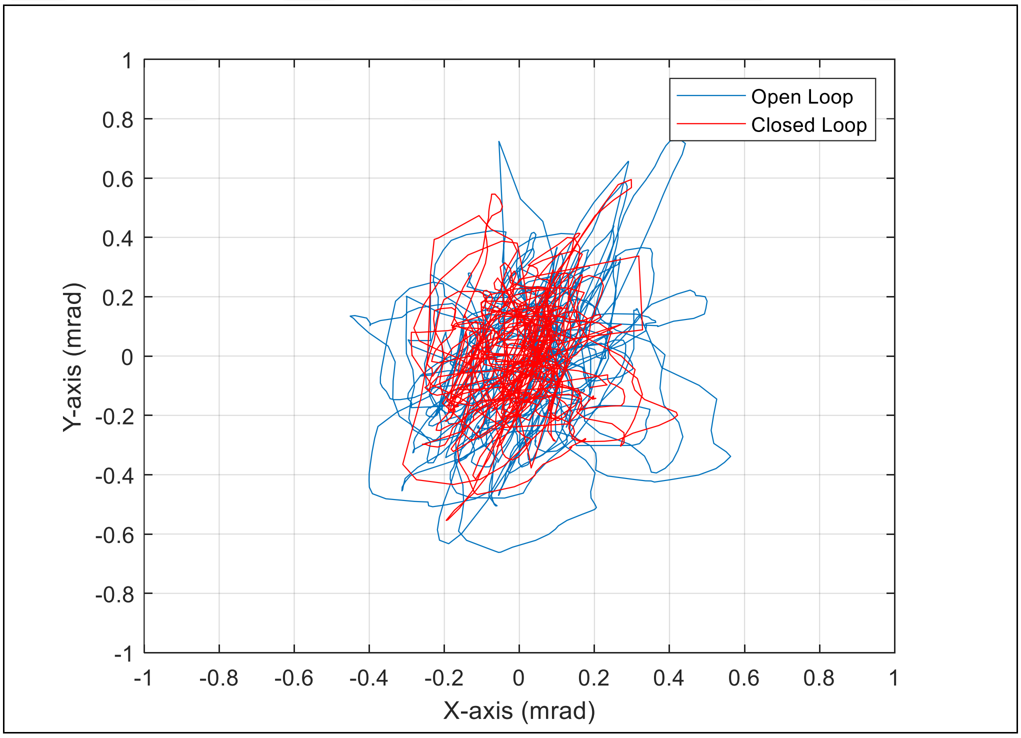

Figure 5.21. Experimental result of the distortion on the X-Y plane (blue) and stabilization with the Adaptive Feedback controller (red)

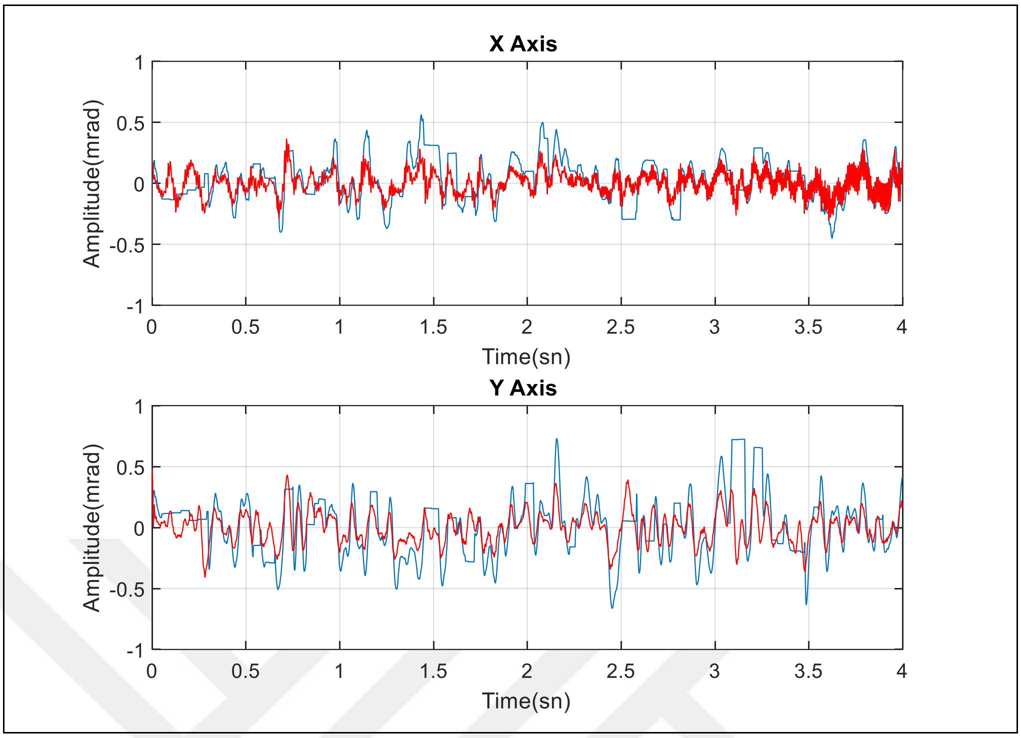

Figure 5.22. Experimental result of the open loop system (blue) and the closed loop system with the controller designed by loop shaping (red).

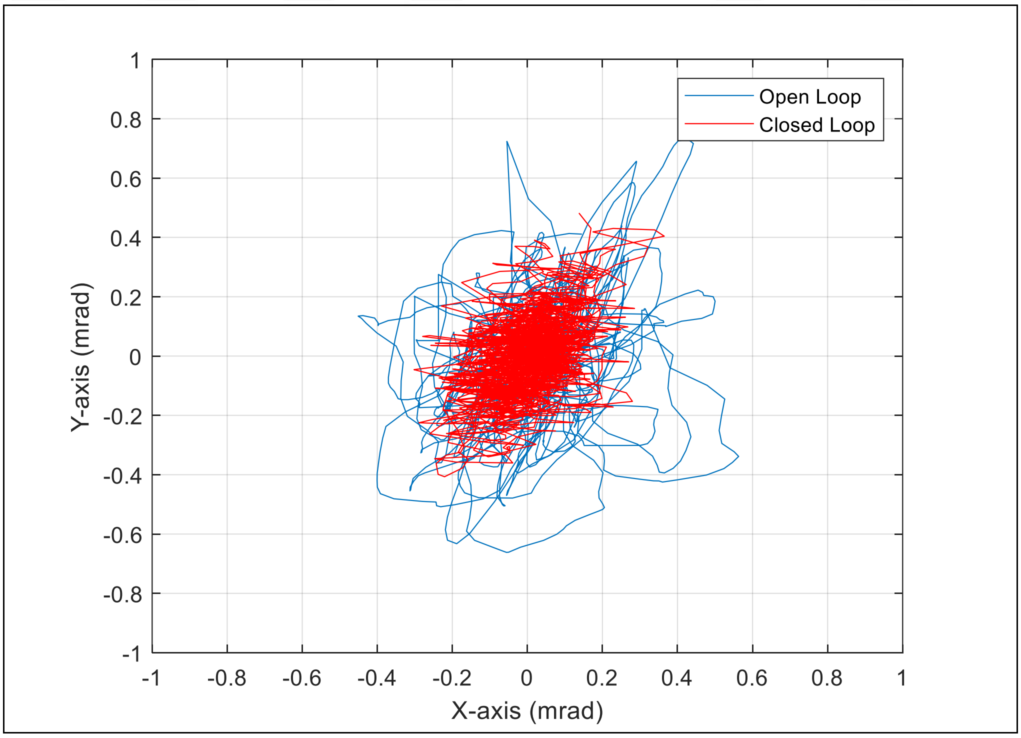

Figure 5.23. Experimental result of the distortion on the X-Y plane (blue) and stabilization with the loop shaping controller (red)

Efficiency of the controllers can be measured by two norms of output signals. In Table 5.2, two norms of application results are given, from this table, it is quite apparent that, centralized PID controller provides fairly good results when compared with other controllers.

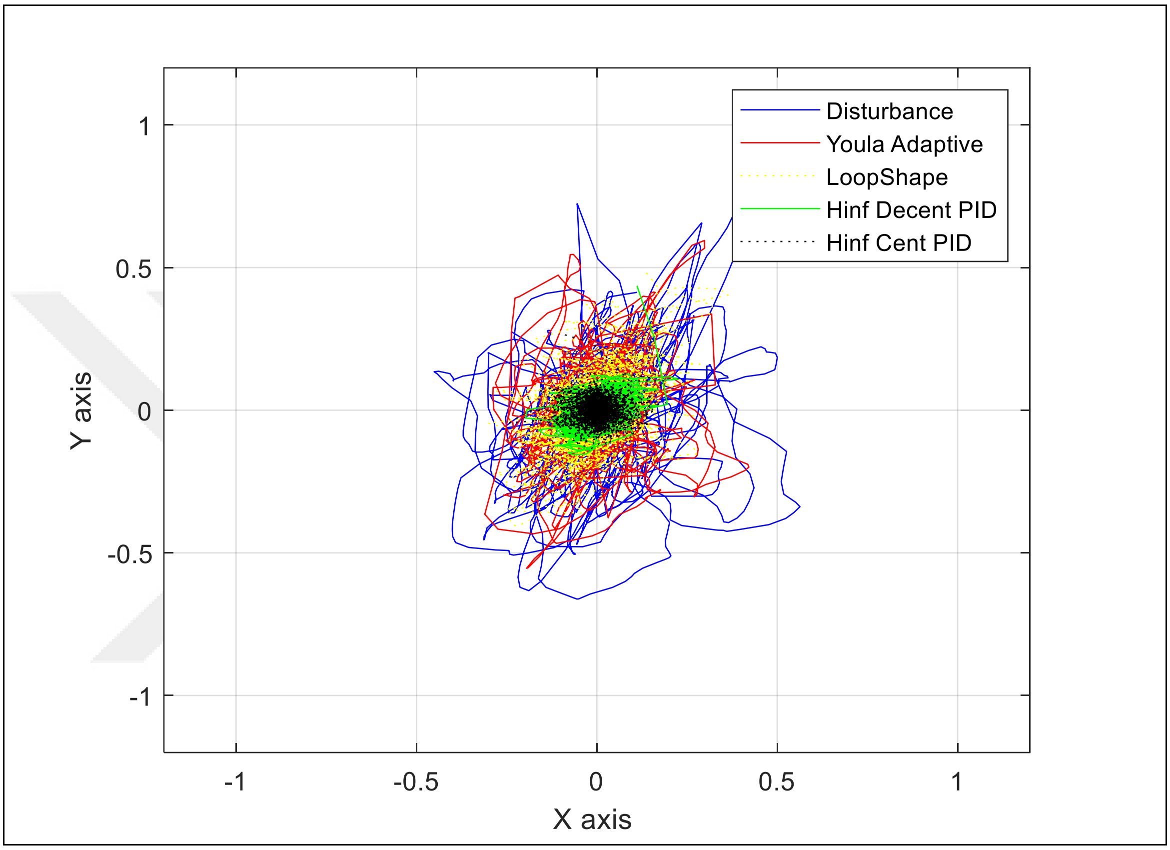

Figure 5.24. Experimental result of the distortion on the X-Y plane and stabilization with the controllers.

Table 5.2. $\|\quad\|_2$norm comparison

System Type	***X axis***	***Y axis***
Open Loop	8,0876	11,2883
Mimo Youla Adaptive Feedback Controller	5,3094	7,2765
Mimo Loop Shaping	4,2858	5,8102
Decentralized PID Controller	1,9309	2,0748
Centralized PID Controller	1,7858	1,716

5.4. DISCUSSION OF THE RESULTS

In Figure 5.2 Figure 5.3 for controlling two axis seperately decentralized 2x2 MIMO PID controller simulation results were given. By selecting suitable sensitivity and cosensitivity weight filters regarding the of atmospheric turbulence bandwith and optical sensor's noise bandwith, H infinity norm of PID controllers have been optimized. Radically increased jitter rejection capability with respect to loop shaping and adaptive type of controllers can be seen in graph.

Morever, regarding coupling between mirror axes centralized structure of 2x2 MIMO PID controller had been thought to perform better. Using same weight functions H infinity norm has been optimized and results were slightly better than decentralized 2x2 PID controller simulation. Results of rejection of axes seperately for tip and tilt axis together can be seen in Figure 5.5

In the literature, there exist two main different controller design architectures; centralized and decentralized. In the decentralized architecture, the main system is assumed to be divided into small sub-systems, and all sub-systems are controlled separately. Although application of these controllers can be considered as straightforward, the performance will be limited. Undoubtedly, the centralized architecture is the most acceptable one, but computational burden is inevitable in this case. Therefore, the designer should deal with trade-off between performance and computational cost. In this work, all results demonstrate that it is possible to get nearly the same performance as centralized-based controller by using decentralized one. The most important point is that, one should be aware of coupling structure of the overall system.

In Figure 5.13 -Figure 5.14, simulation study was performed using adaptive feedback control based on Youla-parameterization. Similar adaptive feedback controller [30] has been applied to MIMO system and nearly similar jitter rejection rates have been obtained in simulation study. Also in [35] similar controller structure with adaptive filter tuning with RLS method has been applied to jitter rejection in sattellite optical communication problem.

Figure 5.10 and Figure 5.11 shows the simulation results of the controller designed using MIMO loop shaping method. The second order butterworth low pass filter shaping the sensitivity transfer function has been designed for the controller block according to the power spectral density of the turbulence signal used as disturbance. Despite the little mathematical complexity compared to the adaptive feedback controller, it has been observed that its performance is close or even slightly better. Structured type $\mathcal{H}_\infty$ controllers exhibit dominantly good results against the other designed controllers.

Figure 5.24 shows the results of real system implementation results of the obtained controllers with simulation studies. These results were obtained by the capability not only to send the same jitter sequences to the disturbance actuator but implementation of controllers on control actuator in same switching frequency. And two norms of jitter rejection performances of the controllers are given in Table 5.2.

In the all designed controller types in this section, when the applied control signal is examined, it is seen that it does not exceed 40 percent of the actuator limits since it is below the ±2V band in all designed controllers. Since the same signal is used for the testing of all controllers, it was not necessary to limit the actuator input in this study. It has been seen in the studies that when the design is made under different strength level atmospheric disturbances(expresed with different C_N^2 value) and also different distances, it is necessary to limit the control signal with the optimal controllers or with different weighting transfer functions.

6. HYSTERESIS COMPENSATION IN PIEZOELECTRIC FAST STEERING MIRRORS

In practical applications, hysteresis in piezo-controlled fast steerable mirrors (FSM) poses a challenge for highly precise position control. In this study, nonlinear hysteresis behavior of biaxial fast steering mirrors, which are frequently used for laser beam focusing, depending on the amplitude of the input voltage and the rate of input change, is investigated. Within the scope of the thesis, hysteresis was modeled mathematically by using P-I hysteresis modeling method.

The hysteresis behavior of the system at a certain frequency and voltage is modeled by analytical modeling method using the samples taken, and an inverse P-I hysteresis compensator is designed for the modeled system.

By applying the obtained results to the real system, it has been observed that the nonlinear behavior is reduced. The anti-hysteresis behavior for both axes was examined and the effect of the interaction between the axes on the open loop compensation result was observed. It has been observed that the tracking performance of closed-loop controllers varies with or without hysteresis compensation.

6.1. PRELIMINARIES ABOUT HYSTERESIS MODELLING AND COMPENSATION METHODS

Physical modeling based on general physical principles of piezoelectric materials is possible, but this modeling is not well suited for practical use due to lack of generalization. In general, hysteresis is modeled using phemenological methods [48].Classification of different hysteresis models can seen in [59].

Since the P-I hysteresis modeling method models the hysteresis nonlinearity symmetrically, asymmetric hysteresis modeling methods have also been used in some publications to reduce the tracking error in piezoelectric actuators. Modified Prandtl Ishlinskii Model (MPI), which was created by adding dead zones to the symmetric P-I model, has been used in some publications to capture the asymmetric hysteresis model and to provide inverse hysteresis model with analytical equations [60, 61] . In addition, methods with polynomially modified hysteresis characteristic are also used to correct the asymmetric hysteresis characteristic [62]. A real-time inverse hysteresis compensation was designed in [63]. MPI inverse hysteresis compensation has been realized, which provides advanced phase margin improvement for HDD servo control systems [61]. One of the closed-loop controller design methods [64] , which uses the asymmetric hysteresis compensation method they developed to correct the asymmetrical structure of the hysteresis encountered in the control of piezo materials, is also described. In proposed work feedforward PID controller using the asymmetric hysteresis compensation method they developed improves the tracking error by 66 percent compared to the controller using the symmetric hysteresis compensation method.

The hysteresis characteristic curve changes as the input frequency and amplitude applied to the actuator changes. In [65- 67], the velocity dependent hysteresis operator is defined, since the hysteresis characteristic changes at all frequencies.

There is a study that examines the shape of the hysteresis curve that occurs when signals such as square waves and triangle waves are applied outside the sine and performs inverse hysteresis compensation with a simple curve fitting method [68].

It could be seen in [69] that the tracking performance of the controller in the feedback+feedforward structure is increased by taking the inverse hysteresis compensator as the feedforward controller. A robust adaptive controller designed in [47] has been applied to piezo FSM model calculated by considering the P-I hysteresis model and the electrical, mechanical dynamics and uncertainities. A novel the dynamic model including inverse hysteresis model as feedforward and PID feedback controller has been applied to laser beam tracking problem with FSM [70]. In [71] hysteresis nonlinearity has been reduced in the piezoelectric actuator system with feedforward inverse P-I compensator, and sliding mode controller was used for the remaining nonlinear and disturbance effects.

In atomic force microscopes, image quality is improved by using inverse hysteresis methods by providing precise control of the piezoelectric structured cantilever at the nanometer level. "Direct Inverse Asymmetric Prandtl Ishlinsky" method has been proposed in order to better compensate asymmetric hysteresis [72].

Rakotondrabe has good studies in this area. In [74] a feedforward multivariable anti hysteresis compensator has been designed for multivariable systems. In [75] employed multivariable hysteresis, creep and vibration closed loop compensator for nulti-axes piezoelectric actuator, on the other hand in [76] they developed a complete open loop control solution for same three phenomena to a single axis piezoelectric cantilever.

6.1.1. Preisach Hysteresis

The hysteresis relay is the fundamental block of the Preisach hysteresis model. It has a 2-valued structure denoted by $R_{\alpha,\beta}$[77].

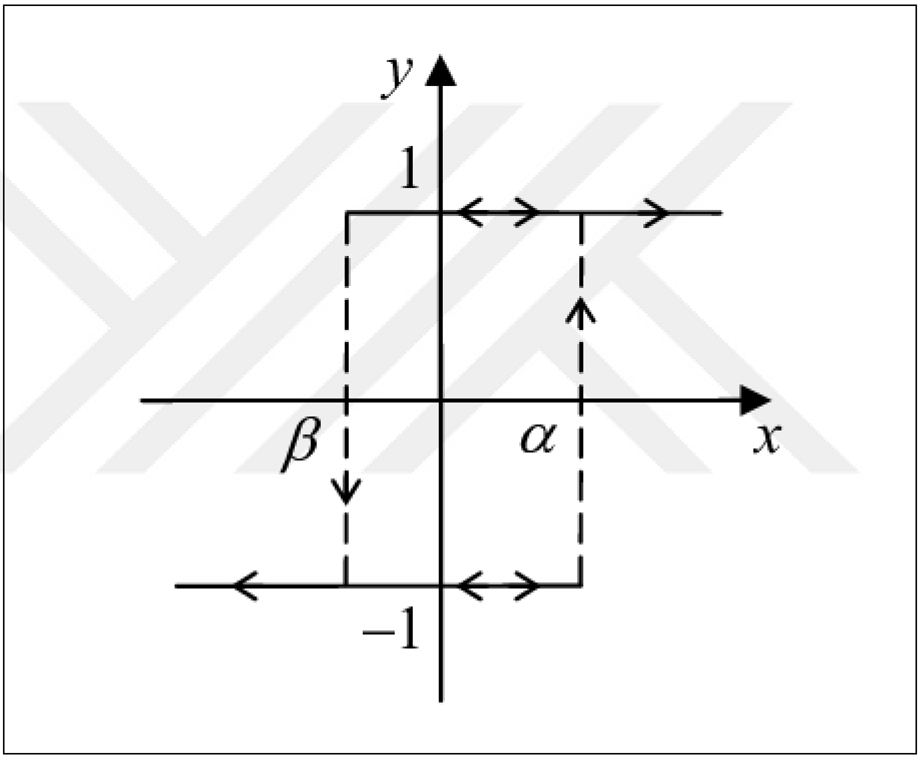

Figure 6.1. Nonideal relay

In Figure 6.1. Nonideal relay , x takes a value of +1 or -1 according to the increase or decrease of the signal indicated by the arrows and the previous value of the output y. Also actual value of x determines the y output.

This definition of the hysteresis relay shows the basic diagram. The Preisach model consists of many hysteresis relays connected in parallel, with given weights, and summed. It can be visualied in Figure 6.2.

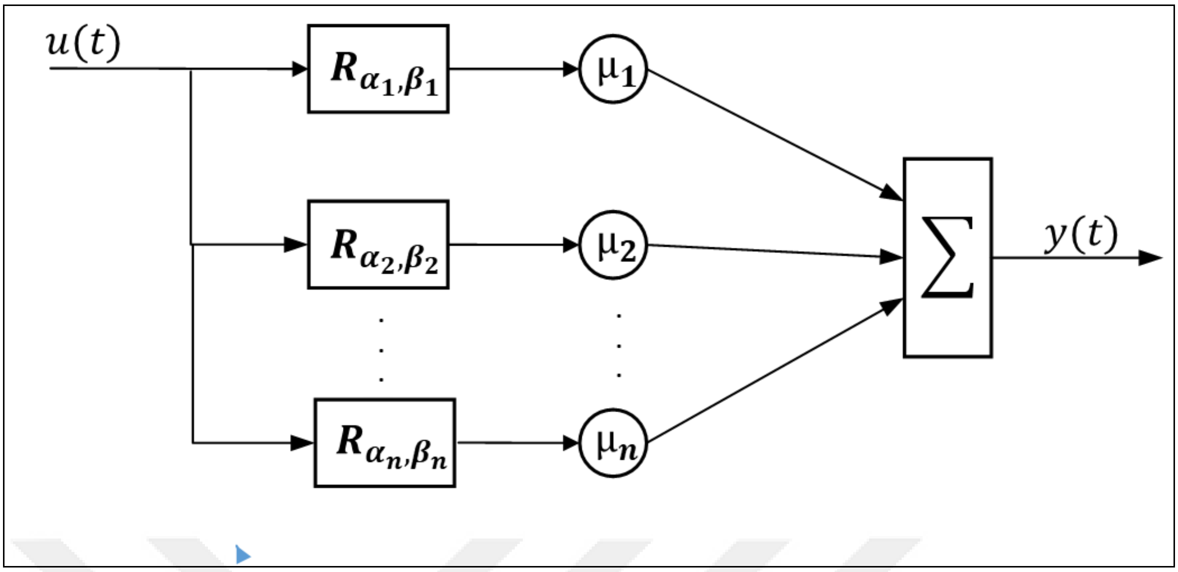

Figure 6.2. Weighted parallel connection of a finite number of nonideal relays

Each relay has different α and β tresholds and is multiplied by μ to add to the total x value. With increasing hysteresis relay particles, it provides better convergence to the real hysteresis curve.

6.1.2. Prandtl-Ishlinskii Hysteresis:

The P-I method, which describes the basic hysteresis methods, is a hysteresis modeling method derived from the Preisach method. By using this method, the symmetrical hysteresis model can be determined easily .

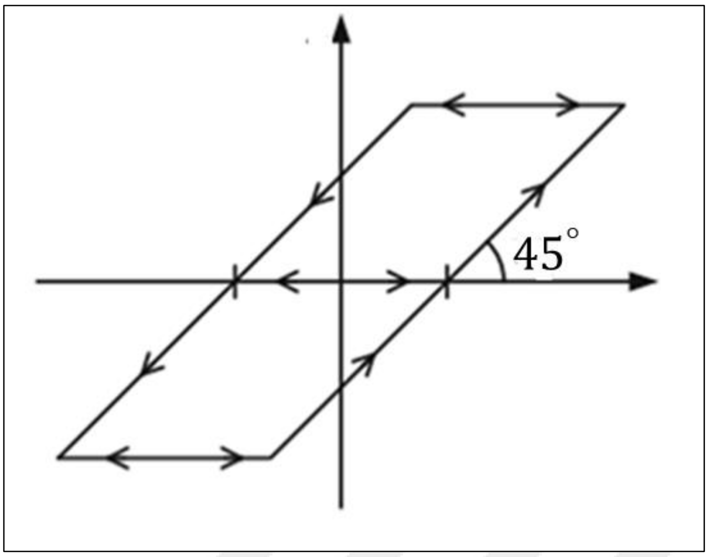

Figure 6.3. Backlash operator H_r

Backlash operator is the elemantary operator of P-I hysteresis model. The backlash operator Hr is shown in Figure 6.4, which is defined by

$$y(t) = H_r[u, y_0](t) = max\{u(t) - r, min\{u(t) + r, y(t - T)\}\} \tag{6.1}$$

$$y(0) = max\{u(0) - r, min\{u(0) + r, y_0\}\} \tag{6.2}$$

Where $u(t)$ denotes input voltage, r is the threshold value of hysteresis, T is the sample time, y_0 is the initial condition usually taken as 0.

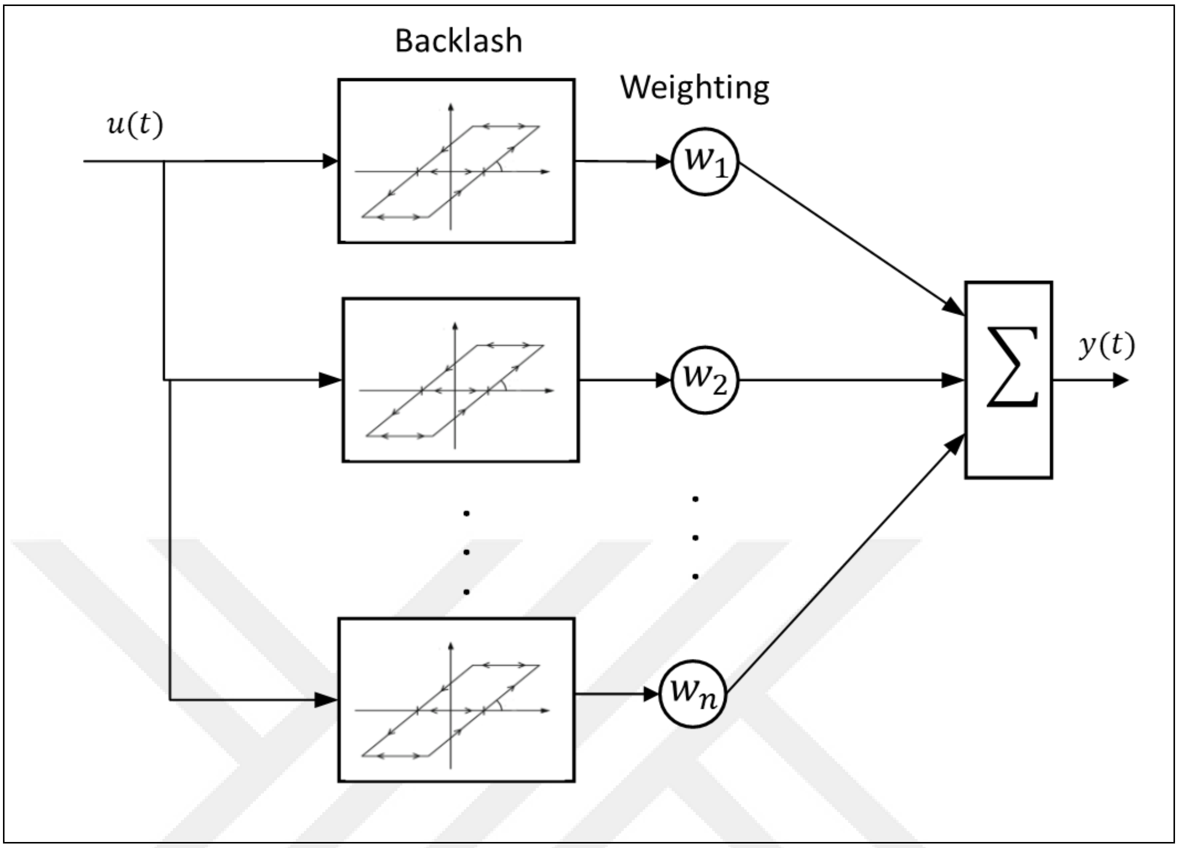

Figure 6.4. Prandtl Ishlinsky hysteresis operator

The P-I model is the sum of the backlash operators at different threshold and weighting values. The input and output graph of the backlash operator is shown in Figure 6.4. If we express the sum of the backlashes:

$$y(t) = \mathrm{w}_h^T \mathrm{H}_r[u, \mathrm{y}_0](t) \tag{6.3}$$

$$\mathbf{x}_0 = [x_{00}, x_{01}, \dots, x_{0n}]^T, \text{for } 0 = r_0 < r_1 < r_n < +\infty \tag{6.4}$$

$$\mathrm{H}_r[u, \mathrm{y}_0](t) = [H_r[, y_{00}](t),, H_r[u, y_{01}](t), \dots, H_r[u, y_{0n}](t)]^T \tag{6.5}$$

$$\mathrm{w}_h^T = [w_{h0}, w_{h1}, \dots, w_{hn}] \tag{6.6}$$

$$\mathbf{r} = [r_0, r_1, \dots, r_n] \tag{6.7}$$

6.1.3. Inverse Prandtl-Ishlinskii Hysteresis

Classical Prandtl Ishlnsky Method 'Inverse Hyteresis Equations are given as,

$$w'_{h0} = \frac{1}{w_{h0}} \tag{6.8}$$

$$w'_{hi} = \frac{-w_{hi}}{\left(\sum_{j=0}^{i} w_{hj}\right)\left(\sum_{j=0}^{i-1} w_{hj}\right)}, \qquad i = 1, \dots, n \tag{6.9}$$

$$r'_i = \sum_{j=0}^{i} w_{hj}\left(r_i - r_j\right), \ i = 0,1, \dots, n \tag{6.10}$$

$$y'_{0i} = \sum_{j=0}^{i} w_{hj} y_{0i} + \sum_{j=i+1}^{n} w_{hj} y_{0j}, \ i = 0,1, \dots, n \tag{6.11}$$

6.1.4. Modified Prandtl-Ishlinskii Model

The P-I operator has the same symmetric property as the backlash operator withrespect to the center point of the loop formed by the operator. Hence, the model accuracy of P-I operator will be reduced for the situations where the hysteresis loopsare not symmetric. In order to overcome this issue, a saturation operator is adoptedto connect in serial with the hysteresis operator.

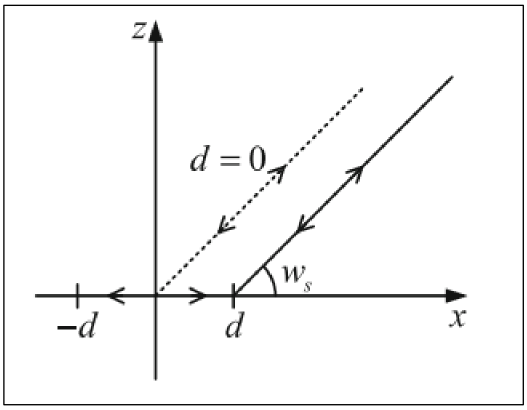

Figure 6.5. Dead Zone Operator S_d

$$S_d[y](t) = \begin{cases} max\{y(t) - d, 0\}, & d > 0 \\ y(t), & d = 0 \end{cases} \quad (6.12)$$

Output of the dead zone block with weighting functions

$$z(t) = \mathrm{w}_s^T \mathrm{S}_d[y](t) \quad (6.13)$$

Therefore, the modified P-I operator is derived as follows:

$$z(t) = \Gamma[u](t) = \mathrm{w}_s^T \mathrm{S}_d\left[\mathrm{w}_h^T \mathrm{H}_r[u, \mathrm{y}_0]\right](t) \quad (6.14)$$

6.1.5. Hysteresis Compensation

For reducing the nonlinearity effects of piezo inverse hysteresis should be applied before piezo stack

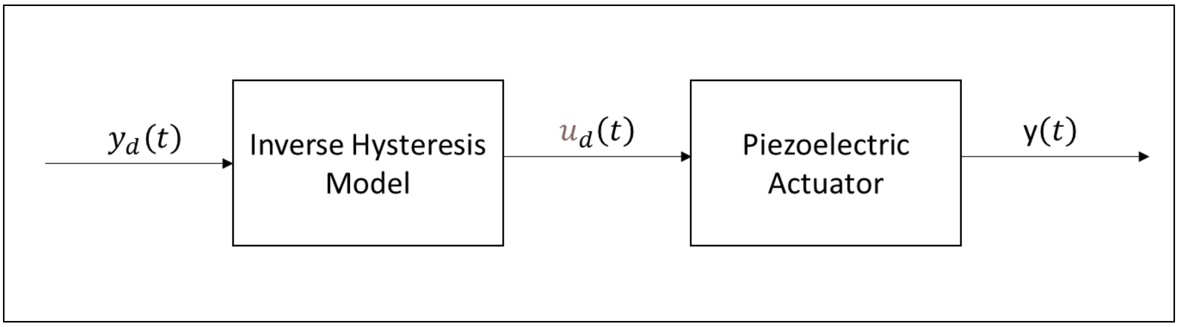

Figure 6.6. Linearizing piezo hysteresis

The input voltage changed by the inverse hysteresis model is used to drive the piezoelectric ceramic actuators, and the displacement data in the x and y axis are measured via the PSD sensor, converting the nonlinear hysteresis curve to a linear curve.

6.2. CLOSED LOOP AND OPEN LOOP EXPERIMENTS WITH EXPERIMENTAL SETUP

Similar experimental setup to fine tracking controller setup has been used for experiments. The system consists of MRC beam stabilization kit and National Instruments PCIE6363 analog data acquisition card and He-Ne laser source. The laser beam is reflected on the Position Sensitive Detector (PSD) by reflecting from the FSM. The system design block diagram is given in Figure 6.7.

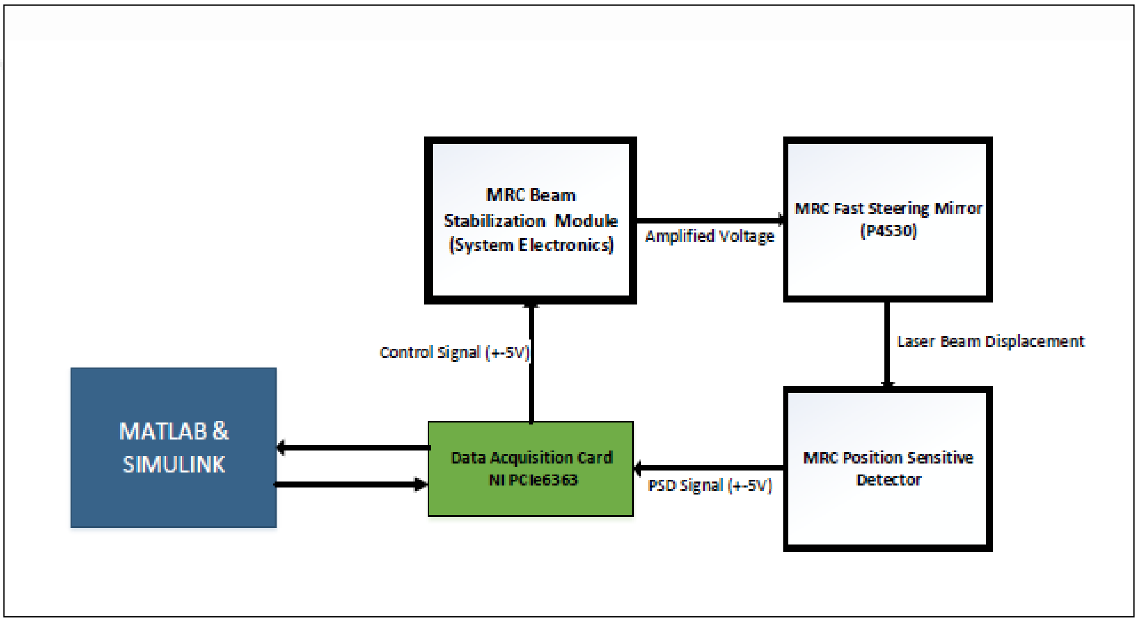

Figure 6.7. Experimental setup block diagram

Pictures of optical and electronic components in the setup given in the Figure 6.8. Also stabilized He-Ne laser is used in the setup.

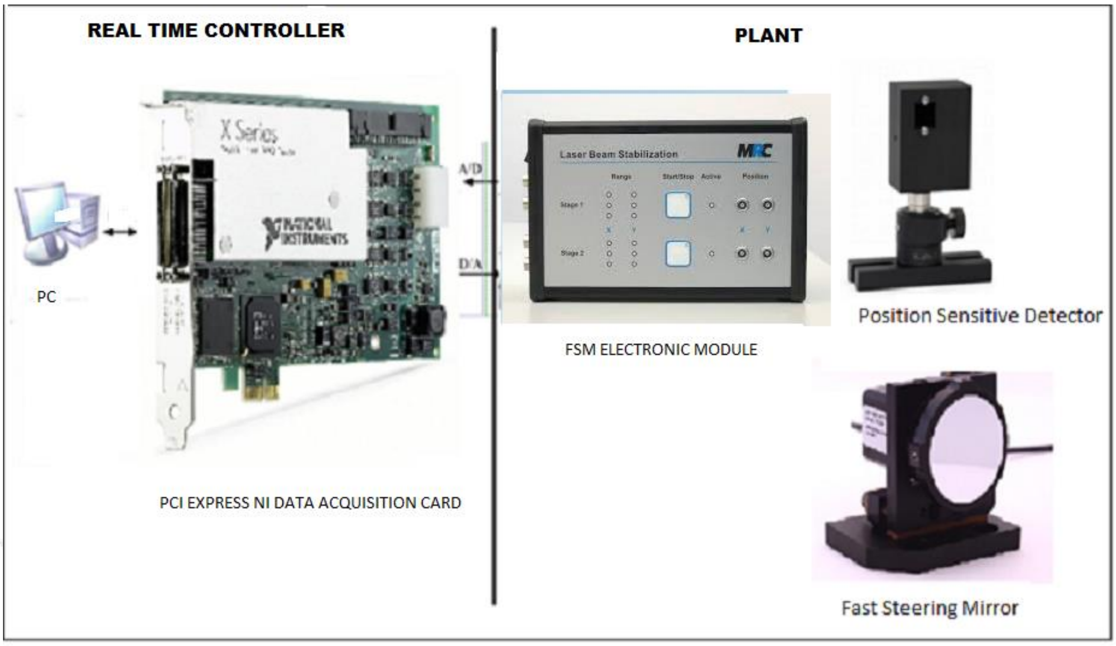

Figure 6.8. Electronic modules used in the setup

Firstly with experimental setup three different experiments has been performed. In the first experiment sine signal was applied to FSM inputs at increasing frequencies with the fixed amplitude given by the equation $\mathrm{Y1} = 0.5 * \sin(2 * pi * F * t)$. F=1hz, 5hz, 10hz inputs were applied and outputs from Position Sensitive Detector (PSD) are shown in Figure 6.9. As it is seen that the hysteresis increases as the frequency of the input signal increases.

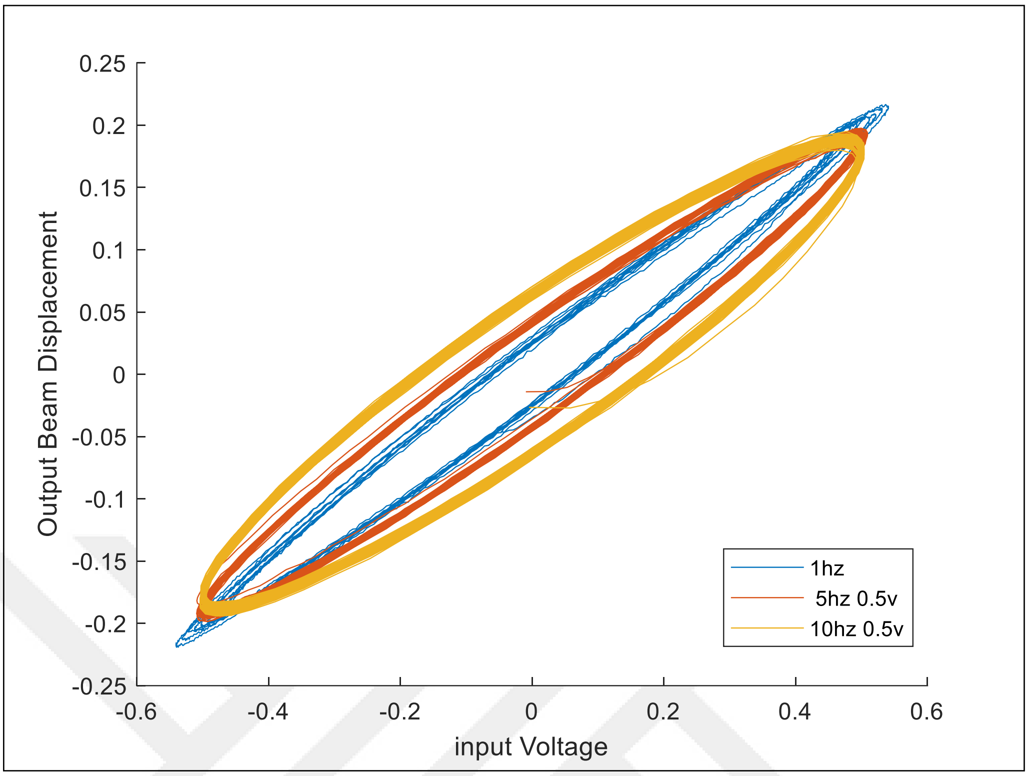

Figure 6.9. Experiment 1, different frequency inputs

In other experiment, sine signal given by the equation $Y2 = 2 * \sin(2 * pi * F * t)$ has been applied to piezo FSM input with frequencies 1hz, 5hz, 10hz,20hz, 40hz. It is seen that the increase in hysteresis becomes more pronounced as the frequency increases. Results are shown in Figure 6.10.

Last experiment has been carried out with $Y3 = G * \sin(2 * pi * 10 * t)$ signal. Amplitude G has been changed as 0.5v, 1v, 2v. Nonlinearity with increasing amplitude can be seen in Figure 6.11. It is seen that the nonlinearity decreases at low amplitudes, and the hysteresis increases at increasing amplitudes and the nonlinear characteristic becomes more pronounced.

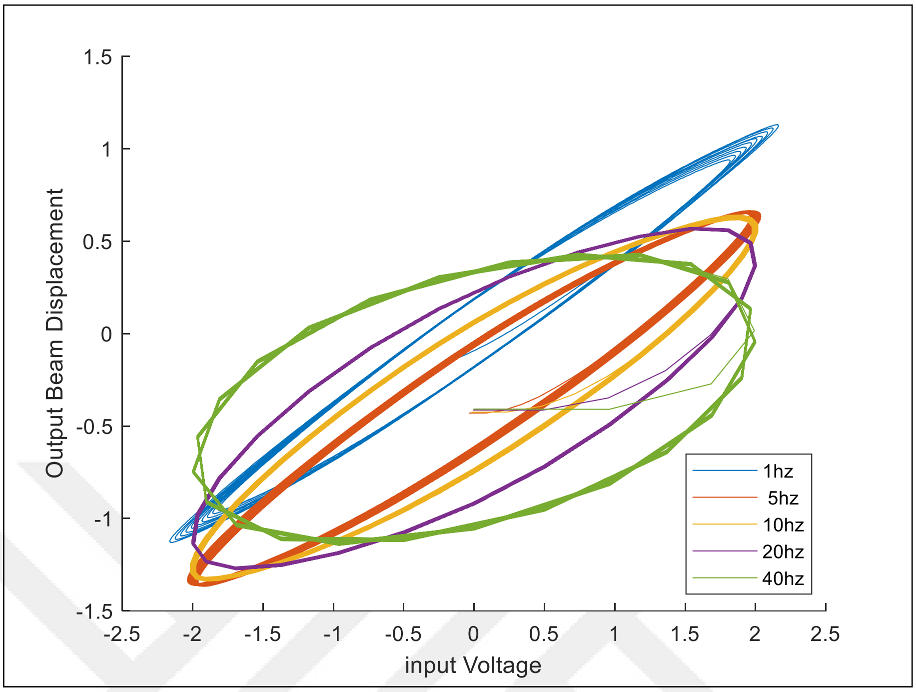

Figure 6.10. Experiment 2, more different frequency inputs

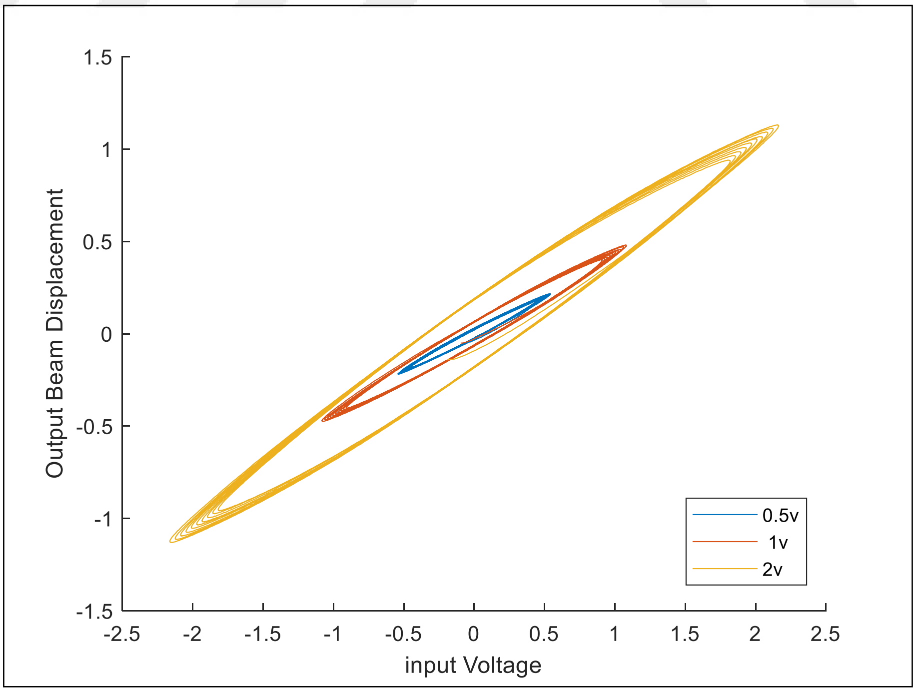

Figure 6.11. Experiment 3, different amplitude inputs

6.2.1. Open Loop Hysterezis Compensation and Identification of Hysteresis Parameters

Considering the classical Prandtl-Ishlinskii model, if the procedure in [79] is followed step by step, identification of hysteresis parameters, weighting and threshold values can be done.

The hysteresis curve obtained from the experiment-1 for 10 Hz 0.5 V sine input is taken with sampling at six points and the bw and Δy parameters are determined first. The sine input u(t) should be applied to the actuator input. The y(t) amplitude input covers the specific PSD output scale. On the obtained hysteresis curve (x(t), y(t))-map, n Backlash numbers should be determined.

In the y(t) domain, it is divided into n+1 regular or irregular parts. In Figure 6.12, it is divided into seven parts and gives an approximation of the hysteresis with six backlash. The bandwidth parameter $\mathrm{bw_i}$ can be calculated from the difference of the values of the vector x, and the difference output vector Δy can also be calculated from the difference of the vector values corresponding to y from the increasing curve.

$\Delta y$and bw_{i}bandwidth values can be calculated using the following equations.

$$\Delta y_{i-1} = y(i) - y(i-1) \text{ ; i=2..8} \tag{6.15}$$

$$bw_1 = |x(2) - x(1)| \tag{6.16}$$

$$\mathrm{bw_i} = \mathrm{bw_{i-1}} + |\mathrm{x(i)} - \mathrm{x(i-1)}| \text{ ; i=2..8;} \tag{6.17}$$

The calculated values are given in Table 6.1

,

Table 6.1. Calculated bandwidth bw_{i} and Δyi values

i	bw_i	Δy_i
1	0.05	-0.188
2	0.3	-0.130
3	0.5	-0.065
4	0.7	0.1870
5	0.9	0.01
6	0.99	0.105
7	1	0.16
8	1.05	-

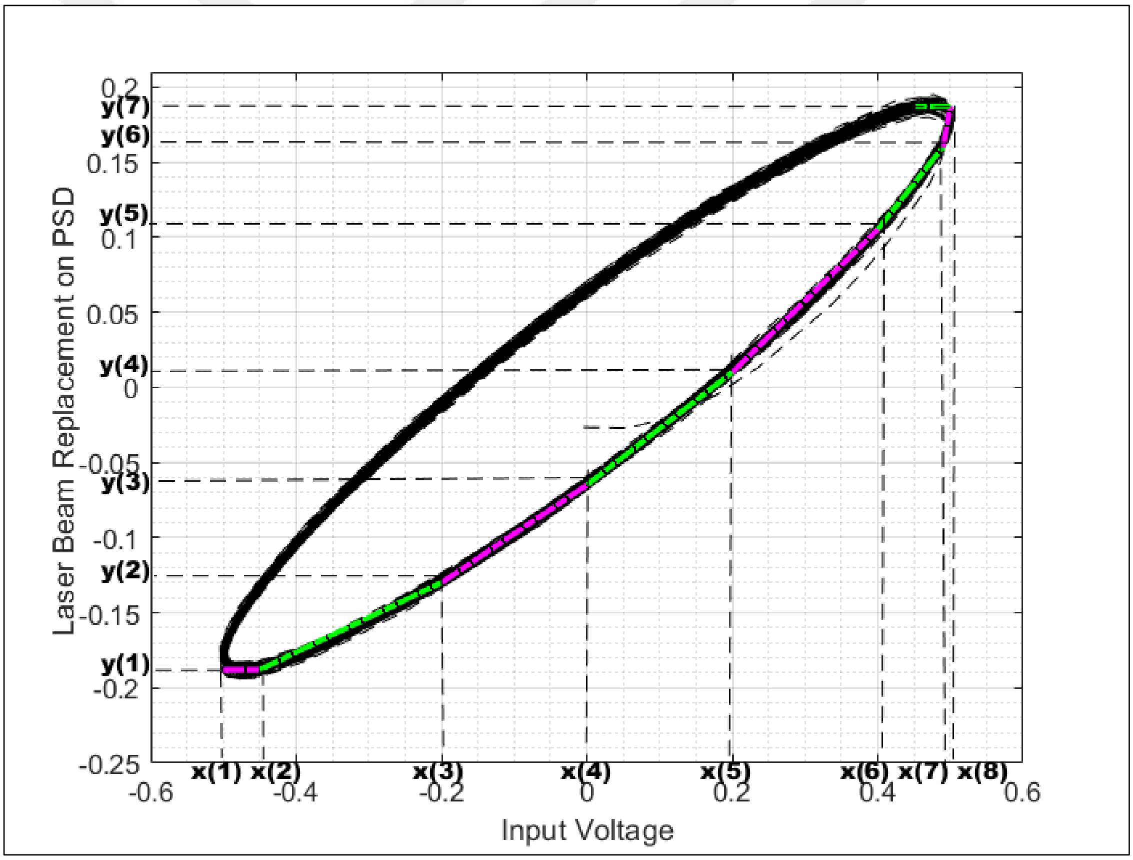

Figure 6.12. Sampling of 10hz 0.5v hysteresis curve from Experiment-1 at 6 points

r and w vectors can be calculated as follows

$$bw_i = 2 * r_i \tag{6.18}$$

$$\Delta y_j = \sum_{i=1}^{j} \left(bw_{j+1} - bw_i\right) \cdot w_i \tag{6.19}$$

Equation (6.19) can be written in matrix form taking A as circular matrix

$$\{\Delta y\} = [A] \cdot \{w\}$$

$$A = \begin{pmatrix} (bw_2 - bw_1) & 0 & \cdots & 0 \\ (bw_3 - bw_1) & (bw_3 - bw_2) & \ddots & \vdots \\ \vdots & \ddots & 0 & \\ (bw_{n+1} - bw_1) & (bw_{n+1} - bw_2) & \cdots & (bw_{n+1} - bw_n) \end{pmatrix} \tag{6.20}$$

Solution of w is

$$\{w\} = [A]^{-1} \cdot \{y\} \tag{6.21}$$

Identified hysteresis values in (6.2) are obtained by calculating the r and w vectors for 6 points using the equations. Figure 6.13. shows the hysteresis curve plotted together with the measurement result, using the calculated values.

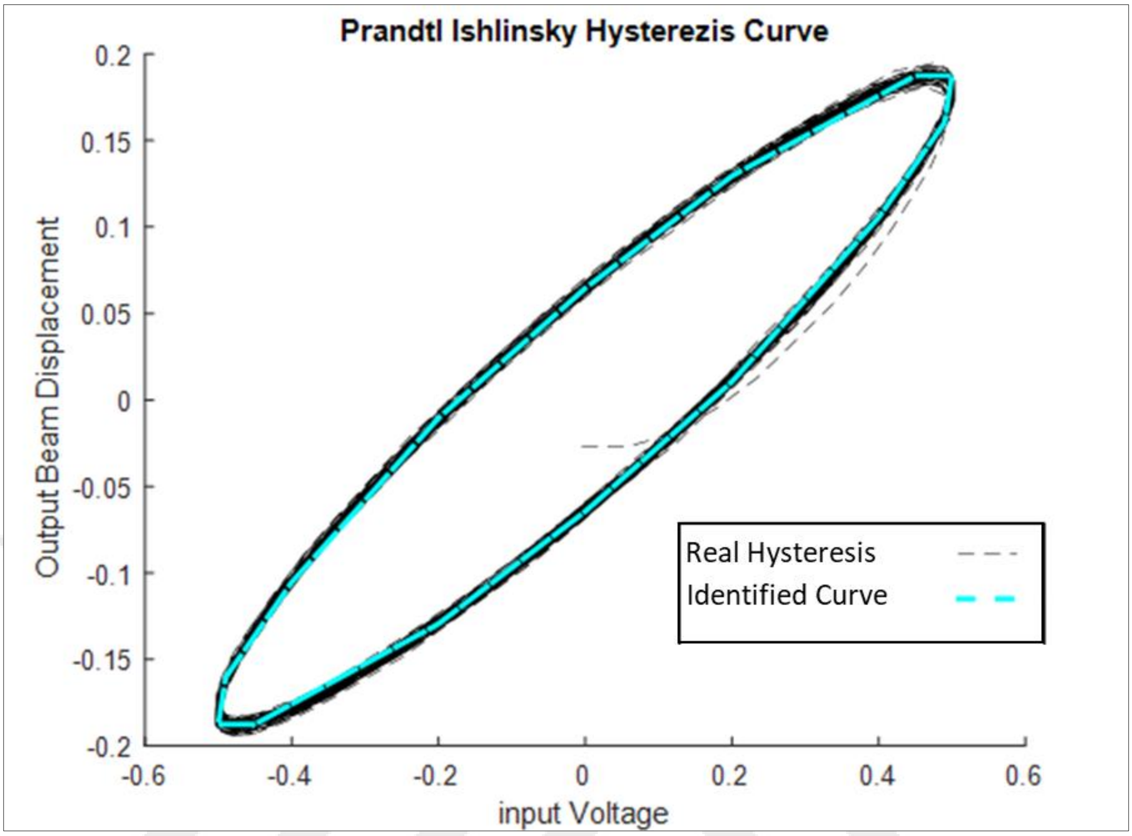

Figure 6.13. Measured hyteresis curve vs identified curve

Table 6.2. Identified forward hysterezis parameters for 10 hz 0.5v sine input

i	w_{fw}	r_{fw}
1	0.232	0.025
2	0.093	0.15
3	0.05	0.25
4	0.1	0.35
5	0.13611	0.45
6	2.089	0.495

The values in Table 6.3 are obtained by calculating the Inverse P-I hysteresis parameters using the equations given in Section 6.1.3.

Table 6.3. Inverse Hysterezis Parameters 10 hz 0.5v

i	w_{inv}	r_{inv}
1	4.31034	0
2	−1.23342,	0.029
3	−0.410256	0.0615
4	−0.561404	0.099
5	0.4689	0.1465
6	−1.26599	0.174

Simulink scheme designed for applying calculated inverse hysteresis model to real system is seen in Figure 6.14. w_{inv} and r_{inv} values given in Table 6.3 is constructed as anti hysterezis block.

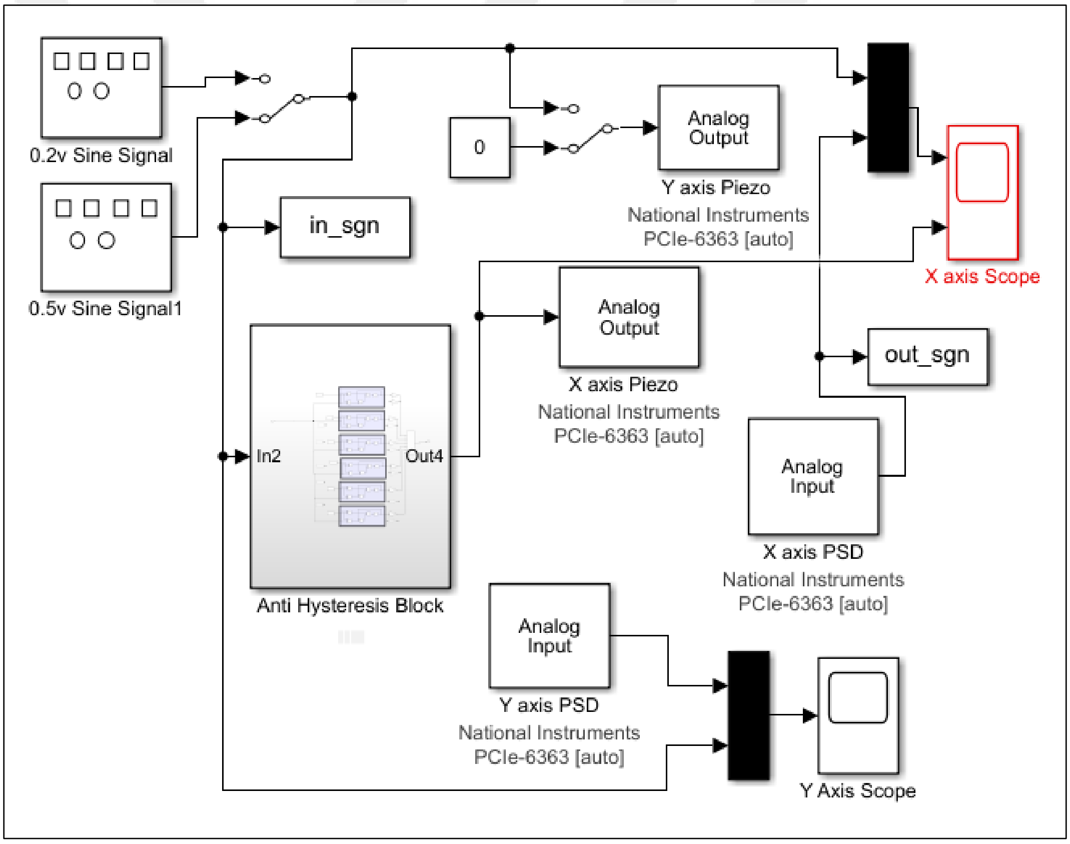

Figure 6.14. Simulink model

The inverse hysteresis model created with the obtained values is given to the input of the system, and a linear input-output graph is obtained as in Figure 6.15.

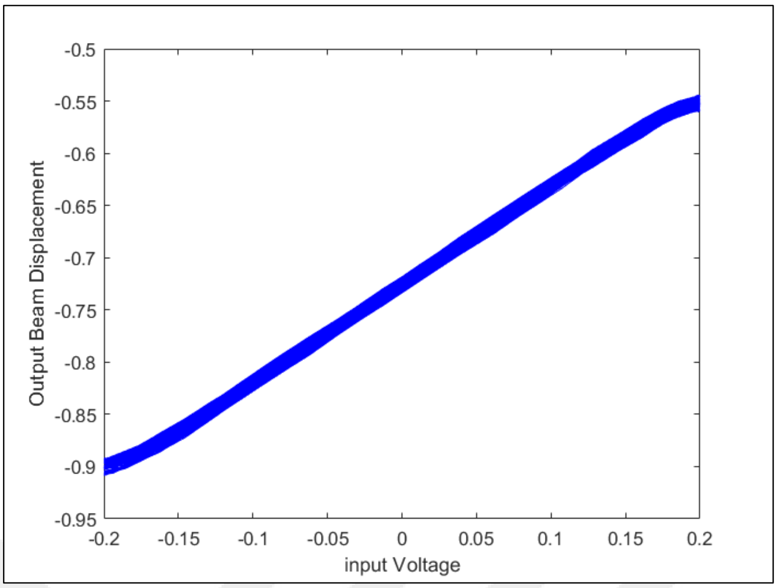

Figure 6.15. Input-output graph of one axis formed as a result of applying hysteresis compensation

Since the optical table dimensions are limited in the experimental setup, ±5V used for FSM movement corresponds to ±2V signal at the PSD sensor output. Therefore, applying ±0.5V to the anti-hysteresis compensation block input corresponds to applying ±0.2V to the actuator input. As seen in Figure 6.11. the hysteresis characteristic that occurs at different amplitude inputs is different.Since there is 30 percent coupling between the x and y-axes in the FSMs we used in the experimental setup, for example, when the x-axes is energized, it causes an amplitude increase of 30 percent in the y-axes .This can reduce the effect of the anti-hysteresis compensator designed to a certain extent.

0.2V 10Hz sine input is applied to the x-axes input with an anti-hysteresis compensator. Constant 0V input is applied to the y-axes input. In Figure 6.15. it is seen that the input and output of the real system is linear.

Hysteresis compensator was applied for the x-axes while the same sine signal is applied to the y-axes. There is around 30 percent interaction between the axes. The results are shown in Figure 6.16. In this case linearity degrades. But hysteresis compensator still has effect to reduce nonlinearity.

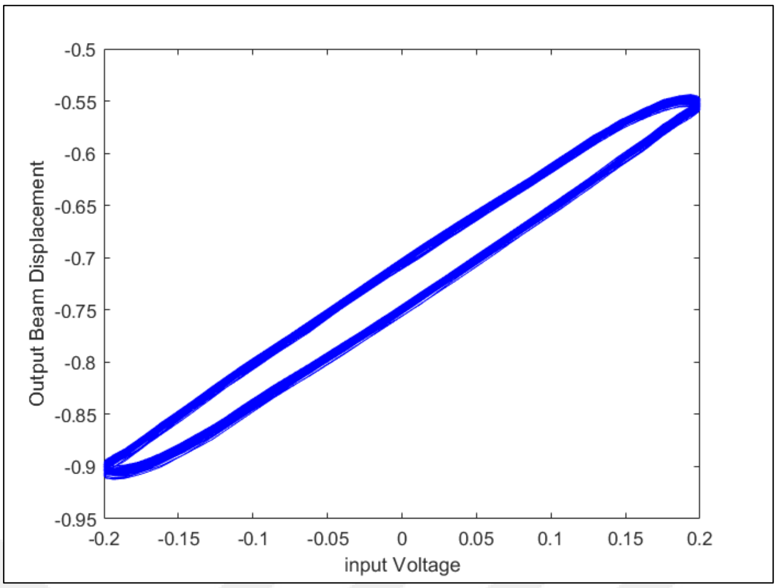

Figure 6.16. Input-output graph of one axis formed as a result of hysteresis compensation when the other axis is active

With same inverse hysteresis model values, 10Hz 0.2v triangle signal has been applied to the system. In hysteresis compensated case and non-compensated case graphs can be seen in Figure 6.17. Input-output graph in both case also shown in Figure 6.18.

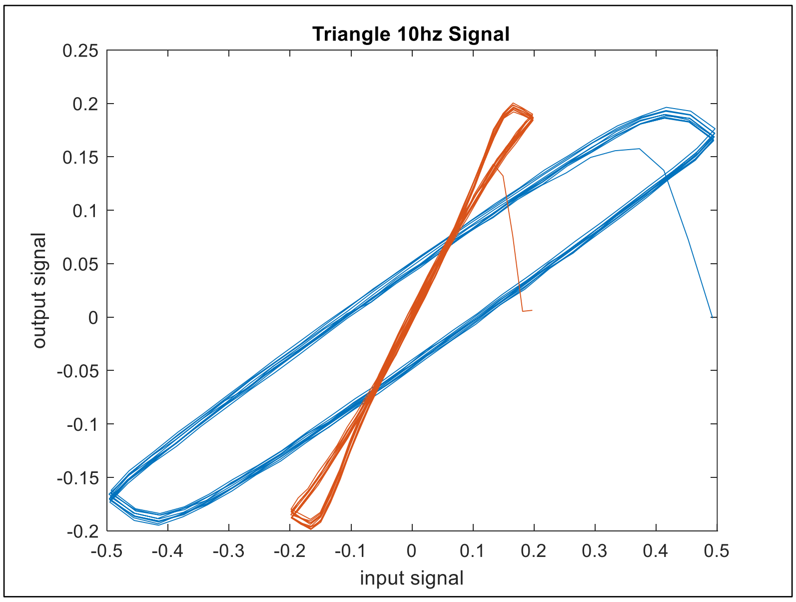

Figure 6.17. Triangle input, non-compensated cases (blue) hysteresis compensated case (red)

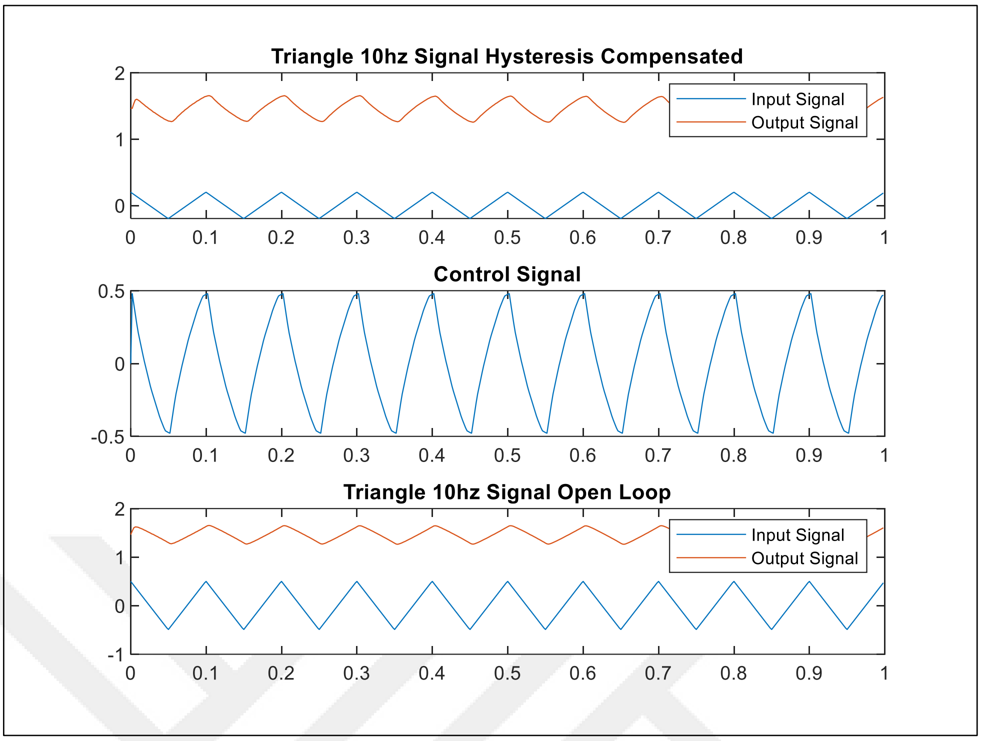

Figure 6.18. Input output signals in compensated and non-compensated cases,

6.2.2. Two Axis Fast Steering Mirror Closed Loop Control Performance with Hysteresis Compensation

Obtained results will be applied to real system and results will be obtained for two axis piezo fast steering model. The controller will be designed for the system and applied to real results. Intended to design system has been shown in Figure below

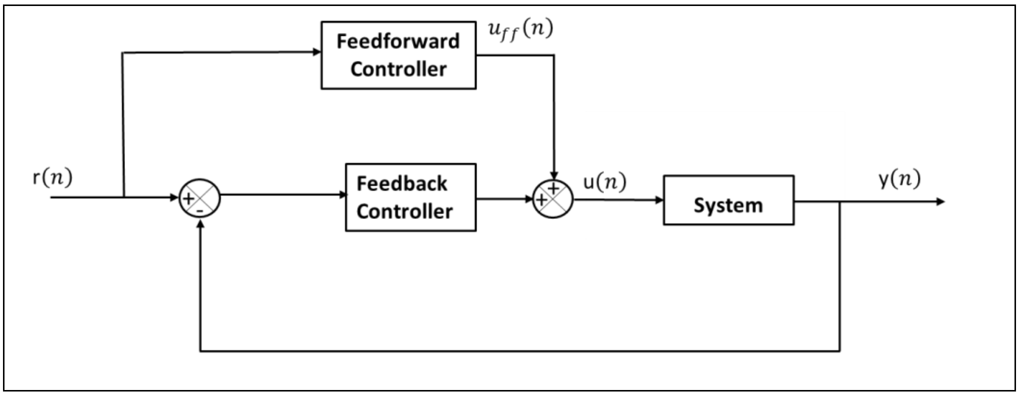

Figure 6.19. MIMO feedback+feedforward controler .

In this experiment feedforward side will include compensation for nonlinear effects of hysteresis and feedback controller will be a linear controller for the FSM.

The controller is in the MIMO PI structure and is adjusted using the manual tuning method. Contoller equation is given

$$U_{mimo} = \begin{bmatrix} U_{PI} & 0 \\ 0 & U_{PI} \end{bmatrix}$$
$$U_{PI} = 2 + \frac{600}{s} \tag{6.22}$$

First closed loop experiment is applied to system with sine reference signal to both axes.

0.2V 10 Hz sine input is applied to both x-axes and y-axes inputs with an anti-hysteresis compensator and without compensator with closed loop PI controller. Tracking errors and reference vs output signals shown in the figures below. Same calculated anti hyteresis vectors given in Table 6.3 is used for this experiments.

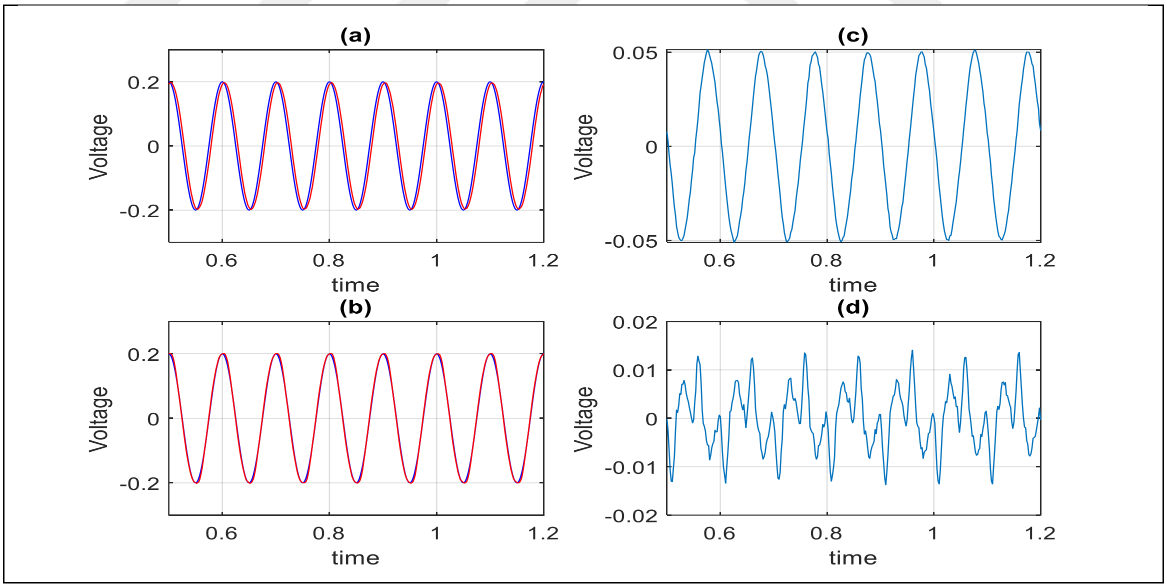

Figure 6.20. 0.2v 10Hz sine reference, y-axis closed loop results, (a) without hysteresis compensation(blue-refererence,red output), (b) with hysteresis compensation(blue-refererence,red output), (c) tracking error without hysteresis compensation, (d) tracking error with hysteresis compensation

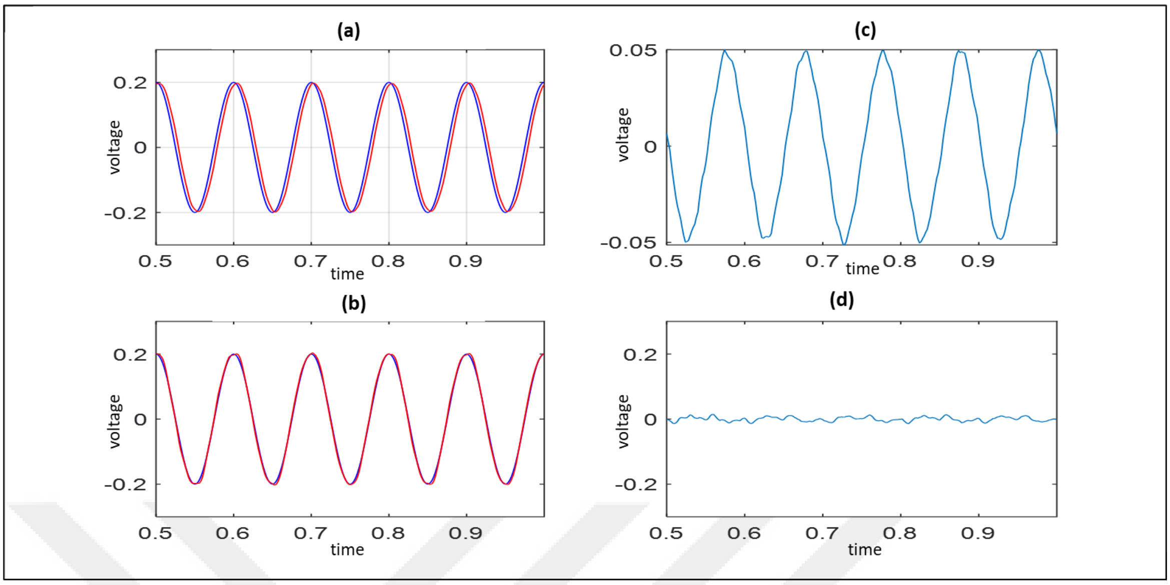

Figure 6.21. 0.2v 10Hz sine reference, x-axis closed loop results, (a) without hysteresis compensation(blue-refererence,red output), (b) with hysteresis compensation(blue-refererence,red output), (c) tracking error without hysteresis compensation, (d) tracking error with hysteresis compensation

As seen in the graphics, tracking error is radically reduced when hysteresis compensation is applied. For closed loop experiment again triangle signal is applied and controller outputs is seen for the cases when hysteresis compensator on and off. Also tracking errors is seen in the same graphs.

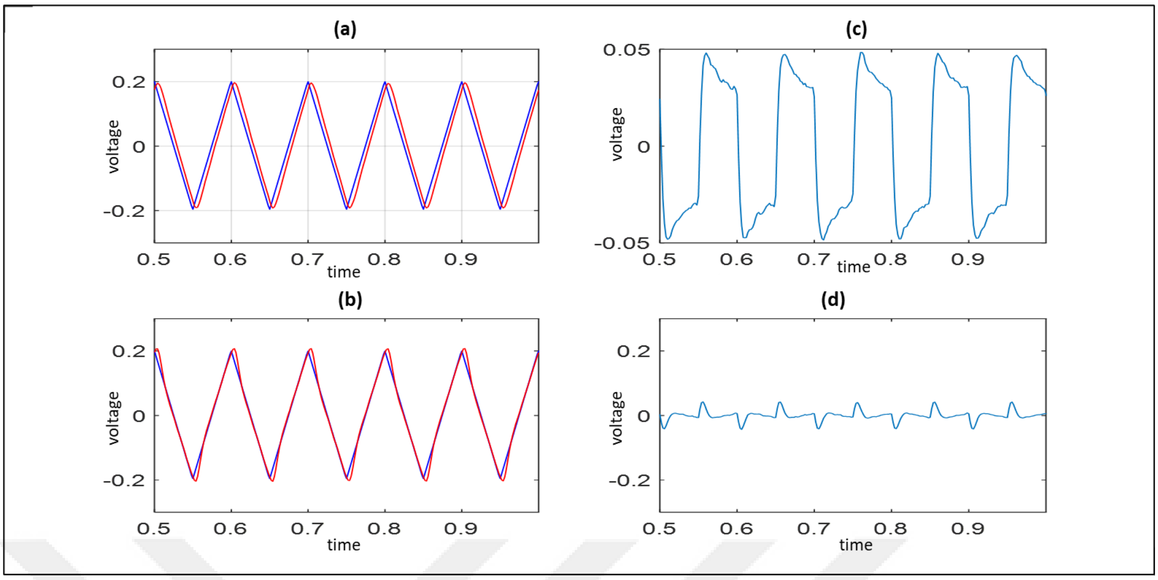

Figure 6.22. 0.2v 10Hz triangle reference, y-axis closed loop results, (a) without hysteresis compensation(blue-refererence,red output), (b) with hysteresis compensation(blue-refererence,red output), (c) tracking error without hysteresis compensation, (d) tracking error with hysteresis compensation

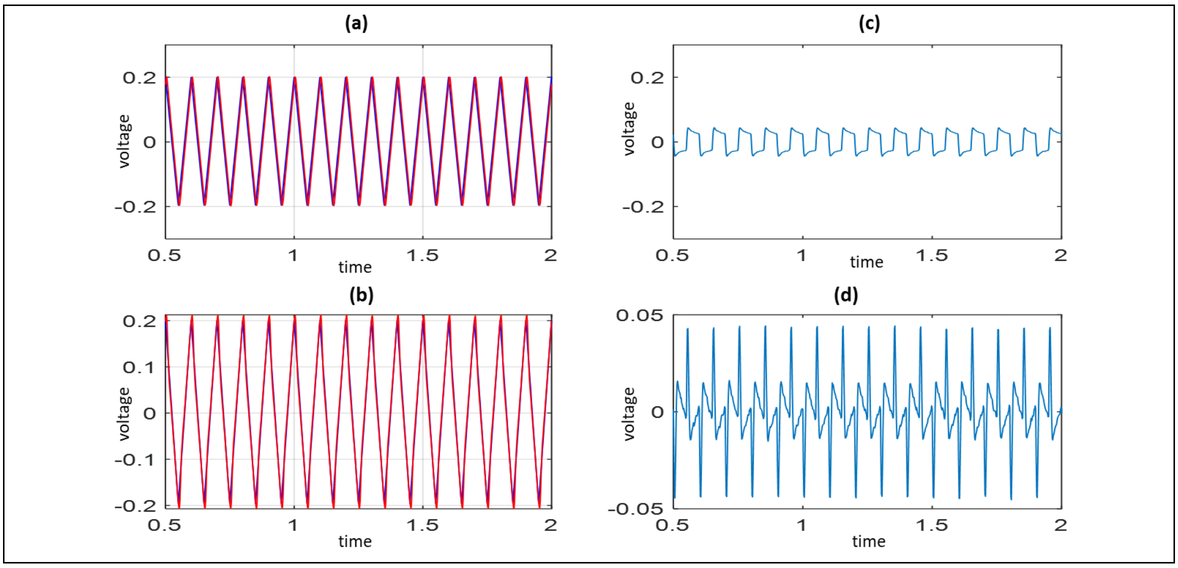

Figure 6.23. 0.2v 10Hz triangular reference, x-axis closed loop results, (a) without hysteresis compensation(blue-refererence,red output), (b) with hysteresis compensation(blue-refererence,red output), (c) tracking error without hysteresis compensation, (d) tracking error with hysteresis compensation

The performances of the closed-loop controller were observed by adding small amplitudes of harmonics to the 0.2v 10hz sine signal whose anti-hysteresis coefficients were calculated above. The harmonic signal applied to the Y input is:

$$\begin{aligned} Y_{ref} = {} & 0.2 * \sin(2 * \mathrm{pi} * 10) \\ & + 0.05 * \sin(2 * \mathrm{pi} * 5)\ 0.05 * \sin(2 * \mathrm{pi} * 20) \\ & + 0.05 * \sin(2 * \mathrm{pi} * 30)\ + 0.02 * \sin(2 * \mathrm{pi} * 40) \\ & + 0.04 * \sin(2 * \mathrm{pi} * 10) \end{aligned} \tag{6.23}$$

And signal applied to the X input is:

$$X_{ref} = 0.2 * \sin(2 * \mathrm{pi} * 10) \tag{6.24}$$

Total harmonic distortion of the applied signal is calculated with formula

$$\mathrm{THD} = \frac{\sqrt{\mathrm{V}_2^2 + \mathrm{V}_3^2 + \mathrm{V}_4^2 + \cdots + \mathrm{V}_n^2}}{\mathrm{V}_S} \tag{6.25}$$

By using this formula, a comparison of how successful the signal is in compensation and closed-loop control can be given by using the anti-hysteresis curve of the dominant amplitude sine signal for anti-hysteresis compensation. It was seen that the anti-hysteresis compensator designed for the reference signal of signals with many harmonics did not work.

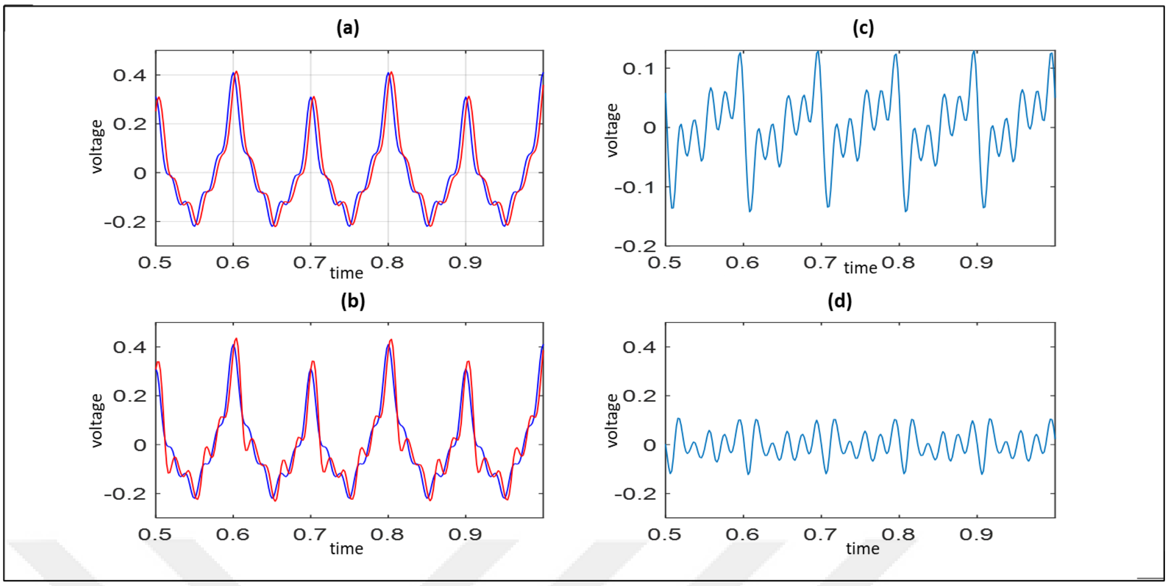

Figure 6.24. Mixed harmonic reference, y-axis closed loop results, (a) without hysteresis compensation(blue-refererence,red output), (b) with hysteresis compensation(blue-refererence,red output), (c) tracking error without hysteresis compensation, (d) tracking error with hysteresis compensation

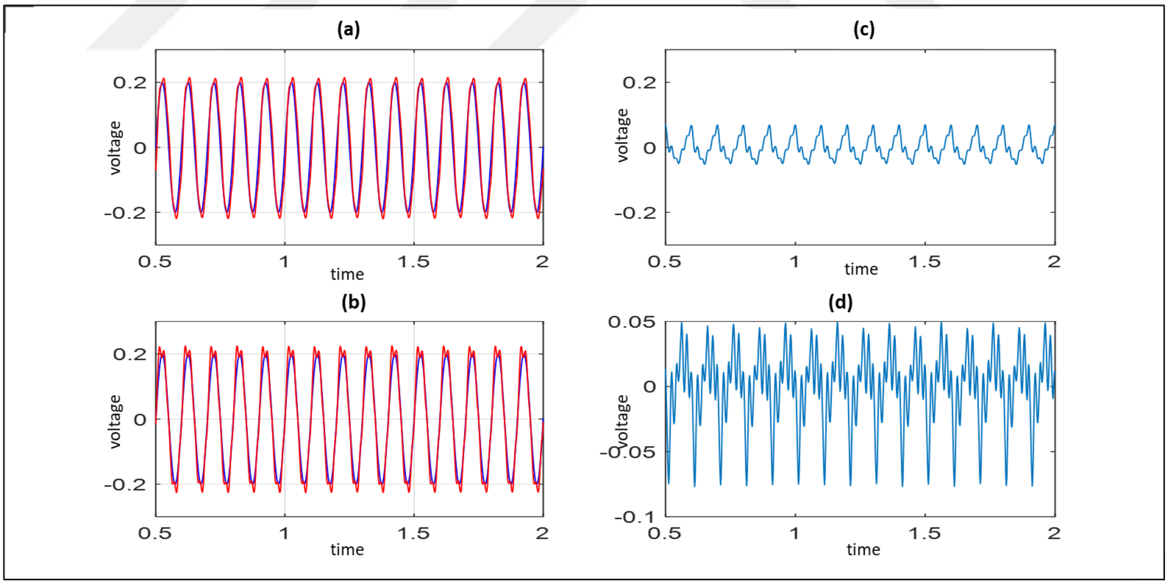

Figure 6.25. Mixed harmonic reference, x-axis closed loop results, (a) without hysteresis compensation(blue-refererence,red output), (b) with hysteresis compensation(blue-refererence,red output), (c) tracking error without hysteresis compensation, (d) tracking error with hysteresis compensation

$\| \quad \|_2$ norm comparison of the error signals in the closed loop control case when anti-hysteresis compensation on and off, is given in Table 6.4. It is shown that Feedforward Anti-hyteresis compensator radically reduces the tracking error.

Table 6.4. Closed Loop Controller Comparison Table with or Without Feedforward Controller

Reference Signal	**Feedforward AntiHysteresis Compensation On / Off**	$\|y_{ref} - y_{out}\|_2$	$\|x_{ref} - x_{out}\|_2$
Sine	On	0.3317	1.1996
	Off	4.31034	1.6182
Triangle	On	0.7901	0.8461
	Off	1.9183	1.6885
$W_{harmonic}$	On	2.8548	1.5021
	Off	3.1197	1.7651

In another experiment, a sweep sine signal with 0.2v amplitude between 1-21 hz was applied to the closed-loop controller as a reference input. In Figure 6.26. and Figure 6.27. x-axis and y-axis closed loop controller reference vs output signals also tracking errors is shown. . $\| \quad \|_2$ norm comparison of output errors is also given in Table 6.5.

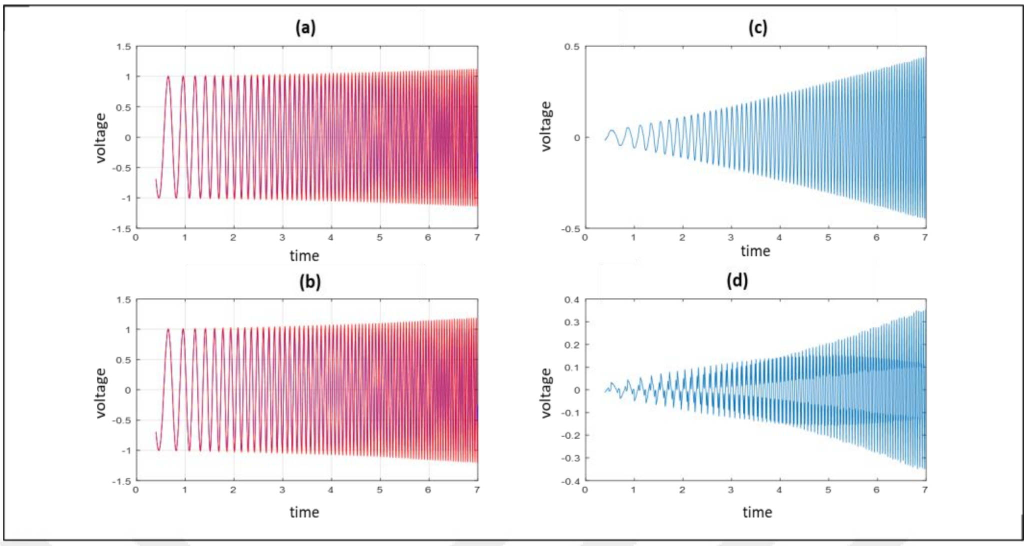

Figure 6.26. Sweep sine reference, x-axis closed loop results, (a) without hysteresis compensation(blue-refererence,red output), (b) with hysteresis compensation(blue-refererence,red output), (c) tracking error without hysteresis compensation, (d) tracking error with hysteresis compensation

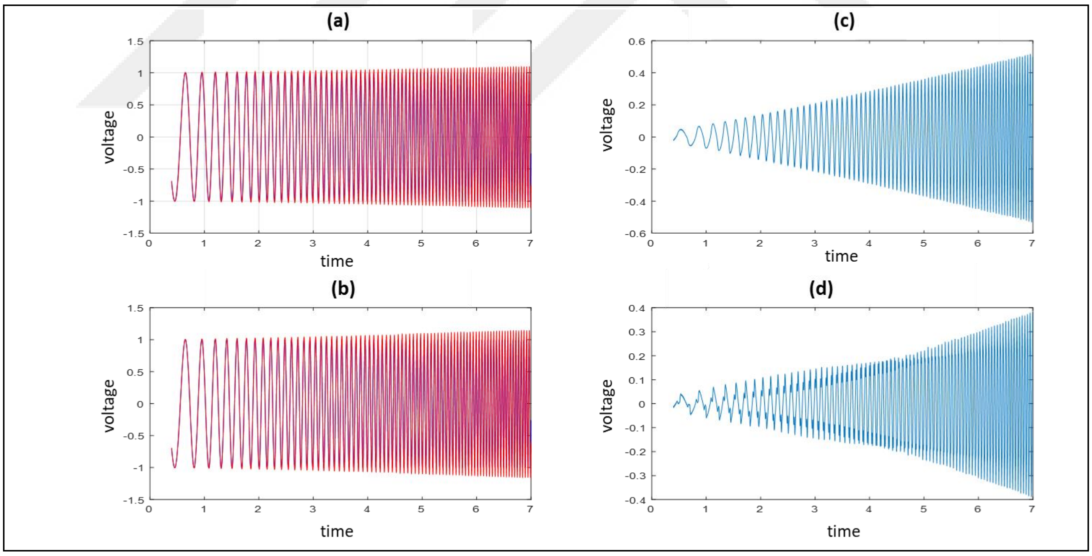

Figure 6.27. Sweep sine reference, y-axis closed loop results, (a) without hysteresis compensation(blue-refererence,red output), (b) with hysteresis compensation(blue-eferenence,red output), (c) tracking error without hysteresis compensation, (d) tracking error with hysteresis compensation

Table 6.5. Closed Loop Controller Results with or without Feedforward Controller

Reference Signal	**Feedforward AntiHysteresis Compensation On / Off**	$\left\Vert y_{ref} - y_{out} \right\Vert_2$	$\left\Vert x_{ref} - x_{out} \right\Vert_2$
Sine Sweep Signal (1-21Hz)	On	7.8919	6.3407
	Off	11.5556	9.5667

6.3. DISCUSSION OF THE RESULTS

By applying reference inputs at different waveforms and frequencies to the FSM, the performance of the system in combination with hysteresis compensation and closed or open loop controllers has been investigated.

The hysteresis parameters of the curve obtained for 0.2v-10Hz input were found by taking 6 sample. The inverse hysteresis model found using the inverse P-I model calculation method applied to the real system via Simulink and the data acquisition card.

In open loop hyteresis control experiments, it was seen that the relationship between input and output is linear in the absence of FSM axial coupling. It was seen that linearity decreases somewhat in the case of axial coupling but it is approximately one third compared to the case of no compensation. Also including similar harmonic component signals like triangle wave also compensated by the same anti-hysteresis compensator.

Closed loop experiments with hysteresis compensation has been also performed. Triangle wave, sweep signal and sine signals were applied to the system, and tracking errors were observed in cases with or without compensation, and in cases where compensation was present, it was seen that the 2-norm always decreased.

7. CONCLUSIONS AND FUTURE WORK

In this study, the control of FSM mirrors, which are frequently used in space technology and laser beam steering processes, has been examined. In addition, coarse tracking and pointing, fine tracking mechanisms used in space optical communication have been examined and it has been stated that the need for jitter rejection is necessary for maximum beam power transfer to the opposite terminal.

For this purpose, PID type controllers is proposed for the beam jitter problem. Since the model-based controller design is adopted, the system identification tools are used to obtain the mathematical model of the FSM using the atmospheric turbulence data, which is determined experimentally. Then, three types of low order controllers which are the MIMO loop shaping, $\mathcal{H}_\infty$ decentralized PID and $\mathcal{H}_\infty$ centralized PID, are designed. The simulation and the experimental results show that the low order PID controllers perform better than the fixed order MIMO loop shaping controller. However, it has been seen in the results that the MIMO loop shaping method has similar performance to the controller designed with the adaptive youla parametrization method, which has higher mathematical complexity. It was shown that low-complexity controllers can be used to solve the problem.

The hysteresis characteristic is a drawback for the use of piezo FSMs. The varying hysteresis characteristics for different frequency and amplitude inputs have been investigated. Hysteresis nonlinearity have been modelled and anti-hysteresis compensator have been applied to piezo FSM mirrors. Open loop anti-hysteresis compensator performances and MIMO closed loop controllers with feedforward hysteresis compensation have been compared in the tracking performance of FSM.

Because of the poor coupling between the actuators and the tip-tilt mirror, there is no remarkable performance difference between the decentralized and the centralized PID controllers. In order to see the difference, the same design procedure should be examined on the continous deformable mirrors with highly coupled actuator layout. This problem will be considered as the future work.

Meanwhile FSM’s are used to reject the disturbances in the laser beam, they are also used for beam tracking, especially in free space optical communication applications [80] . It is not desirable to reduce the performance of FSM’s used for reference tracking against external disturbance effects. As a future study, reference tracking controller design, robust to external disturbances can be studied, while it's hysteresis nonlinear characteristics had been reduced while tracking the laser beam.

REFERENCES

1. Free-space optical communication - Wikipedia [Internet]. [cited 2021 Nov 3]. Available from: https://en.wikipedia.org/wiki/Free-space_optical_communication

2. Steinvall O. Performance of laser tracking of small targets during turbulence and beam jitter. Optical Engineering. 2004 Jul 1;43(7):1609.

3. Toyoda M. Acquisition and tracking control of satellite-borne laser communication systems and simulation of downlink fluctuations. Optical Engineering. 2006 Mar 1;45(3):036001.

4. Jia P, Zhang S. Simulation and fabrication of the atmospheric turbulence phase screen based on a fractal model. Research in Astronomy and Astrophysics. 2012;12(5).

5. Dissipation of energy in the locally isotropic turbulence. Proceedings of the Royal Society of London Series A: Mathematical and Physical Sciences. 1991;434(1890).

6. Valerian Ilich Tatarski. Wave propagation in a turbulent medium. McGraw-Hill; 1961.

7. Fried DL. Optical Resolution Through a Randomly Inhomogeneous Medium for Very Long and Very Short Exposures. Journal of the Optical Society of America. 1966;56(10):1372–9.

8. John W. Hardy. Adaptive Optics for Astronomical Telescopes. 1998.

9. Abahamid A, Vernin J, Benkhaldoun Z, Jabiri A, Azouit M, Agabi A. Seeing, outer scale of optical turbulence, and coherence outer scale at different astronomical sites using instruments on meteorological balloons. Astronomy and Astrophysics. 2004;422(3):1123–7.

10. Fuchs A, Vernin J, Tallon M. Laboratory simulation of a turbulent layer: optical and in situ characterization. 1996.

11. Cardema JC, Tanzillo JN, Lee S, Dunbar CB. Performance and characterization results of a lasercom testbed for the pointing, acquisition, and tracking subsystem of a satellite-to-satellite laser communications link. In: Free-Space Laser Communications VIII. SPIE; 2008. p. 70910P.

12. Tolker-Nielsen T, Guillen J-C. SILEX: The First European Optical Communication Terminal in Orbit. 1998.

13. Anderson EH, Blankinship RL, Fowler LP, Glaese RM, Janzen PC. Adaptive filtering and feed-forward control for suppression of vibration and jitter. In: Acquisition, Tracking, Pointing, and Laser Systems Technologies XXI. SPIE; 2007. p. 65690Q.

14. Ding K, Huang Y, Ma J. Satellite APT system for Satellite-earth laser communication modeling, simulation and analysis. In: 5th International Symposium on Advanced Optical Manufacturing and Testing Technologies: Optical Test and Measurement Technology and Equipment. SPIE; 2010. p. 76566L.

15. Clements E, Aniceto R, Barnes D, Caplan D, Clark J, Portillo I del, et al. Nanosatellite optical downlink experiment: design, simulation, and prototyping. Optical Engineering. 2016 Sep 13;55(11):111610.

16. Shantha Lakshmi K, Senthil Kumar MP, Kavitha KVN. Inter-satellite laser communication system. Proceedings of the International Conference on Computer and Communication Engineering 2008, ICCCE08: Global Links for Human Development. 2008;978–83.

17. Wu R, Zhao X, Tian C. Improving line-of-sight pointing accuracy of laser communication system based on Kalman filter. Optical Engineering. 2019 Jan 23;58(01):1.

18. Perez E, Bailly M, Pairot JM. Pointing Acquisition And Tracking System For Silex Inter Satellite Optical Link. In: Acquisition, Tracking, and Pointing III. SPIE; 1989. p. 277.

19. Brändle M. Pointing/tracking control design for a high energy laser system. IEEE/ASME International Conference on Advanced Intelligent Mechatronics, AIM. 2014;676–82.

20. Borrello M. A multi stage Pointing Acquisition and Tracking (PAT) control system approach for air to air laser communications. In: Proceedings of the American Control Conference. 2005. p. 3975–80.

21. Soysal G, Efe M. Kalman Filter Aided Cooperative Optical Beam Tracking. 2010.

22. Li G, Xie C, Ou L, Zhou Z. Design of optical axis jitter control system for multi beam lasers based on FPGA. In SPIE-Intl Soc Optical Eng; 2018. p. 207.

23. Gu J, Ai Y. Design of active disturbance rejection controller for space optical communication coarse tracking system. In: AOPC 2015: Advances in Laser Technology and Applications. SPIE; 2015. p. 96711Y.

24. Xiao Y, Guo Z, Xuan W. Experiment study for simulation tracking of coarse pointing subsystem. 2012 2nd International Conference on Consumer Electronics, Communications and Networks, CECNet 2012 - Proceedings. 2012;1:3239–42.

25. Yamashita T, Morita M, Shimizu M, Eto D, Shiratama K, Murata S. The new tracking control system for Free-Space Optical Communications. 2011 International Conference on Space Optical Systems and Applications, ICSOS'11. 2011;(Mic):122–31.

26. Yamashita T, Ogura N, Kurii T, Hashimoto T. Improved satellite attitude control using a disturbance compensator. Acta Astronautica. 2004;55(1):15–25.

27. Orzechowski PK, Chen NY, Gibson JS, Tsao TC. Optimal suppression of laser beam jitter by high-order RLS adaptive control. IEEE Transactions on Control Systems Technology. 2008 Mar;16(2):255–67.

28. Yoon H, Bateman BE, Agrawal BN. Laser beam jitter control using recursive-least-squares adaptive filters. Journal of Dynamic Systems, Measurement and Control, Transactions of the ASME. 2011;133(4):1–8.

29. Watkins RJ, Agrawal BN. Use of least means squares filter in control of optical beam jitter. Journal of Guidance, Control, and Dynamics. 2007;30(4):1116–22.

30. McEver MA, Cole DG, Clark RL. Adaptive feedback control of optical jitter using Q-parameterization. Optical Engineering. 2004;43(4).

31. Orzechowski PK, Gibson S, Tsao TC, Herrick D, Beazel V, Mahajan M, et al. Nonlinear adaptive control of optical jitter with a new liquid crystal beam steering device. In: Proceedings of the American Control Conference. [American Automatic Control Council]; 2008. p. 4185–90.

32. Pérez Arancibia NO. Variable-order adaptive control of a microelectromechanical steering mirror for suppression of laser beam jitter. Optical Engineering. 2006 Oct 1;45(10):104206.

33. Tang T, Qi B, Yang T. Youla – Kucera Parameterization-Based Optimally. 2018;18(15):6154–60.

34. Skormin VA, Tascillo MA, Busch TE. Adaptive jitter rejection technique applicable to airborne laser communication systems [Internet]. Available from: http://spiedigitallibrary.org/ss/termsofuse.aspx

35. Xue Z, Qi B, Ren G. Vibration-induced jitter control in satellite optical communication. International Symposium on Photoelectronic Detection and Imaging 2013: Laser Communication Technologies and Systems. 2013;8906:89061X.

36. Huang Y. Acceleration feedback of a CCD-based tracking loop for fast steering mirror. Optical Engineering. 2009 Jan 1;48(1):013001.

37. Pérez Arancibia NO, Chen N, Gibson S, Tsao T-C. Adaptive Control of a MEMS Steering Mirror for Suppression of Laser Beam Jitter.

38. Orzechowski PK, Chen NY, Gibson JS, Tsao TC. Optimal suppression of laser beam jitter by high-order RLS adaptive control. IEEE Transactions on Control Systems Technology. 2008 Mar;16(2):255–67.

39. Orzechowski PK, Gibson S, Tsao TC, Herrick D, Beazel V, Mahajan M, et al. Nonlinear adaptive control of optical jitter with a new liquid crystal beam steering device. In: Proceedings of the American Control Conference. [American Automatic Control Council]; 2008. p. 4185–90.

40. Lin Y-H, Mahajan M, Taber D, Wen B, Winker B. Compact 4 cm aperture transmissive liquid crystal optical phased array for free-space optical communications. In: Free-Space Laser Communications V. SPIE; 2005. p. 58920C.

41. Pérez Arancibia NO. Variable-order adaptive control of a microelectromechanical steering mirror for suppression of laser beam jitter. Optical Engineering. 2006 Oct 1;45(10):104206.

42. Turan H, Engin SN. LQR Based Optimal PID Controller Design for Suppression of the Jitter in Laser Beam. In: 2020 28th Signal Processing and Communications Applications Conference, SIU 2020 - Proceedings. Institute of Electrical and Electronics Engineers Inc.; 2020.

43. Watkins RJ, Chen H-J, Agrawal BN, Shin YS. Optical beam jitter control. In: Free-Space Laser Communication Technologies XVI. SPIE; 2004. p. 204.

44. Dai C, Zhu M, Sun T, Dong H. Design and simulation of LQR controller based on fast steering mirror used in compound-axis system. In SPIE-Intl Soc Optical Eng; 2020. p. 222.

45. American Piezo Ceramics Products & Services [Internet]. 2021 [cited 2021 Oct 29]. Available from: https://www.americanpiezo.com/standard-products/stack-actuators.html

46. Song H, Zhang J heng, Yang P, Huang H cai, Zhan S yue, Liu T jun, et al. Modeling of a dynamic dual-input dual-output fast steering mirror system. Frontiers of Information Technology and Electronic Engineering. 2017 Oct 1;18(10):1488–98.

47. Wang G, Rao C. Adaptive control of piezoelectric fast steering mirror for high precision tracking application. Smart Materials and Structures. 2015;24(3).

48. Xu Q, Tan KK. Advances in Industrial Control Advanced Control of Piezoelectric Micro-/Nano-Positioning Systems [Internet]. Available from: http://www.springer.com/series/1412

49. John Doyle BFAT. Feedback Control Theory. Vol. 22, Automatica. 1986. 761–762 p.

50. Li CH, Park SC. Corrigendum “An efficient document classification model using an improved back propagation neural network and singular value decomposition” [Experts Systems with Applications 36 (2P2) (2009) 3208-3215]

(DOI:10.1016/j.eswa.2008.01.014). Expert Systems with Applications [Internet]. 2009;36(5):9603. Available from: http://dx.doi.org/10.1016/j.eswa.2008.12.060

51. Toscano R. Signal and system norms. Advances in Industrial Control. 2013;(9781447151876):25–44.

52. Dahleh M, Dahleh MA, Verghese G. Lectıres on Dynamic Systems and Control. 2011.

53. Herzog R, Jürg K. Advanced Control: An Overview on Robust Control. 2009;1–31.

54. Skogestad S, Postlethwaite I. Multivariable Feedback Control—Analysis and Design. IEEE Control Systems. 2007;27(1):80–1.

55. Kučera V. A method to teach the parameterization of all stabilizing controllers. In: IFAC Proceedings Volumes (IFAC-PapersOnline). 2011.

56. Doyle JC, Glover K, Khargonekar PP, Francis BA. State-Space Solutions to Standard H2and H∞, Control Problems. IEEE Transactions on Automatic Control. 1989;34(8).

57. Navarro-Tapia D, Marcos A, Bennani S, Roux C. Structured H-infinity control based on classical control parameters for the VEGA launch vehicle. In: 2016 IEEE Conference on Control Applications, CCA 2016. Institute of Electrical and Electronics Engineers Inc.; 2016. p. 33–8.

58. Apkarian P, Noll D, Pellanda PC. 6 th World Congress on Structural and Multidisciplinary Optimization [Internet]. Available from: http://www.cert.fr/dcsd/cdin/apkarian/

59. Chi Z, Xu Q. Recent advances in the control of piezoelectric actuators. International Journal of Advanced Robotic Systems. 2014;11.

60. Ye W. Inverse Compensation of Hysteresis using Modified Generalized Prandtl-Ishlinskii Hysteresis Model. 2016;(September).

61. Zhang Z, Du C, Gao T, Xie L. Hysteresis modeling and compensation of PZT milliactuator in hard disk drives. 2014 13th International Conference on Control Automation Robotics and Vision, ICARCV 2014. 2014;980–5.

62. Wang W, Wang J, Chen Z, Wang R, Lu K, Sang Z, et al. Research on asymmetric hysteresis modeling and compensation of piezoelectric actuators with PMPI model. Micromachines. 2020;11(4).

63. Gu GY, Yang MJ, Zhu LM. Real-time inverse hysteresis compensation of piezoelectric actuators with a modified Prandtl-Ishlinskii model. Review of Scientific Instruments. 2012;83(6).

64. Wang G, Chen G, Zhou H, Bai F. Modeling and tracking control for piezoelectric actuator based on a new asymmetric hysteresis model. IEEE/CAA Journal of Automatica Sinica. 2017;4(4):782–91.

65. Ang WT, Garmón FA, Khosla PK, Riviere CN. Modeling Rate-dependent Hysteresis in Piezoelectric Actuator.

66. Zhang G, Zhang C, Gu J. Modeling and control of rate-dependent hysteresis in piezoelectric actuators. Chinese Control Conference, CCC. 2013;1929–34.

67. Qin Y, Zhao X, Zhou L. Modeling and identification of the rate-dependent hysteresis of piezoelectric actuator using a modified Prandtl-Ishlinskii model. Micromachines. 2017;8(4).

68. Li Y, Liu Z, Liu Y. Hysteresis Modeling of Piezoelectric Actuators and Feed-Forward Compensation Algorithm Research. International Journal of Control and Automation [Internet]. 2015 Jul 31;8(7):405–16. Available from: http://article.nadiapub.com/IJCA/vol8_no7/39.pdf

69. Han W, Jia R, Qin Y, Sun N. Modeling and Compensation of the Hysteretic Nonlinearity of Piezoelectric Actuators.

70. Zhu W, Bian L, An Y, Chen G, Rui X. Modeling and control of a two-axis fast steering mirror with piezoelectric stack actuators for laser beam tracking. Smart Materials and Structures. 2015;24(7).

71. Shen JC, Jywe WY, Chiang HK, Shu YL. Precision tracking control of a piezoelectric-actuated system. 2007 Mediterranean Conference on Control and Automation, MED. 2007;

72. Wang D, Yu P, Wang F, Chan HY, Zhou L, Dong Z, et al. Improving atomic force microscopy imaging by a direct inverse asymmetric PI hysteresis model. Sensors (Switzerland). 2015;15(2):3409–25.

73. Wang D, Yu P, Wang F, Chan HY, Zhou L, Dong Z, et al. Improving atomic force microscopy imaging by a direct inverse asymmetric PI hysteresis model. Sensors (Switzerland). 2015;15(2):3409–25.

74. Rakotondrabe M. Multivariable classical Prandtl–Ishlinskii hysteresis modeling and compensation and sensorless control of a nonlinear 2-dof piezoactuator. Nonlinear Dynamics. 2017;89(1):481–99.

75. Habineza D, Zouari M, le Gorrec Y, Rakotondrabe M. Multivariable Compensation of Hysteresis, Creep, Badly Damped Vibration, and Cross Couplings in Multiaxes Piezoelectric Actuators. IEEE Transactions on Automation Science and Engineering. 2018;15(4).

76. Rakotondrabe M, Clévy C, Lutz P. Complete open loop control of hysteretic, creeped, and oscillating piezoelectric cantilevers. IEEE Transactions on Automation Science and Engineering. 2010;7(3):440–50.

77. Bertotti G, Mayergoyz ID. The Science of Hysteresis. Vols. 1–2, The Science of Hysteresis. 2006.

78. Gu GY, Yang MJ, Zhu LM. Real-time inverse hysteresis compensation of piezoelectric actuators with a modified Prandtl-Ishlinskii model. Review of Scientific Instruments. 2012;83(6).

79. Rakotondrabe M. Classical Prandtl-Ishlinskii modeling and inverse multiplicative structure to compensate hysteresis in piezoactuators. In: Proceedings of the American Control Conference. 2012.

80. Phong DX, Suzumoto R, Carrasco-Casado A, Moll F, Hosonuma T, Toyoshima M, et al. Modeling of piezoelectric actuator’s hysteresis and its effect on the control accuracy of a LEO-to-GEO laser-communication for a small satellite. In 2021.

APPENDIX A: SYSTEM IDENTIFICATION MATLAB CODE

```
Fs = 1000;
dt=1/Fs;
StartTime =0;
StopTime = 3.4;
t=(StartTime:dt:StopTime-dt);
diff=-pi/2;
% Generate x-axis outputs
x=0;
x_=0;
for m=1:50
    l=normrnd(0,2); % +5V  6
    w1=normrnd(50,10);
    x=l*cos(2*pi*w1*t+diff);
     x_=x_+x;
end
x_=x_/6;

% Generate y-axis outputs
,y=0;y_=0;
for m_1=1:50
    l1=normrnd(0,2); % +5V  6
    w1=normrnd(50,10);
    y=l1*cos(2*pi*w1*t+diff);
     y_=y_+y;
end

% Generate x-axis disturbance outputs
x=0;
xd_=0;
for m=1:50
    l=normrnd(0,2); % +5V  6
    w1=normrnd(250,25);
    x=l*cos(2*pi*w1*t+diff);
     xd_=xd_+x;
end
xd_=xd_/6;

% Generate y-axis disturbance outputs
y=0;
yd_=0;
for m_1=1:50
    l1=normrnd(0,2); % +5V  6
    w1=normrnd(50,10);
    y=l1*cos(2*pi*w1*t+diff);
     yd_=yd_+y;
end
Out_Data_T(:,1)= xd_';              % disturbance x axis
```

```
Out_Data_T(:,2)= yd_';              % disturbance y axis
Out_Data_T(:,3)= x_';
Out_Data_T(:,4)= y_';
```

% Adding Analog Input Channel toDAQ Card, Obtain I/O data

```
s.addAnalogInputChannel('Dev1',0,'Voltage')
s.addAnalogInputChannel('Dev1',1,'Voltage')
%% Adding Analog Output Chan nel
s.addAnalogOutputChannel('Dev1',0,'Voltage')
s.addAnalogOutputChannel('Dev1',1,'Voltage')
s.addAnalogOutputChannel('Dev1',2,'Voltage')
s.addAnalogOutputChannel('Dev1',3,'Voltage')
s.Rate = Fs;
 queueOutputData(s,Out_Data_T);
```

% Identificaton of models from the experimental data

```
close all
Fs=1000;
c=detrend(captured_data);
fsm_x = Out_Data(:,3);
fsm_y = Out_Data(:,4);
dist_x=Out_Data(:,1);
dist_y=Out_Data(:,2);
psd_x=c(:,1);
psd_y=c(:,2);

experiment_data = iddata([psd_x,psd_y],[fsm_x,fsm_y,dist_x,dist_y],1/Fs);
experiment_data.InputName =
{'FSM_X_input';'FSM_Y_input';'DIST_X_input';'DIST_Y_input'};
experiment_data.OutputName = {'X_PSD';'Y_PSD'};

mp3th_wdst = ssest(experiment_data(1:25000),3);
compare(experiment_data(1:25000),mp3th_wdst);
figure;
mp4th_wdst = ssest(experiment_data(1:25000),4);
compare(experiment_data(1:25000),mp4th_wdst);
figure;
mp5th_wdst = ssest(experiment_data(1:25000),5);
compare(experiment_data(1:25000),mp5th_wdst);
figure;
mp6th_wdst = ssest(experiment_data(1:25000),6);
compare(experiment_data(1:25000),mp6th_wdst);
figure;
```

% Compare identified models with real system outputs

```
 aa(1,:)= Out_Data_T(:,3)=; );          %input x
aa(2,:)= Out_Data_T(:,4)=; );           %input y
aa(3,:)=Out_Data_T(:,1);            %disturbance x
aa(4,:)=Out_Data_T(:,2); );             %disturbance y
```

```
c3=lsim(mp3th_wdst,aa',t);            %3.degree transfer func
c4=lsim(mp4th_wdst,aa',t);            %4. degree transfer func
c5=lsim(mp5th_wdst,aa',t);            %5. degree transfer func
c6=lsim(mp6th_wdst,aa',t);            %6. degree transfer func

difX=c3(:,1)-c(:,1);
nX = norm(difX);
nXYzd3th=100-nX/3;
GnXYzd3th=200*goodnessOfFit(c3(:,1),c(:,1),'MSE')

difY=c3(:,2)-c(:,2);
nY = norm(difY);
nYYzd3th=100-nY/3;
GnYYzd3th=200*goodnessOfFit(c3(:,2),c(:,2),'MSE')

difX=c4(:,1)-c(:,1);
nX = norm(difX)
nXYzd4th=100-nX/3;
GnXYzd4th=200*goodnessOfFit(c4(:,1),c(:,1),'MSE')

difY=c4(:,2)-c(:,2);
nY = norm(difY);
nYYzd4th=100-nY/3;
 GnYYzd4th=200*goodnessOfFit(c4(:,2),c(:,2),'MSE')

difX=c5(:,1)-c(:,1);
nX = norm(difX);
nXYzd5th=100-nX/3;
GnXYzd5th=200*goodnessOfFit(c5(:,1),c(:,1),'MSE')

difY=c5(:,2)-c(:,2);
nY = norm(difY);
nYYzd5th=100-nY/3;
GnYYzd5th=200*goodnessOfFit(c5(:,2),c(:,2),'MSE')

difX=c6(:,1)-c(:,1);
nX = norm(difX);
nXYzd6th=100-nX/3;
GnXYzd6th=200*goodnessOfFit(c6(:,1),c(:,1),'MSE')

difY=c6(:,2)-c(:,2);
nY = norm(difY);
nYYzd6th=100-nY/3;
GnYYzd6th=200*goodnessOfFit(c6(:,2),c(:,2),'MSE')
```

APPENDIX B: MIMO LOOP SHAPING AND $\mathcal{H}_\infty$ CONTROLLERS SYNTHESIS MATLAB CODE

% Smoothing the calculated atmospheric disturbance signal,

```
 Clear,close all;
load('29112019.mat');
Fs=100;
load('cn2-13L1500_2.txt');
cn2_x=cn2_13L1500_2(:,1)/40;
cn2_y=cn2_13L1500_2(:,2)/40;
% cn2_x(27192:27200)=0;
% cn2_y(27192:27200)=0;
cn2_x_smt(:,2)=smooth(cn2_x,0.002,'rloess');
cn2_y_smt(:,2)=smooth(cn2_y,0.002,'rloess');

tt=0.002:0.002:8;
ttt=0.002:0.002:40
cn2_x_smt(:,1)=tt';
cn2_y_smt(:,1)=tt';
 cn2_x_smt100=0;
cnt=1;

for c=1:length(cn2_x_smt);
   nb = 6;
    while nb > 1
        nb = nb-1;
        cn2_x_smt100(cnt,2)=cn2_x_smt(c,2);
        cnt=cnt+1;
    end
end
cn2_x_smt100(:,1)=ttt';

cn2_y_smt100=0;
cnt=1;
for c=1:length(cn2_y_smt);
   nb = 6;
    while nb > 1
        nb = nb-1;
        cn2_y_smt100(cnt,2)=cn2_y_smt(c,2);
        cnt=cnt+1;
    end
end
cn2_y_smt100(:,1)=ttt';
length(cn2_x)
L=length(tt')
figure
plot(tt,cn2_x_smt,tt,cn2_x);
```

```
figure
plot(tt,cn2_x);
a=length(cn2_x)

 % Power spectral density plots ,
figure;
[psd, f] = pspectrum(cn2_x_smt100(:,2), ttt');
subplot(2,1,1),loglog( f,psd, 'b')
grid on;
xlabel('f(Hz)')
ylabel('PSD((rad/s)^2/Hz)')
title('Power Spectral Density of X axis')

 [psd, f] = pspectrum(cn2_y_smt100(:,2), ttt');
subplot(2,1,2),loglog( f,psd, 'b')
grid on;
xlabel('f(Hz)')
ylabel('PSD((rad/s)^2/Hz)')
title('Power Spectral Density of Y axis')

% 4th order identified system
A4th=mp4th_wdst.A;
B4th=mp4th_wdst.B;
C4th=mp4th_wdst.C;
D4th=mp4th_wdst.D;

% 4th order system
A=A4th;
% Inputs
B1=B4th(:,3:4);  % Disturbance inputs
B2=B4th(:,1:2);  % Control inputs
Bs=[B2];
Bhinf=[B1 B2];

% Output and performance matrix
C1=C4th;  % performance matrix
C2=C4th;  % observed outputs
Cs=[C2];
Chinf=[C1;C2];
% D matrix
D12=D4th;
D22=D4th;
Dhinf=[D12;D22];
Ds=[0 0; 0 0];

% Loop shaping controller synthesis
G=ss(A,Bs,Cs,Ds);
Ghinf=ss(A,Bhinf,Chinf,Dhinf);
Eye=eye(2);
```

```
[b,a] = besself(2,3000,'low');
w = logspace(1,4);
f=tf(b,a)
f=f*3;
K=Eye*f
```

% Sensitivity, Cosensitivity plots

```
% form the compensated loop L
L = G*K;
T = feedback(L,eye(2));
T.InputName = {'alpha command','theta command'};
S1 = eye(2)-T;
S2 = feedback(eye(2),L); % S=inv(I+L);

figure
subplot(2,1,1),h=sigmaplot(G)
setoptions(h,'FreqUnits','Hz');
 title('System  G(s) ')

subplot(2,1,2),h=sigmaplot(L)
setoptions(h,'FreqUnits','Hz');
 title('Loop Gain G(s)*K(s) ')

figure
subplot(2,1,2),h=sigmaplot(T)
setoptions(h,'FreqUnits','Hz');
 title('CoSensitivity T(s)')

subplot(2,1,1),h=sigmaplot(S1)
setoptions(h,'FreqUnits','Hz');
 title('Sensitivity S(s) ')

figure,nyquist(L)
title('Nyquist of Loop Gain, L(s)=G(s)*K(s)')
```

% Decentralized h-infinity controller synthesis

```
G=sys_mimo;
 C1 = ltiblock.pid('C1','pid');
C2 = ltiblock.pid('C2','pid');
C = blkdiag(C1,C2);

lfG=1e3;           % desired low frequency gain
hfG=0.5;           % desired high frequency gain
w0= 2*pi*80 ;        % desired crossover  frequency
wS=(hfG*s+w0)/(s+w0/lfG);
 lfG=0.001;          % desired low frequency gain
hfG= 40;           % desired high frequency gain
w0= 2*pi*400;        % desired crossover
wT=(s+w0*lfG)/(s/hfG+w0);
```

```
figure;
bodemag(wS,'b-',wT,'r--'); grid;

P = augw(G,wS*eye(2) ,[] , wT*eye(2) ); % Derive augmented plant
CL0 = lft(P,C);                    % calculate LFT
op = hinfstructOptions('RandomStart',5);
[CL, gam] = hinfstruct(CL0,op);
gam
 C1 = getBlockValue(CL,'C1')
C2 = getBlockValue(CL,'C2')
C_final=[C1 0 ;
        0    C2];
C_ss=ss(C_final);
 Tsim = feedback(G*C_ss,eye(2)) ;
```

% Centralized h-infinity controller synthesis

```
Kp = realp('Kp',zeros(2));
Ki = realp('Ki',zeros(2));
Kd = realp('Kd',zeros(2));
tau = realp('tau', 1);
Kpid = Kp + Ki*tf(1,[1 0]) + Kd*tf([1 0],[tau 1]) ;
 % Sensitivity weight
lfG=1e3; % desired low frequency gain
hfG=0.5; % desired high frequency gain  % 0.5
w0= 2*pi*80 ; % desired crossover
wS=(hfG*s+w0)/(s+w0/lfG);
% Coensitivity weight
 lfG=0.001; % desired low frequency gain
hfG= 40; % desired high frequency gain
w0= 2*pi*400; % desired crossover  400
wT=(s+w0*lfG)/(s/hfG+w0);
figure;
bodemag(wS,'b-',wT,'r--'); grid;
legend('Sensitivity weight','Complementary sensitivity weight')
P = augw(G,wS*eye(2) ,[] , wT*eye(2) );   % Derive augmented plant
CL0 = lft(P,Kpid);
op = hinfstructOptions('RandomStart',5);
[CL, gam] = hinfstruct(CL0,op);
gam
 Kp=CL.Blocks.Kp.Value
Ki=CL.Blocks.Ki.Value
Kd=CL.Blocks.Kd.Value
tau=CL.Blocks.tau.Value
Kpid = Kp + Ki*tf(1,[1 0]) + Kd*tf([1 0],[tau 1]) ;
C_final=ss(Kpid);
figure;
Tsim = feedback(G*C_final,eye(2)) ;
```

APPENDIX C: HYSTERESIS CURVE IDENTIFICATION AND INVERSE HYSTERESIS CALCULATION CODE

```
clear
close ALL
t=0:0.0025:12.5;
Wh_fw=[0.232,0.093,0.05,0.1,0.136111111,2.088888889];
Wh_inv=[4.31034,-1.23342,-0.410256,-0.561404,-0.4689,-1.26599];
r_fw=[0.025,0.15,0.25,0.35,0.45,0.495]
r_inv=[0 ,0.029,  0.0615  ,0.099  ,0.1465 ,0.174];

%  Applying Sine input to inverse hysteresis model
c=[1:6], nc=length(c);
Upsd = (0.2*sin(2*pi*10*t - pi/2));        %input signal
Gtt=myfun2__v0(Wh_inv(c),Upsd,r_inv(c),nc)
a=length(Gtt)
figure
subplot(3,1,2),plot(Upsd(1:a-1),Gtt(1:a-1),'Color','blue','LineWidth',1);
title('Inverse Prandtl Ishlinsky Hysterezis Curve')
xlabel('input Displacement');
ylabel('Output Voltage' )
xlim([-0.5 0.5])
ylim([-0.5 0.5])

%  Applying Inverse hysteresis output to identified system  hysteresis model
Gtt2=myfun2__v0(Wh_fw(c),Gtt,r_fw(c),nc);
subplot(3,1,3),plot(Upsd(1:a-1),Gtt2(1:a-1),'Color','blue','LineWidth',1);
title('Compensated Input Output Curve')
xlabel('input Voltage');
ylabel('Output Beam Displacement' )
xlim([-0.5 0.5])
ylim([-0.5 0.5])
Ut =  (0.5*sin(2*pi*10*t - pi/2));         % input signal
Gtt3=myfun2__v0(Wh_fw(c),Ut,r_fw(c),nc);
a=length(Gtt3);

subplot(3,1,1),plot(Ut(1:a-1),Gtt3(1:a-1),'Color','blue','LineWidth',1);
title('Forward Prandtl Ishlinsky Hysterezis Curve')
xlabel('input Voltage');
ylabel('Output Beam Displacement' )
xlim([-0.5 0.5])
ylim([-0.5 0.5])
figure;
subplot(2,1,1),plot(t,Upsd)
subplot(2,1,2),plot(t,Gtt2)
```

% Piecewise linear approximation to measured FSM % hysteresis curve, bw and dy parameters calculation used % for identification hysteresis curve

```
load("matlab.mat")
f1=figure
plot(detrend(x_cmd_hystresis10hz_0_5v),detrend(x_psd_hystresis_8),'Color','black','Line
Width',0.4,'LineStyle','--')

hold on
x = [-0.5 -0.45]; y = [-0.188 -0.188];
x1 = [-0.45 -0.2]; y1= [-0.188 -0.130];
x2 = [-0.2 0]; y2 = [-0.130 -0.065];
x3 = [0 0.5]; y3 = [-0.065   0.1870];
x3 = [0 0.2]; y3 = [-0.065 0.01];
x4 = [0.2 0.4]; y4= [0.01  0.105];
x5 = [0.4 0.49]; y5 = [0.105   0.16];
x6 = [0.49 0.5]; y6 = [0.16   0.1870];
x7 = [0.5  0.45]; y7 = [0.1870 0.1870];

bw1=abs(x(1)-x(2)),bw2=bw1+abs(x1(1)-x1(2)),bw3=bw2+abs(x2(1)-
x2(2)),bw4=bw3+abs(x3(1)-x3(2)),bw5=bw4+abs(x4(1)-x4(2))
bw6=bw5+abs(x5(1)-x5(2)),bw7=bw6+abs(x6(1)-x6(2)),bw8=bw7+abs(x7(1)-x7(2));
dy1=abs(y(1)-y(2)),dy2=dy1+abs(y1(1)-y1(2)),dy3=dy2+abs(y2(1)-
y2(2)),dy4=dy3+abs(y3(1)-y3(2)),dy5=dy4+abs(y4(1)-y4(2))
dy6=dy5+abs(y5(1)-y5(2)),dy7=dy6+abs(y6(1)-y6(2)),dy8=dy7+abs(y7(1)-y7(2));
 line(x,y,'Color','mag','LineStyle','-.','LineWidth',2)
 line(x1,y1,'Color','green','LineStyle','-.','LineWidth',2)
 line(x2,y2,'Color','mag','LineStyle','-.','LineWidth',2)
 line(x3,y3,'Color','green','LineStyle','-.','LineWidth',2)
 line(x4,y4,'Color','mag','LineStyle','-.','LineWidth',2)
 line(x5,y5,'Color','green','LineStyle','-.','LineWidth',2)
 line(x6,y6,'Color','mag','LineStyle','-.','LineWidth',2)
 line(x7,y7,'Color','green','LineStyle','-.','LineWidth',2)
```

% Plotting of measured hysteresis curve

```
X = transpose(detrend(x_cmd_hystresis1hz0_5v));
Y = transpose(detrend(x_psd_hystresis_8));
grid on
grid minor
title('Forward Prandtl Ishlinsky Hysterezis Curve')
xlabel('Input Voltage');
ylabel('Laser Beam Replacement on PSD' )
ylim([-0.27 0.21])
annotation(f1,'textbox',...
    [0.2490625 0.114714285714286 0.160714285714286 0.0714285714285714],...
    'LineStyle','none');
figure
```

% Calculation of identified hysteresis curve outputs

```
Ut = (0.5*sin(2*pi*10*t - pi/2));   % input signal
```

```
Gtt=myfun2__v0(Wh_fw,Ut,r_fw,6);
a=length(Gtt);
hold on

title('Prandtl Ishlinsky Hysterezis Curve')
plot(detrend(x_cmd_hystresis10hz_0_5v),detrend(x_psd_hystresis_8),'Color','black','Line
Width',0.4,'LineStyle','--')
plot(Ut(1:a-1),Gtt(1:a-1),'Color','cyan','LineStyle','--','LineWidth',2);
xlabel('input Voltage');
ylabel('Output Beam Displacement')

%  Prandtl Ishlinsky hysteresis calculation function play operator
function  Gt = myfun2__tek(Whi, u,ri,n)
   Yeit(1:n)=0;                % yeit initial = [0]
   Yeit=Yeit';
   ri=ri.';
 for i=1:5001
   Ut_=0;
   Ut_(1:n)=u(i);
   Ut_=Ut_.';
   transpose(Yeit);
           Whi';
  transpose(Yeit);
   Yeit=(max(Ut_-ri, min(Ut_+ri, Yeit)));  % refresh yeit
   Gt(i)=transpose(Yeit)*Whi';
 end
```

APPENDIX D: SIMULINK MODELS

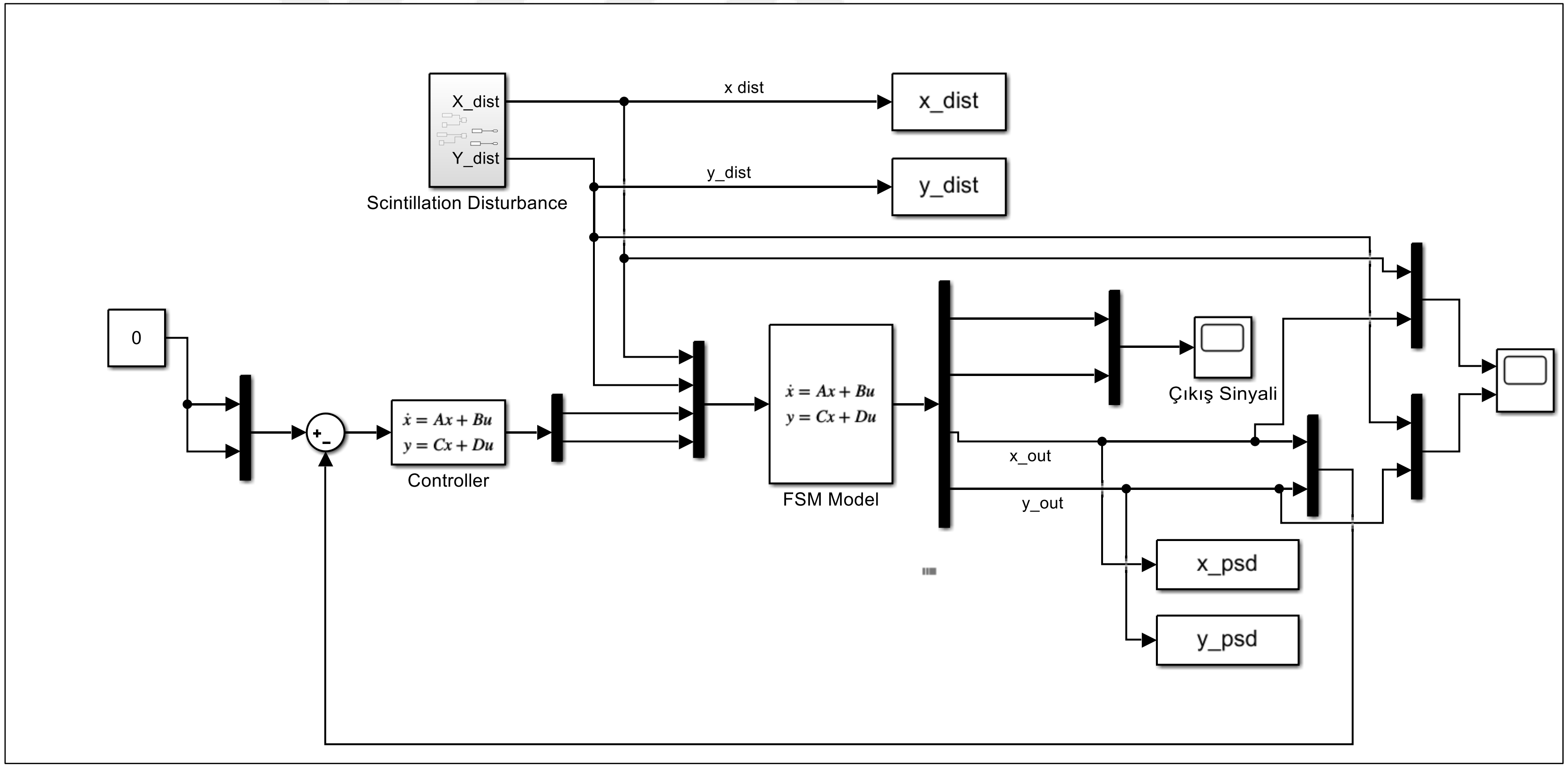

Figure D.1. Simulation phase, MIMO loop shaping and $\mathcal{H}_\infty$ centralized and decentralized controller

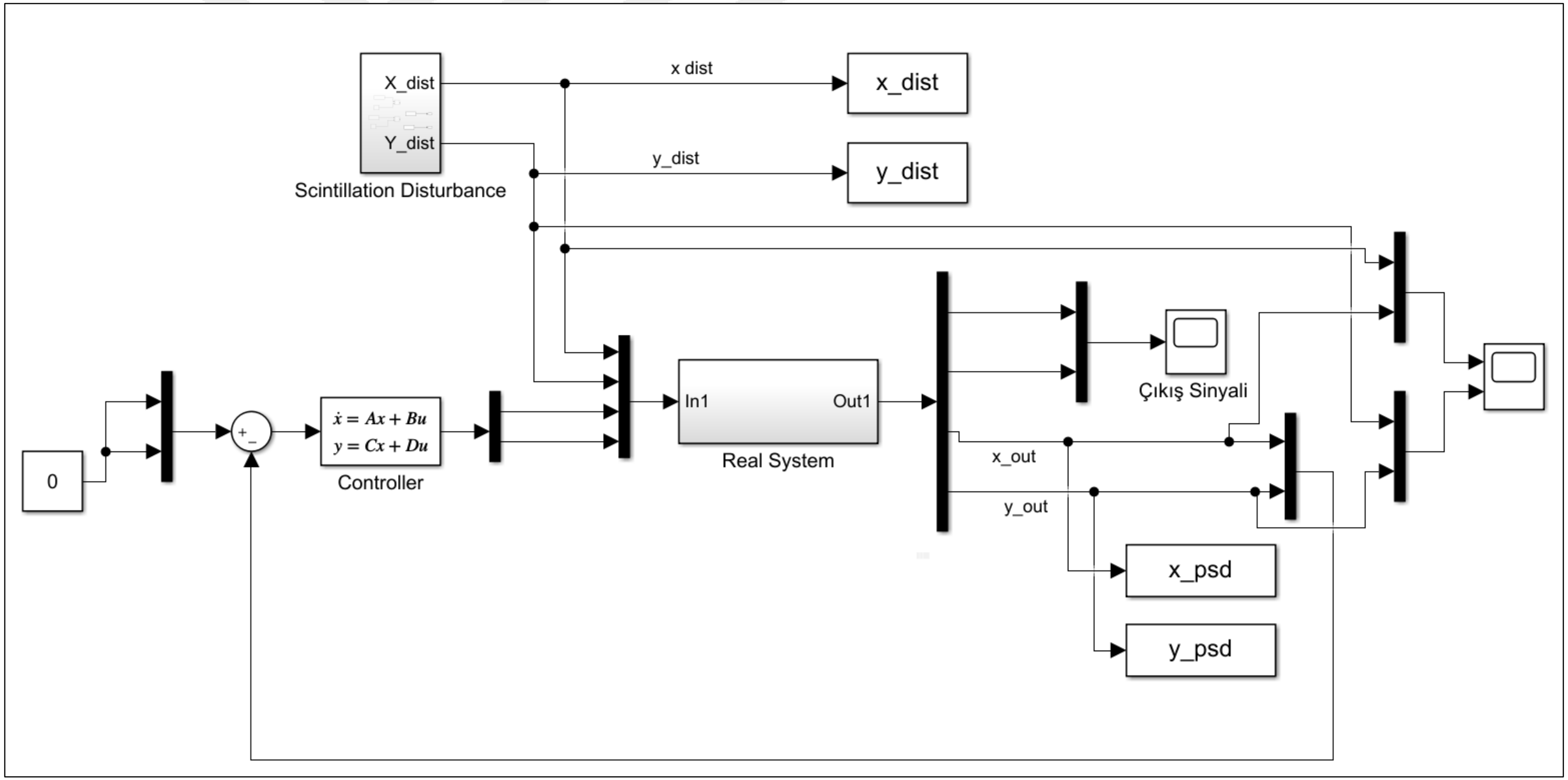

Figure D.2. Experimental phase, MIMO loop shaping and $\mathcal{H}_\infty$ centralized and decentralized controller

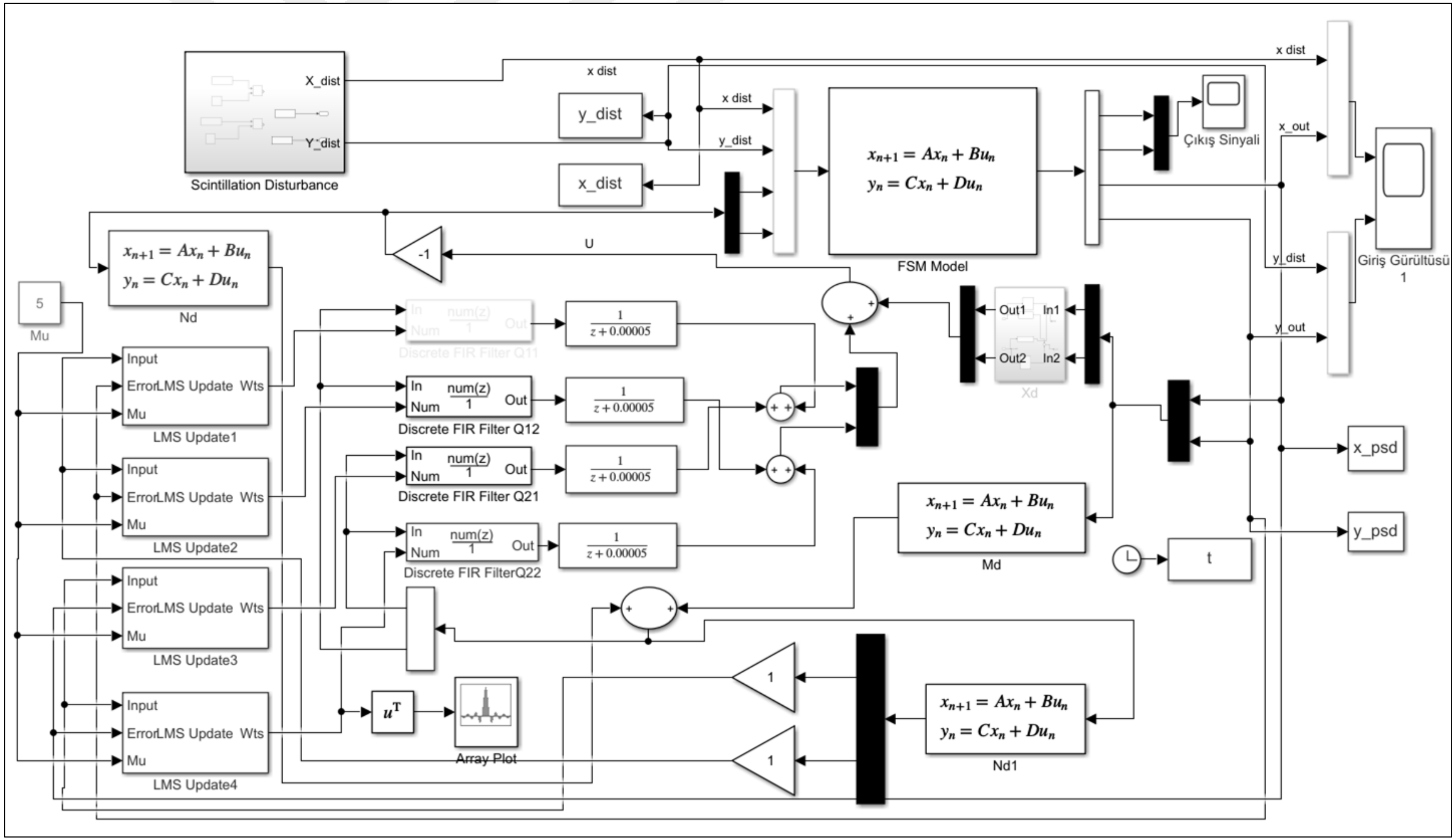

Figure D.3. Simulation phase, MIMO youla adaptive feedback controller

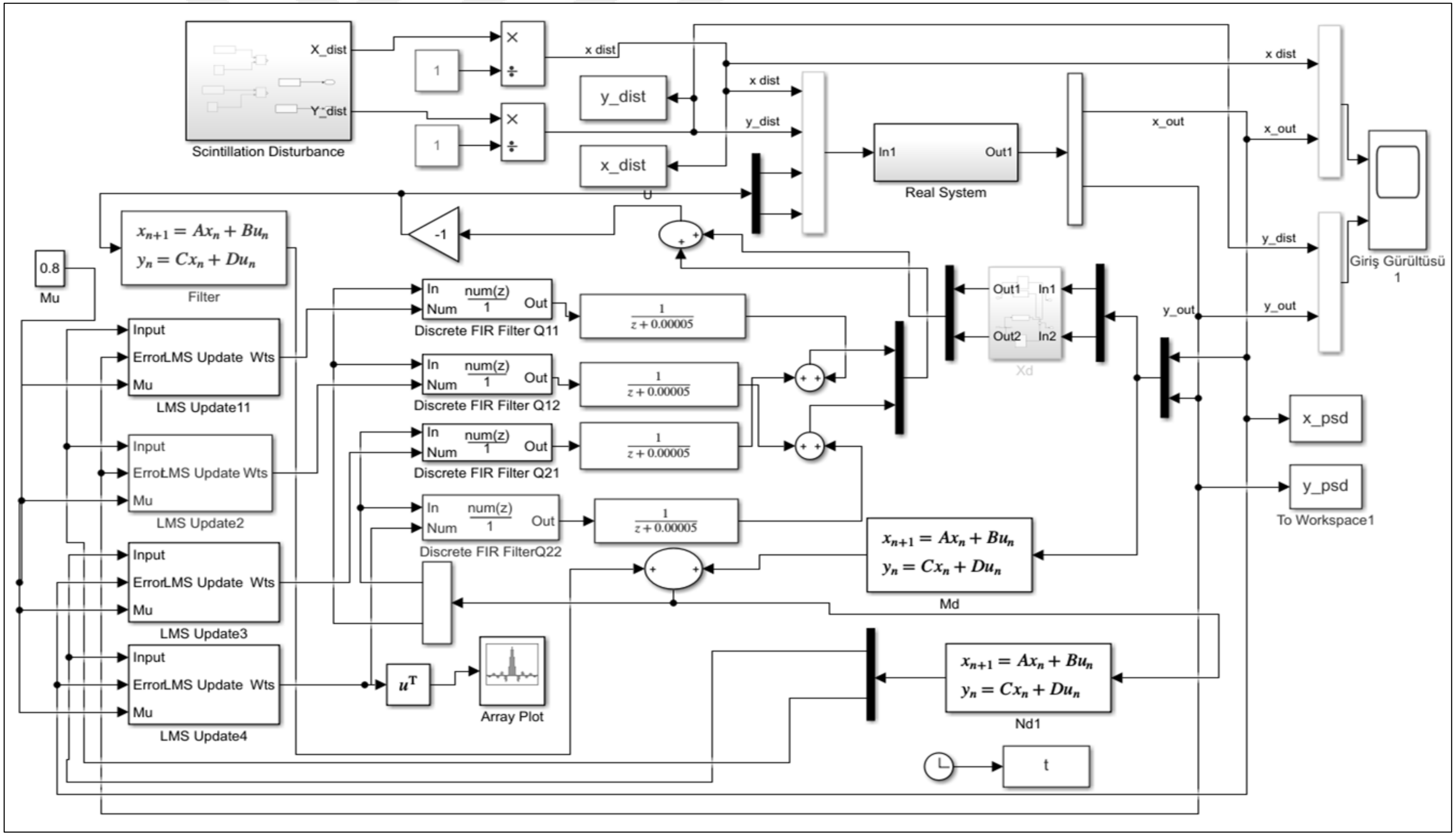

Figure D.4. Experimental phase, MIMO youla adaptive feedback controller

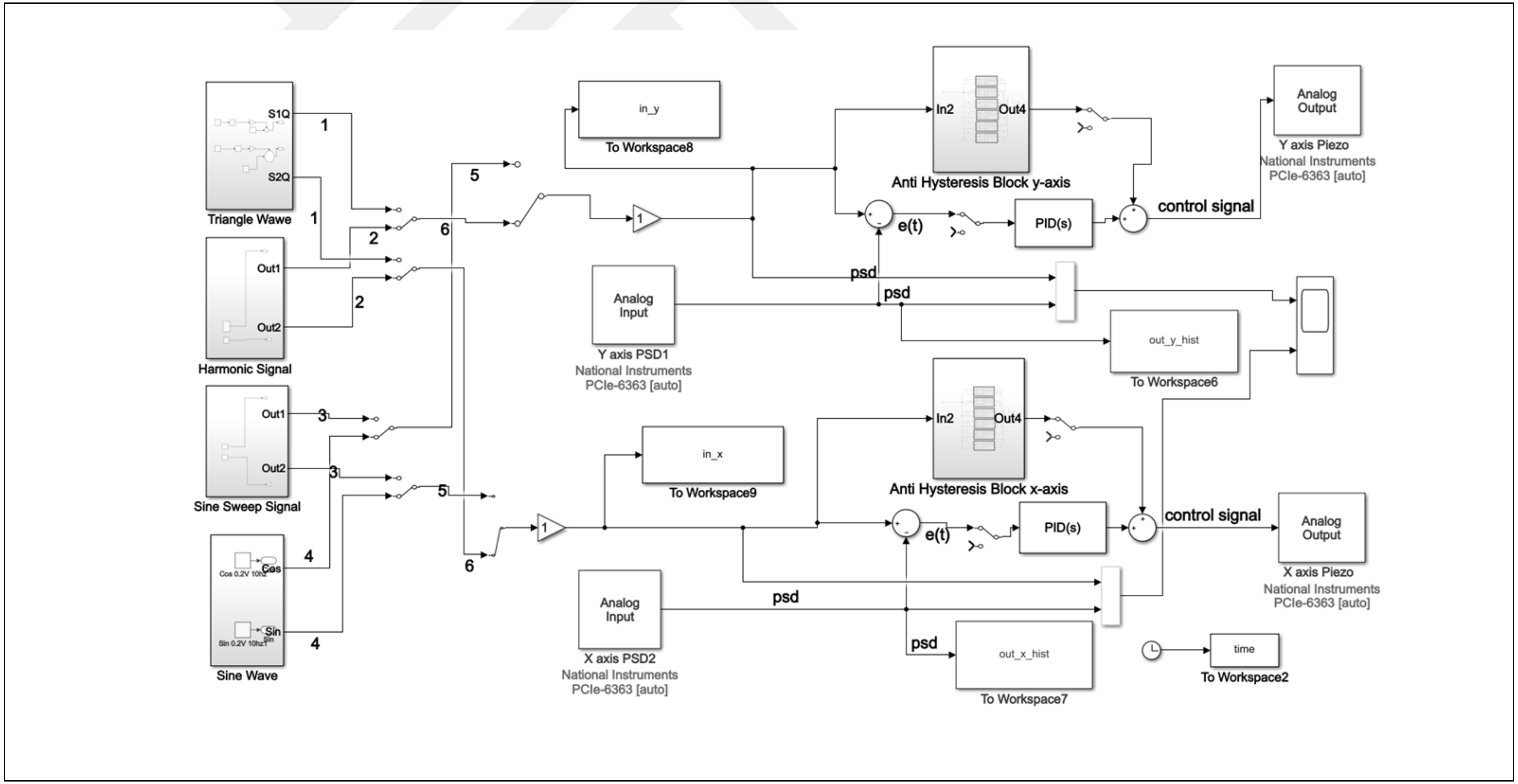

Figure D.5. Combination of feedback(PID) and feedforward(Inverse Hysteresis) control of two axis FSM